THE UNIVERSITY *of* EDINBURGH

SCHOOL OF CHEMISTRY

THE UNIVERSITY OF EDINBURGH

Design and synthesis of novel Polymers of Intrinsic Microporosity for gas separations

Thesis submitted for the degree of Doctor of Philosophy by:

Jie Chen

Supervisor: Neil B. McKeown **2020**

Declaration

Statement 1

This work has not been submitted in substance for any other degree or award at this or any other university or place of learning, nor is it being submitted concurrently in candidature for any degree or other award.

Signed …… (candidate)

Date ……

Statement 2

This thesis is being submitted in partial fulfilment of the requirements for the degree of Doctor of Philosophy.

Signed …… (candidate)

Date ……

Statement 3

This thesis is the result of my own independent work/investigation, except where otherwise stated. Other sources are acknowledged by explicit references. Any views expressed are my own.

Signed …… (candidate)

Date ……

Statement 4

I hereby give consent for my thesis, if accepted, to be available for photocopying and for inter-library loan, and for the title and summary to be made available to outside organisations.

Signed …… (candidate)

Date ……

Acknowledgements

First and foremost, I would like to thank my supervisor, Professor Neil B. McKeown, for giving me the opportunity to carry out my PhD within his research group. I really appreciate for all your support and guidance over the last four years.

I would like to thank all of the post-docs: Bibi, Rich, Grazia, Lino, Angelos and John for their help and support during my PhD period. It is really nice to working with all the group members, past and present, as my friends: Sarah, Hannah, ChunChun, Sandy, Panos, Emily, Hongchun, Travis, Khairul and Kimia. As a foreigner, the language was a big barrier when I was first here. A big thank to my group members for trying a lot to talk to me and encourage me. Thank you for supporting me all the time.

I would like to thank my family, especially my husband Yichuan for always being on my side. I am thankful for my Chinese friends, especially Chunchun, Cuicui and Pengyuan. Thank you for sharing the happiness with me and being patient with me when I was sad.

Four years' time in Edinburgh has passed fast. I believe it was the best choice I have ever made to come to Edinburgh. I enjoyed a lot, learnt a lot and gained a lot. Thank you!

Lay abstract

Membranes are used for gas separations such as O_2/N_2 separation for nitrogen enrichment and oxygen enrichment or natural gas upgrading (i.e. removal of CO_2 from CH_4). Membranes allow one gas to pass through but block other gases and are typically made of polymers. Polymers such as polymers of intrinsic microporosity (PIMs) containing pores that are in the size of gas molecules are useful materials for separation membranes.

Fluorine-containing polymers were reported to be repellent to CH_4, so that lower amounts of CH_4 would be expected to be adsorbed in the membrane than CO_2 or He, providing membranes with higher selectivities for CO_2/CH_4 and He/CH_4. In the first two parts of my work, four fluorinated PIMs were synthesised and investigated. In comparison with PIMs without fluorine-containing substituents, fluorinated PIMs displayed a better selectivity for CO_2/CH_4 and He/CH_4 due to the low CH_4 adsorption, suggesting products with high purities can be achieved.

The flux of membranes (i.e., membrane productivity) made by PIMs can be improved by increasing the pore densities. Pores in PIMs are formed by inefficient packing of polymer chains. The polymer chains of PIMs can be imagined as rigid sticks with contorted structure. When many contorted sticks are placed together in a disordered way, voids are generated between the sticks, and the amount of voids can be increased by increasing the distance between sticks. Therefore, in the last part of my work, a new building block was applied to construct polymer chains with higher interchain distance. The improved pore density provides new PIMs with high gas flux and good selectivity for CO_2/CH_4 and O_2/N_2, so the required membrane areas for separation of an amount of gas mixtures and associated costs can be reduced.

Abstract

Polymers of Intrinsic Microporosity (PIMs) are a new class of microporous material combining excellent solution processability with great structural diversity. The microporosity of PIMs derives from the inefficient packing of rigid and contorted polymeric chains. PIM membranes show great potential in gas separations (e.g., CO_2/CH_4, CO_2/N_2, O_2/N_2, H_2/N_2). However, they suffer from a well-defined tradeoff relationship between gas permeability and selectivity. Novel PIMs were designed and synthesised to investigate structure-property relationships and to provide a guideline for designing a new membrane material, which can provide a good balance of gas permeability and selectivity.

In the first part of this thesis, two fluorinated benzotriptycene polybenzodioxin polymers were prepared. These benzotriptycene-based PIMs exhibit ultra-high permeability with remarkable selectivity for carbon capture (CO_2/N_2) and natural gas purification (CO_2/CH_4), and defined the new upper bounds for these gas pairs together with four other benzotriptycene PIMs. In particular, the fluorinated polymers showed a better performance for CO_2/CH_4 and He/CH_4 than alkyl substituted benzotriptycene based PIMs due to their higher solubility selectivity resulting from the low CH_4 sorption in the fluorinated polymers.

In the second part, a fluorinated and non-fluorinated benzomethanoanthracene PIMs (PIM-OCF and PIM-OCP) were designed and synthesized in which fluorine atoms illustrated a minor effect on polymer microstructure confirmed by molecular simulation. The improved CO_2/CH_4 solubility selectivity exclusively derives from the inclusion of the fluorocarbon unit. The perfluoroalkyl chain substituent was also observed to reduce the CH_4 sorption and improve the solubility selectivities of CO_2/CH_4, He/CH_4 and H_2/CH_4, although the reduced size selectivity of perfluoroalkyl chain substituted polybenzodioxin polymer and low surface area of the perfluoroalkyl chain substituted Tröger's base polymer limit their potential applications.

In the last chapter, dibenzeno-6,13-methanopentacene (DBMP), a bridged bicyclic structure with a bulkier structure than that of triptycene, was utilized for PIM synthesis. The membrane of the homopolymer (PIM-DBMP) proved too fragile for membrane fabrication. Therefore,

the potential of DBMP for gas separations was investigated using a series of copolymers composed of DBMP and 5,5',6,6'-tetrahydroxy-3,3,3',3'-tetramethyl-1,1'-spirobisindane (TTSBI). The gas permeability of the copolymers demonstrated that the introduction of DBMP improves the gas permeability and selectivity simultaneously, overcoming the challenging tradeoff relationship. PIM-DBMP was further modified via amidoxime functionalisation, which was anticipated to improve the membrane's mechanical properties. As expected, a robust membrane of amidoxime-PIM-DBMP was achieved which showed promising gas separation performance.

Abbreviations

PIMs	Polymers of intrinsic microporosity
DBMP	Dibenzeno-6,13-methanopentacene
IUPAC	International Union of Pure and Applied Chemistry
BET	Brunauer-Emmett-Teller
CA	Cellulose acetate
PPO	Poly(phenylene oxide)
PI	Polyimide
NMP	N-methyl-pyrrolidone
THF	Tetrahydrofuran
DMAC	Dimethylacetamide
PSF	Bisphenol A polysulfone
CTA	Cellulose triacetate
MOFs	Metal Organic Frameworks
DAPI	Diaminophenylindane
BTDA	3,3'-4,4'-Benzophenone tetracarboxylic dianhydride
PTFE	Polytetrafluoroethylene
PALS	Positron annihilation lifetime spectroscopy
PTMSP	Poly(1-trimethylsilyl-1-propyne)
TR	Thermal rearrangement
PBO	Polybenzoxazole
3D	Three dimensional
2D	Two dimensional
S_NAr	Nucleophilic aromatic substitution
TFTPN	2,4,5,6-Tetrafluoroterephthalonitrile
TTSBI	5,5',6,6'-Tetrahydroxy-3,3,3',3'-tetramethyl-1,1'spirobisindane
DMF	Dimethylformamide
BTrip	Benzotriptycene
TMN	Tetramethyltetrahydronaphthalene
DA	Diels-Alder
TGA	Thermal gravimetric analysis

SA_{BET}	Brunauer-Emmett-Teller surface area
PSDs	Pore-size distributions
NLDFT	Non-local density functional theory
GPC	Gel Permeation Chormatography
AFM	Atomic force microscopy
OCF	Octafluoropentene
CPD	Cyclopentadiene
DCPC	Dicyclopentadiene
CPE	Cyclopentene
HDFE	1H, 1H, 2H-heptadecafluorodec-1-ene
OPA	*o*-Phthalaldehyde
PA	Phthalic anhydride
M_W	Weight average molecular weight
Mn	Number average molecular weight
V_{total}	Total free volume per gram
NMR	Nuclear magnetic resonance
h	Hours
d_{eff}	Effective gas diameter
CTCs	Charge-transfer complexes
AO	Amidoxime
FTIR	Fourier Transform Infrared Spectroscopy
P_X	Permeability
D_X	Diffusivity coefficient
S_X	Solubility coefficient
$\alpha_{X/Y}$	Ideal gas selectivity
D_X/D_Y	Diffusivity selectivity
S_X/S_Y	Solubility selectivity
DCM	Dichloromethane
SPS	Solvent Purification System
TLC	Analytical thin layer chromatography
Mp	Melting Point
MS	Mass Spectrometry
LRMS	Low-resolution mass spectrometr

EI	Electron impact ionization
HRMS	High-resolution mass spectrometry

Content

Chapter 1 Introduction

1.1 Porous materials

In recent years, porous materials are used in a wide-range of areas such as gas separation,[1-6] heterogeneous catalysis,[7, 8] hydrogen storage[9-11], to name but a few. Any material containing cavities, channels or interstices are described as porous materials.[12] When the depth of these free spaces is larger than their width, they will be defined as pores. The pores in a solid can be subdivided into several groups according to their shapes and the accessibility to an external fluid (**Figure 1.1**)[13]:

(a) Closed pores, which is totally isolated from neighbours
(b) Open, dead end, ink-bottle shape
(c) Open, through pores (c-e-c'), cylindrical shape
(d) Open, through pores (c-e-d), funnel shape
(e) Open, multiple-entry pores, cylindrical shape
(f) Open, blind end, cylindrical shape.
(g) Surface roughness (wider than they are deep)

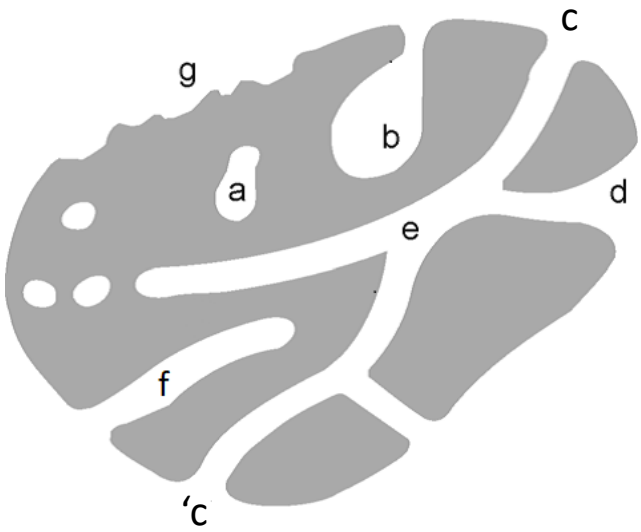

Figure 1.1 Schematic cross section of a porous solid.[13]

On the other hand, porous materials can be classified into three types with regard to their predominant pore sizes as identified by the International Union of Pure and Applied Chemistry (IUPAC)[12]: (i) macroporous - pores of diameter larger than 50nm; (ii) mesoporous - pores of diameter between 2 and 50 nm; (iii) microporous – pores of diameter less than 2 nm.

1.2 Surface area

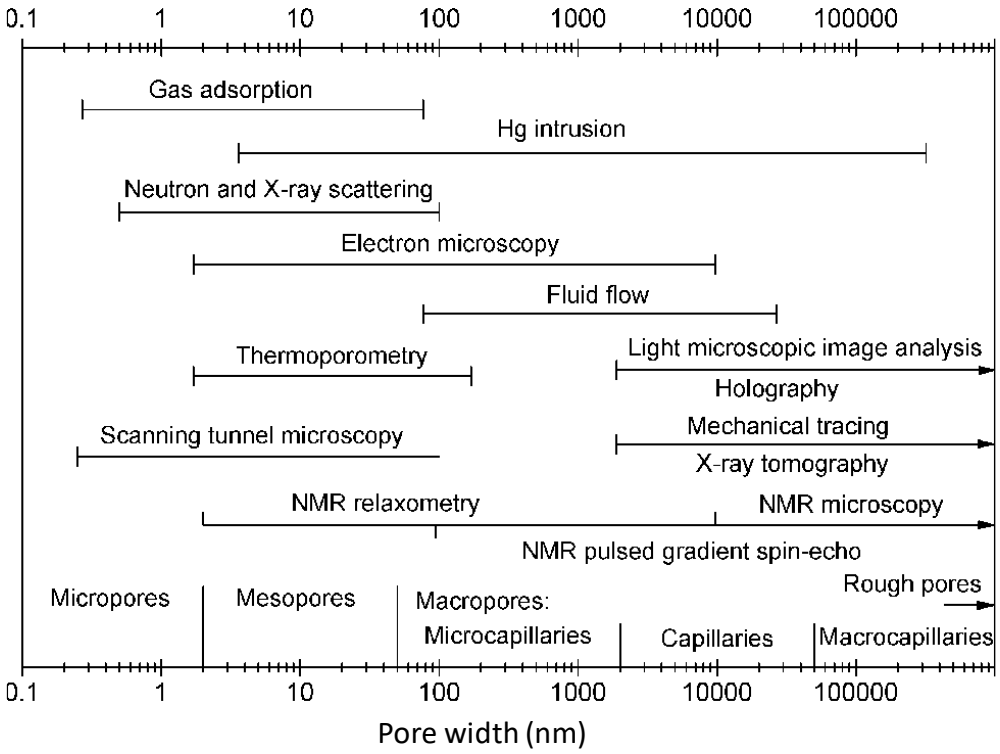

Figure 1.2 Measuring pore-size ranges using different characterization techniques.[14]

Some important properties such as specific surface area, pore size and pore size distribution of porous materials can greatly influence their working performances. The specific surface area is defined as the accessible area of the solid surface per unit mass of a material. Several techniques have been developed to determine specific surface area and pore size distribution.[14] It should be noted that different techniques are based on specific physical principles with probes of different sizes, and therefore are only valid in a certain pore-size range (**Figure 1.2**). The gas adsorption method is commonly used for the evaluation of microporous materials.[14] Adsorption can be clarified as chemical or physical adsorptions. In

the case of chemisorption (chemical adsorption), chemical bonds are formed between the adsorbent and the adsorptive whereas physisorption (physical adsorption) involves a readily reversible process based on weak intermolecular interactions (e.g., van der Waals forces). In gas adsorption measurements, physisorption is usually utilized to obtain information for surface area and pore size distribution of microporous materials.

Nitrogen (N_2) is the commonly used probe for surface area measurements at 77 K. Carbon dioxide (CO_2) , of relatively smaller kinetic diameter, is the recommended probe for determining the pore size distribution in the small micropore range of 0.4-1 nm at 273 K.[14] The detailed adsorption measurement procedure is described as follow: prior to the measurement, sample materials are degassed under high vacuum at elevated temperature to obtain a 'clean' surface and then placed into a sample cell. A known volume of N_2 or CO_2 is admitted stepwise to the sample cell, allowing the sample to reach an equilibrium uptake state, and the uptake volume of gas is recorded. The surface area can be then calculated using the volume of adsorbed nitrogen and the cross-sectional area of the probe molecule using BET (Brunauer-Emmett-Teller) theory,[15] an extension of Langmuir theory.[16]

The Langmuir model is derived from the equation below where *A* is the probe gases, *S* is the free adsorption sites and *AS* is the adsorbed molecule. *K*, the equilibrium constant of this system, can be defined as follow:

$$A + S \leftrightharpoons AS \qquad K = \frac{[\mathrm{AS}]}{[\mathrm{A}][\mathrm{S}]}$$

The equilibrium constant *K* can also be expressed using the fraction of surface coverage θ which is the ratio between the occupied adsorption sites (i.e., the adsorbed gas volume V_A) and the total available sites on the surface V_M (the gas volume used for a monolayer coverage), where *P* is the partial pressure of gas.

$$K = \frac{\theta}{P(1-\theta)} \qquad \theta = \frac{V_A}{V_M}$$

Combination of the above two equations gives the following equation:

$$\frac{KP}{1+KP} = \frac{V_A}{V_M}$$

The equation can be rearranged to give a linear function in the form of *y=mx + c*, where V_M and *K* can be obtained by calculation from the intercept and the slope of the resulting linear plot.

$$\frac{1}{V_A} = \frac{1}{KV_M}\left[\frac{1}{P}\right] + \frac{1}{V_M}$$

It is worth noting that Langmuir model makes the following assumptions when calculating surface areas[16].

1) All adsorption sites on the surface are equivalent and have the same opportunities to adsorb molecules.
2) There is negligible interactions between adjacent adsorbed molecules.
3) Adsorbed molecules are in an immobile state.
4) The surface can only adsorb a monolayer of molecules.
5) The adsorbate behaves as an ideal gas.

As the Langmuir theory does not relate closely to reality, BET theory extends the Langmuir theory to multilayer adsorptions to give the resulting BET equation:

$$\frac{P}{V_A(P-P_O)} = \frac{C-1}{CV_M}\left[\frac{P}{P_O}\right] + \frac{1}{CV_M}$$

where *P* is the equilibrium pressure of adsorbates at measured temperature, P_O is the saturation pressure of adsorbates at measured temperature, V_A is the volume of the adsorbed gas, V_M is the monolayer volume and *C* is the BET constant. In the range of 0.05 ≤ P/P_O≤ 0.35, a plot of P/P_O and $P/[V_A(P-P_O)]$ shows a linear relationship. The monolayer volume (V_M) can be determined using the slope (*A*) and intercept (L) as shown in the following equation:

$$V_M = \frac{1}{A+L}$$

The specific surface area (S_{BET}) of a material can be calculated from V_M as follows:

$$S_{BET} = \frac{N_A V_M \sigma}{m M_V}$$

where N_A is the Avogadro's number (6.022×10^{23} mol^{-1}), σ is the effective cross-sectional area of the probe molecule (16.2 Å^2 for nitrogen), m is the sample weight (g) and M_V is the molar volume of adsorbed gases at standard condition (22.414 L).

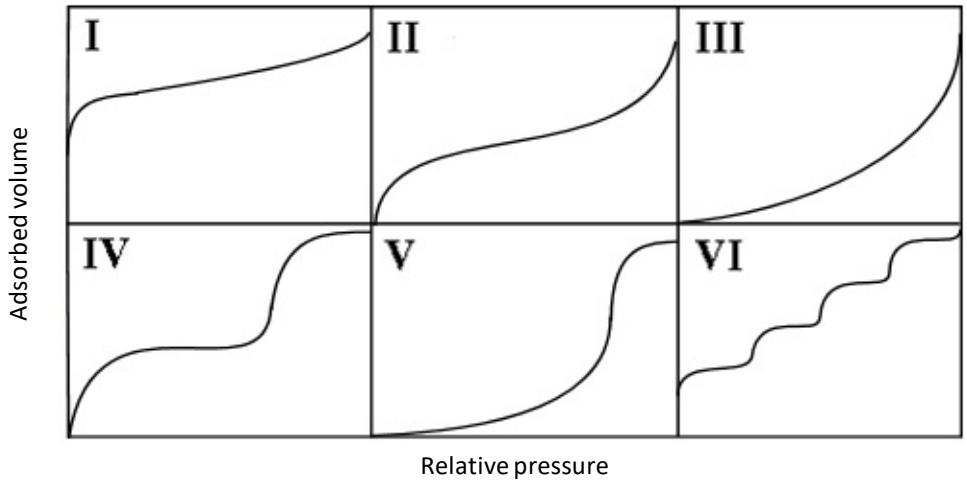

Figure 1.3 IUPAC classification of adsorption isotherms.

The plot of $P/[V_A(P - P_O)]$ against P/P_O is termed as an adsorption isotherm, which was classified into six categories by the IUPAC definition (**Figure 1.3**).[17] Type I is the typical isotherm for microporous materials showing a steep uptake at a very low relative pressure due to enhanced adsorptive-adsorbent interactions in narrow micropores. Type II, III and VI are the isotherms for nonporous or macroporous materials and type IV and V are the characteristic isotherms for mesoporous materials.

1.3 Membrane theory

A membrane is typically defined as ''*A phase or a group of phases that lies between two different phases which is physically and/or chemically distinctive from both of them and which, due to its properties and force field applied, it is able to control mass transport between these phases*".[18] The force field can arise from the gradient of pressure, temperature,

concentration or electric potential across the membrane, which drives permeants across the membrane.[19] Some membrane separation systems have already been implemented in industry successfully and their developing status is shown in **Table 1.1**.[19] For example, microfiltration, ultrafiltration and reverse osmosis have been well developed. Especially, reverse osmosis process for seawater desalination has solved the freshwater problem in many regions in the world. The energy consumption of reverse osmosis is around 4.5 kWh/m^3, and is an order of magnitude lower than that of the thermally driven separation process (~ 50 kWh/m^3).[19] However, thermally driven separations are still the dominant in industry which consumes up to 50% of the energy used in production lines to date.[20] Membrane separations are recognised as a promising technique to replace traditional separation techniques to reduce global energy cost and environmental pollution.

Table 1.1 Membrane technologies and developing status.[19]

Category	**Membrane separation Process**	**Status**
Developed industrial	Microfiltration Ultrafiltration Reverse osmosis Electrodialysis	Well established unit operations. No major breakthroughs seem imminent.
Developing industrial	Gas separation Pervaporation	A number of plants have been installed. Market size and number of applications served are expanding
To-be-developed industrial	Carrier-facilitated transport Membrane contactors Piezodialysis	Major problems remain to be solved before industrial systems will be installed on a large scale

Membrane gas separation is a more challenging process compared to the aforementioned membrane separation techniques (i.e. microfiltration, ultrafiltration and reverse osmosis) due to the small size differences between gases. For instance, in reverse osmosis, free water molecules *versus* hydrated cations and anions differs by over 100% in size, whereas O_2 and N_2 only have 5% difference in effective diameters.[21] With the development of polymer technology, polymer membranes with good gas selectivity have been achieved. The successful implementation of gas separation membrane in industry benefits from the production of anisotropic membranes in late 1960s which improved gas flux significantly.[4] Now successful applications of membrane technology has been realised in many fields, e.g.

air separation, hydrogen separation, natural gas upgrading and post-combustion carbon capture (**Table 1.2**).[4]

Table 1.2 Principal gas separation markets, producers and membrane systems (2000).[4]

Company	Principal markets/ estimated annual sales	Principal membrane material used	Module type
Permea (Air Products) Medal (Air Liquide) IMS (Praxair) Generon (MG)	large gas companies nitrogen/air ($75 million/year) hydrogen separation ($25 million/year)	Polysulfone, polyimide/polyaramide, Polyimide, tetrabromo polycarbonate	hollow fiber
GMS (Kvaerner) Separex (UOP) Cynara (Natco)	mostly natural gas separations carbon dioxide/methane ($30 million/year)	cellulose acetate	spiral-wound, hollow fiber
Aquilo Parker-Hannifin Ube GKSS Licensees	vapor/gas separation, air dehydration, other ($20 million/year)	polyphenylene oxide, Polyimide, silicone rubber	hollow fiber, plate-and-frame spiral-wound

During gas separation, a compressed feed gas mixture will pass the membrane surface which selectively permeates one component of the feed mixture. The gas separation mechanism is different depending on the pore size in the membrane (**Figure 1.4**)[19]: (i) **Knudsen diffusion** occurs when pore sizes are in the range of 15-2000 Å which is smaller than the mean free path of gas molecules. Large gas molecules collide with pore walls more frequently than small ones, thus large gas molecules need to pass through a longer pathway and permeate slower. (ii) **Molecular sieving** will predominate when pore size falls into the range of 4-15 Å. This separation is based on a size exclusion mechanism where the small gas molecules pass through pores, but large gas molecules are hindered. (iii) **Solution-diffusion** model is applied for dense polymer membranes which can effectively separate gas molecules with small size differences (*i.e.*, He/H_2, O_2/N_2 and CO_2/CH_4). The 'pores' in dense membranes are usually described as free volume elements (less than 5-10 Å) which are dynamic and generated by thermal motion of polymer chains. This model is comprised of three steps: gas molecules are firstly adsorbed into the membrane on the feed side, and then diffuse through the membrane matrix, and finally desorbs on the permeate side. Therefore, permeates are separated based on the different solubility and different mobility rate in the membrane medium.[19]

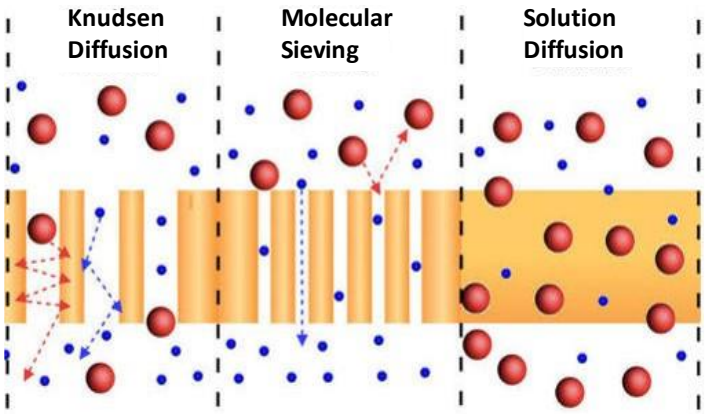

Figure 1.4 Membrane separation mechanism for gases.

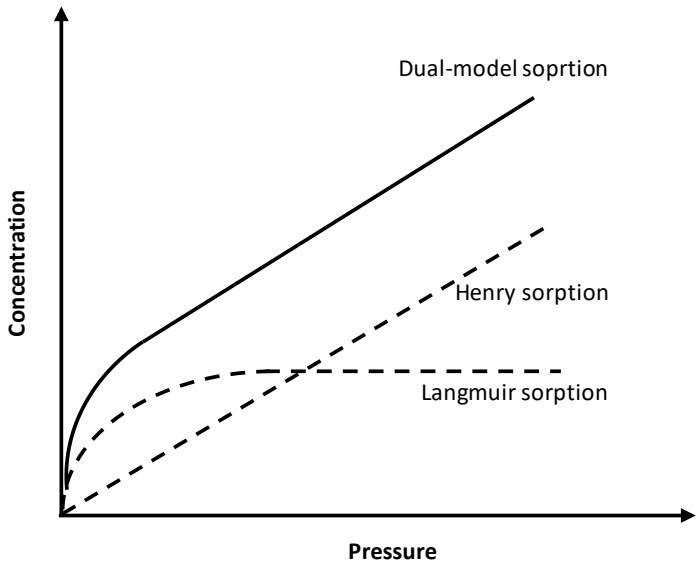

Figure 1.5 An illustration of the Henry, Langmuir and dual-model sorption.[19]

Unlike rubbery polymer, some glassy polymers (*e.g.*, PIMs) are constructed by stiff polymer chains and possess semi-permanent pores in the range of 5-15 Å due to the restricted polymer chain mobility. Therefore, their separation mechanism is a combination of the solution-diffusion model and molecular sieving model. [19] The different microstructures of rubbery polymers and glassy polymers lead to their distinct sorption behaviour. The gas sorption of rubbery polymers follows Henry's law where the gas concentration in the polymer membrane is proportional to the applied pressure. However, glassy polymers act as a 'dual-sorption model' (Henry's law and Langmuir-type adsorption) (**Figure 1.5**) owing to the two types of sorption sites in the polymers. The sorption in the continuous phase of glassy

polymers obeys Henry's law, whereas the sorption in the semi-permanent pores conforms to Langmuir-type adsorption and will cease when all the pores are filled.

1.4 Gas Separation

1.4.1 Transport Parameters

In terms of solution-diffusion model, permeability *P* can be expressed as the below equation,[19] where *P* is in units of Barrer (1 Barrer = 10^{-10} (cm^3 (STP)/cm s cmHg). Solubility coefficient (*S*) describes the volume of dissolved gas per unit volume of polymer per unit pressure (cm^3 cm^{-3} bar^{-1}). Diffusivity efficient (*D*) describes the rate of dissolved molecules moving within the membrane (m^2 s^{-1})

$$P = SD$$

For a gas mixture with two components A and B, the ideal selectivity **α** of a membrane is defined as the ratio of the gas permeability coefficients of the two components:

$$\alpha_{A/B} = \frac{P(A)}{P(B)}$$

This equation can be rearranged into the following form by combination with the equation $P = SD$, thus the ideal selectivity $\alpha_{A/B}$ can be described as a function of the solubility selectivity and diffusion selectivity.

$$\alpha_{A/B} = \frac{P(A)}{P(B)} = \frac{S(A)}{S(B)} \text{ X } \frac{D(A)}{D(B)} \qquad S_{\alpha_{A/B}} = \frac{S(A)}{S(B)} \qquad D_{\alpha_{A/B}} = \frac{D(A)}{D(A)}$$

The solubility of a gas in the membrane matrix depends on its condensability. Larger molecules have stronger intermolecular interactions and condense more easily in membranes than small molecules. Hence, the solubility coefficient increases with gas diameter (**Figure 1.6**). The diffusivity coefficient shows a converse trend to gas diameter because small molecules have less of a barrier to move between free volume elements in the

bulk polymer (**Figure 1.6**). When gas solubility contributes primarily to gas transport, the gas permeability follows the order: $CO_2 > H_2 > O_2 > He > CH_4 > CO > N_2$. This order is not strictly correlated to the size of molecules and thus is known as ''*reverse selective*'' (**Figure 1.7**).[22] In the case of molecular sieving, the membrane permeability increases when the gas molecule diameter decrease (this is known as 'forward selective').

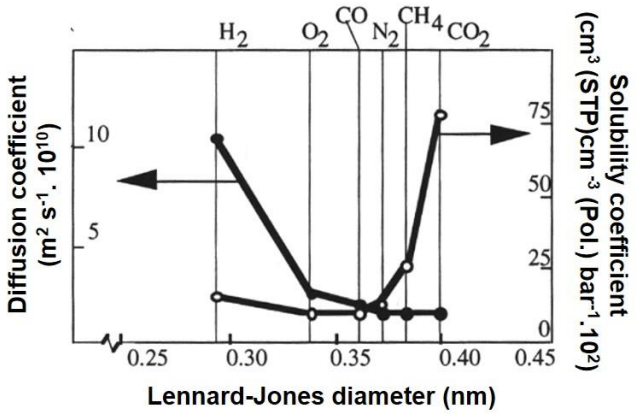

Figure 1.6 Lennard-Jones diameter *vs* diffusion and solubility coefficient for a rubber polymer membrane. [23]

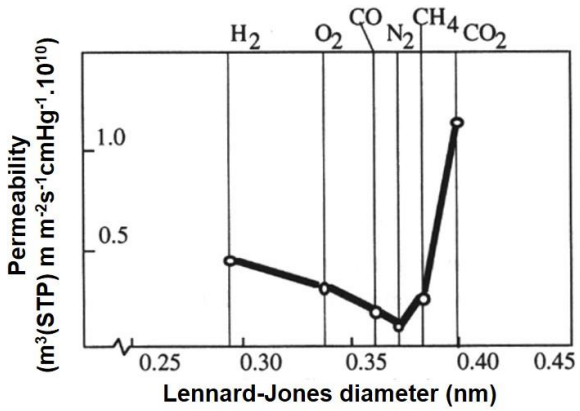

Figure 1.7 Lennard-Jones diameter *vs* permeability coefficient for a rubber polymer membrane.

1.4.2 Permeability/selectivity trade-off relationship, physical aging and plasticization

Over the past 40 years, a vast number of polymer membranes has been developed for gas separation. In 1991, Robeson collected over 300 literature data for polymer gas permeability

and plotted a double logarithmic plot of selectivity α_{ij} versus P_i (the permeability of the more permeable gas) (**Figure 1.8a**).[24] Empirical upper bounds of common gas pairs were established based on these plots to demonstrate the best separation performance of polymer membranes, known as the 1991 Robeson upper bounds. Since then, these upper bounds were used as a standard reference to evaluate the separation performance of a new polymer for gas separation via the position of the new polymer relative to the upper bound. Unfortunately, these upper bounds show a trade-off relationship between gas selectivity and permeability, i.e. a high permeability is usually linked to a low gas selectivity and *vice-versa*.[24] The theoretical analysis of Roberson upper bounds by Freeman suggested that tuning polymer structures can improve the location of upper bounds while their slopes remain unchanged as the latter depend only on the size difference of gas pairs. Freeman proposed that simultaneous increasing of free volumes (by increasing interchain distance) and backbone rigidity can achieve the improvement of both permeability and selectivity.[25] However, it is only effective when the increased interchain distance does not compromise the diffusivity selectivity. The emergence of rigid microporous polymers, such as PIMs and perfluorinated polymers, provided a large improvement in membrane gas separations, so that a series of new upper bounds were raised in 2008, known as *''2008 Roberson Upper Bound''* (**Figure 1.8a**).[26] Fine-tuning of structures of PIMs and PIM-PIs according to Freeman theory has further improved the performance of separation membranes and led to the redefinition of the more recent upper bounds for O_2/N_2, H_2/N_2 and H_2/CH_4 in 2015 by Pinnau (**Figure 1.8a**).[27]

Molecular modelling has demonstrated that PIMs have a unique microstructure consisting of a high concentration of both ultramicropores (< 0.7 nm, enhancing selectivity) and micropores (> 0.7 nm, enhancing permeability) (**Figure 1.8b**).[27] These micropores in rigid PIMs exists permanently on the timescale of gas permeation leading to fast gas diffusions and thus higher permeability compared to conventional polymers in which gas transports through transient openings formed by slow thermal motion of polymer chains. In addition, these micropores are interconnected with selective ultramicropores allowing small molecule transport while blocking large molecules (**Figure 1.8c**). As a result, the unique microstructure of PIMs contributes to a good combination of gas permeability and selectivity. In contrast, poly(1-trimethylsilyl-1-propyne) (PTMSP) contains a large fraction of micropores (**Figure 1.8b**), thus shows ultra-high permeability but extremely low selectivity. Unlike O_2/N_2, H_2/N_2

and H_2/CH_4 gas pairs, which separated mainly by diffusivity selectivity, the separation of CO_2/N_2 and CO_2/CH_4 is more complicated because they are controlled by both diffusivity selectivity and solubility selectivity. Therefore, structural prediction and synthetic development are more challenging, so that few data lie above the 2008 upper bounds and so at the beginning of this PhD research programme there had been no proposed revisions.

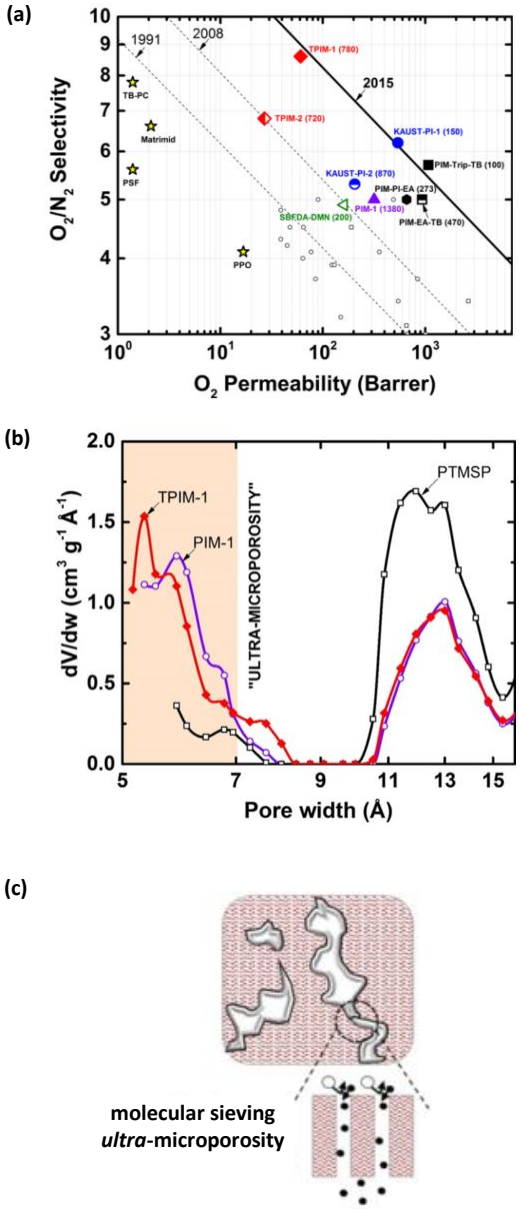

Figure 1.8 (a) Previous 1991 and 2008 (dashed lines) upper bound for O_2/N_2 separation and latest 2015 (solid line) upper bound defined by outstanding PIMs. There is a significant shift between 2008 and 2015 upper bounds. (b) Pore-size distributions obtained from nitrogen adsorption isotherm at 77 K using non-local density functional theory (NLDFT) model.[27]

Physical aging is a common phenomenon for glassy polymers, in which polymer properties experience reversible changes over time. This phenomenon arises from the nonequilibrium state of glassy polymers with excess free volume trapped below their glass transition temperature (**Figure 1.9**).[28] Glassy polymers attempt to approach their equilibrium state via local segment motions leading to a reduction in free volume. As a result, gas permeability sees a decrease coupled with an increase in selectivity over aging. Struik has reported that the driving force for physical aging which determines aging rate and extent is proportional to the differences between the current specific volume (v) and the specific volume at equilibrium (v_∞) (excess free volume = v - v_∞).[29] That is the volume reduction rate (i.e., permeability reduction rate) is proportional to the excess free volume of polymers.[29] For example, PTMSP (one of the most permeable polymers) with high free volume appears to age faster than conventional glassy polymers due to its greater excess free volume, showing a 68% decrease in N_2 permeability from 34000 Barrer to 11000 Barrer over only 27 days.[30] Apart from polymer structures, physical aging rate is also observed to be influenced by membrane thickness.[31-33] Thin films typically age more rapidly than thick ones, presumably due to the quicker diffusion of free volume to the surface of thin films. Indeed, physical aging cause a decrease in permeability, but also a significant enhancement in gas selectivity for some polymers, improving the overall gas separation.

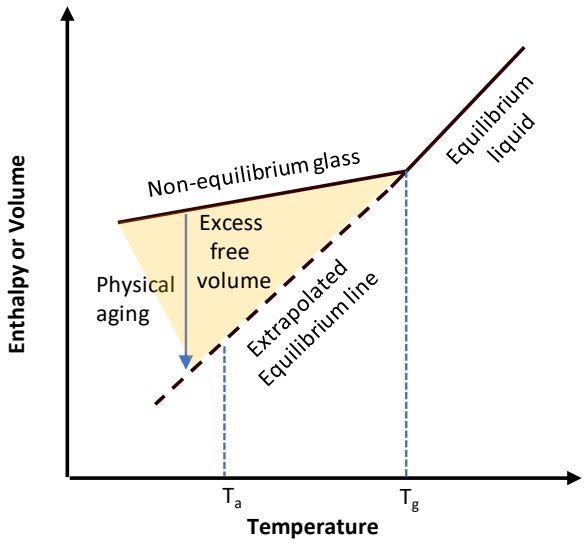

Figure 1.9 Schematic of physical aging influence on enthalpy or volume for glassy polymers as a function of temperature. T_g is the glass transition temperature for glassy polymers and T_a is the environment temperature at which the polymer undergoes aging.[28]

Another limitation of glassy polymers as separation membranes is sorption-induced plasticization. Condensable gases such as CO_2 and hydrocarbons can cause polymer swelling when their concentrations increase to a certain range in the polymer membrane, leading to the promotion of gas permeability (especially for large molecules) and thus a significant decrease in gas selectivity.[34-37] To date, plasticization has been effectively hindered by enhancing interchain interactions, such as chemical or thermal cross-linking[38-42] and introduction of hydrogen-bonding networks[43].

1.5 Commercially available materials for gas separation

As mentioned above, polymer membranes play an important role in gas separations and their market shows a substantial growth in recent years. During this time, several polymers has been used as common gas separation membrane materials, including polysulfone, cellulose acetates, poly(phenylene oxides) (PPO) and polyimides (PI) etc. Their gas permeability and selectivity are included in **Table 1.4** for comparison.

1.5.1 Polysulfones

Polysulfones are a class of glassy amorphous polymers composed of diphenylene sulfone repeating units (-Ar_1-SO_2-Ar_2-). They have three resonance structures as shown in **Figure 1.10**.[44] As sulphur atoms in the sulfone groups are in the highest oxidation state, they tend to withdraw electrons from the adjacent benzene rings. The C-S bonds show a double-bond character which limits polymer chain rotation and hence enhance the backbone rigidity.[44] In addition, the resonance structure improves the strength of the chemical bonds and provides a high chemical stability.[44] Commercial polysulfones are generally prepared via the nucleophilic aromatic polycondensation using halogenated diphenylsulfones and various bisphenols.[44] Most polysulfones have good solution processability as they have good solubility in *N*-methyl-pyrrolidone (NMP), tetrahydrofuran (THF) or dimethylacetamide (DMAC).[45] Bisphenol A polysulfone (PSF) is one of the earliest commercial membrane materials for gas separations (especially for O_2/N_2 and hydrogen separations) due to their excellent mechanical properties, high thermal stability (> 400 °C), good chemical stability, simple processability and low cost.[36, 46] In 1970s, Monsanto Company reported the first large-

scale membrane separation process based on the asymmetric hollow fibre membrane of PSF with a coating layer of silicone rubber.[47] Many following studies have been carried out to explore the relationship between the polysulfone structures and their gas separation performances. The symmetric methyl substituents on the phenyl rings (TMPSF) reduced chain-packing efficiency and simultaneously improved chain stiffness, resulting in a significant increase in gas permeability with a minor loss in gas selectivity compared with PSF.[48] The permeability of TMHFPSF can be further improved by replacement of CH_3 with bulkier group CF_3 while keeping comparable selectivity to TMPSF.[49] The increased free volume of TMHFPSF improved CO_2 sorption which induced plasticization when CO_2 pressure exceeded 15 bar, while PSF and TMPSF showed good plasticization resistance up to 20 bar.[50] This study illustrated that increasing chain rigidity while prohibiting chain packing can overcome the permeability/selectivity tradeoff relationship. The structural symmetry was also observed to influence the gas separation performance, i.e. symmetric bulky substitutions on the phenyl rings yielded less efficient packing structure leading to a higher gas permeability with a lower gas selectivity as compared to asymmetric substitutions.[51]

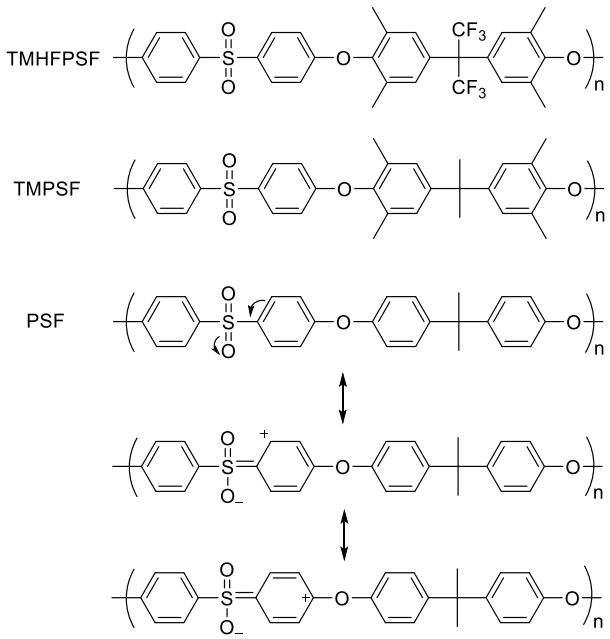

Figure 1.10 Resonance strucutres of poly(arylene ether sulfone).

1.5.2 Cellulose acetates

Cellulose acetates (CA) are prepared by acetylation of hydroxyl groups on cellulose using acetic anhydride or acetic acid with catalysts (e.g., H_2SO_4).[52] The CA polymers are generally designated as CA-DS, where DS represents the acetylation degree ($0 \leq DS \leq 3$). As shown in **Figure 1.11**, full esterification of hydroxyl groups on cellulose results in cellulose triacetate (CTA). Then CA with a specific acetylation degree can be synthesised via the hydrolysis of CTA under acidic or basic conditions.[52] CA polymers with different DS are soluble in organic solvent (e.g., acetone) so that can be processed into asymmetric membranes[53-55] or asymmetric hollow fibres[56-58] by casting method. CA membranes are relatively inexpensive because of the ease of manufacture and the availability of cheap raw materials (cellulose is abundant and can be obtained from renewable resource such as wood and cotton).[59] In mid-1980s, CA membranes were firstly utilised for natural gas upgrading (CO_2/CH_4) and air separations (O_2/N_2). Since then gas separation systems based on CA membranes has dominated the small-scale natural gas separation market because of the high cost and complexity of the traditional amine adsorption system for small-scale gas production.[59] However, several issues of CA membranes limited their application in large-scale gas separations in industry. The most remarkable one is the plasticisation which leads to a significant drop in CO_2/CH_4 selectivity under the practical mixed-gas conditions.[4, 36, 60] For example, the CO_2/CH_4 selectivity is about 35 for CA membranes in the pure gas measurement, but drops to 12-15 under practical condition (mixed-gas feed of 20% CO_2 and 80% CH_4 at 40 bar and 50 °C).[61] Much research has been carried out in order to mitigate these issues, e.g. (i) incorporation of microporous fillers in CA membranes (e.g., zeolites,[62, 63] MOF [64, 65] or silicon species [66-68]), (ii) stabilizing CA matrix by cross linking to supress plasticization.[69] However, these modification achieved only limited improvements. On the other hand, the development of new materials is expected to make a big step in membrane gas separations.

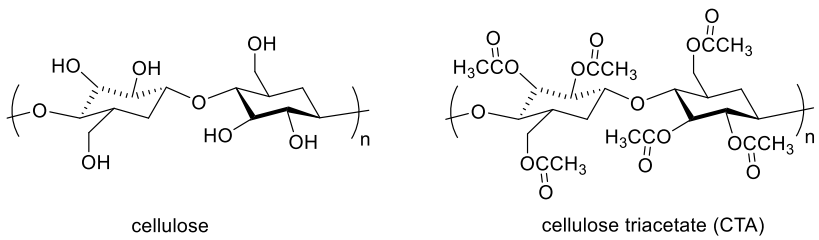

Figure 1.11 Chemical structures of cellulose and cellulose triacetate.

1.5.3 Polyphenylene oxides

Poly(2,6-dimethyl-1,4-phenylene oxide) (PPO) is the most widely studied polyphenylene oxides as membrane materials for gas separations.[70] Linear PPOs with high molecular weight are usually synthesised via oxidation coupling polymerisations with stoichiometric oxygen as an oxidizing agent and CuCl as a catalyst in pyridine solution (**Figure 1.12**).[44, 71] The most attractive property of PPO as gas separation membrane is its unexpected high gas permeability compared to other glassy polymers such as polysulfones and CAs (**Table 1.4**).[72] This is contributed from the contorted ether linkage and the short length of repeating units leading to inefficient chain packing.[73] However, the looser structure results in the comparatively low selectivity of PPO (**Table 1.4**). To achieve better gas separation performance, many modifications have been conducted on PPO. For example, the dimethyl groups in PPO was replaced with two phenyl groups, leading to an increased selectivity at the cost of permeability.[73] Several polar groups, such as carboxyl,[74, 75] nitro,[76] bromine[77-79] and sulfate groups[80] were introduced to PPOs aiming for improvements of gas selectivities. Weakly polar groups (e.g. bromo group) enhanced polymer rigidity by restricting the rotation freedom around the ether linkage, and simultaneously increased polymer free volume. The substitution gave an increase in gas permeability with a minor loss in selectivity.[77-79] However, hydrogen-bond-forming groups (e.g. -COOH) lead to a significant decrease in gas permeability albeit with an increase in gas selectivity due to a notably reduced free volume.[74, 75, 80]

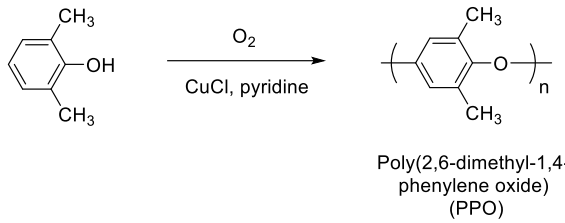

Figure 1.12 Synthesis of PPO via oxidative coupling polymerisation.

1.5.4 Polyimides

Polyimides exhibit a high gas permeability together with a high selectivity for CO_2/CH_4 and O_2/N_2 gas pairs in comparison to other commercial polymers.[5, 36, 81] For example, Baker

reported the replacement of CA (selectivity ≈ 12-15) with more selective polyimides (20-25) for natural gas upgrading can reduce the membrane area and recycle compressor duty by~ 40% and~ 35%, respectively.[4] Polyimides are typically synthesised via polycondensation of dianhydride and diamine monomers, involving a cycloimidization at high temperature.[82] Matrimid 5218 (**Figure 1.13**) is a commercial polyimide composed of diaminophenylindane (DAPI) and 3,3'-4,4'-benzophenone tetracarboxylic dianhydride (BTDA), and has been extensively investigated in gas separation membranes.[33, 83, 84] Matrimid 5218 exhibits a CO_2 permeability of 10 Barrer and a CO_2/CH_4 selectivity of 36,[85] which is higher than polysulfones and cellulose acetates (**Table 1.4**). Gas separation performance of polyimides can be tuned by changing monomer structures. The polymer chain rigidity and free volume can be improved by adding substituents on the ortho position to the imide rings which will restrict the rotation around the single bonds between the phenyl ring and the imide ring.[86] Therefore, polyimides with methyl substitutions on the ortho position usually have higher gas permeability but with a lower gas selectivity.[86] In addition, the introduction of -C(CF_3) groups also showed an increase in chain rigidity leading to an increased gas permeability.[3] One disadvantage of polyimides as separation membrane is the significant sorption-induced plasticization which causes gas selectivity loss in mixed-gas system.[87] For example, the CO_2/CH_4 selectivity of Matrimid 5218 decreased by about 45% in a CO_2/CH_4 (55/45 mol%) mixture when the total feed pressure increased from 5 to 50 bar.[83] Many efforts have been made to supress the plasticization, such as chemical cross-linking[88-92], thermal treatments[83, 93-97] and blend with porous fillers[85, 98], but usually brings a decreased gas permeability.

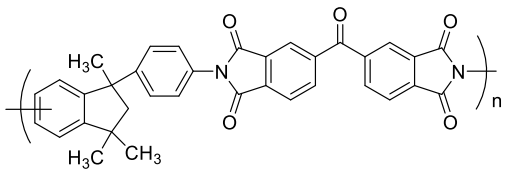

Figure 1.13 Chemical structure of Matrimid 5218 polyimide.

Overall, most of the commercial membrane materials possess high gas selectivity but low permeablity due to the low free volume with the permeability data points located below the 1991 Roberson upper bounds (**Figure 1.14**). The membrane separation techique based on these commerical materilas is now widely used for small-scale gas separations and has been integrated with traditional separation techniques.[4] On the othe hand, membranes made from metal-organic frameworks (MOFs), zeolites and polymer cages possess good

productivity and efficiency for separations due to their interconnected pores and uniform pore sizes. However, they are costly and large defect-free membranes (a few thousand to a million m^2) are difficult to be made using these materials.[61] In recent years, soluble microporous polymers have emerged and provided a large step-change in membrane gas separation.

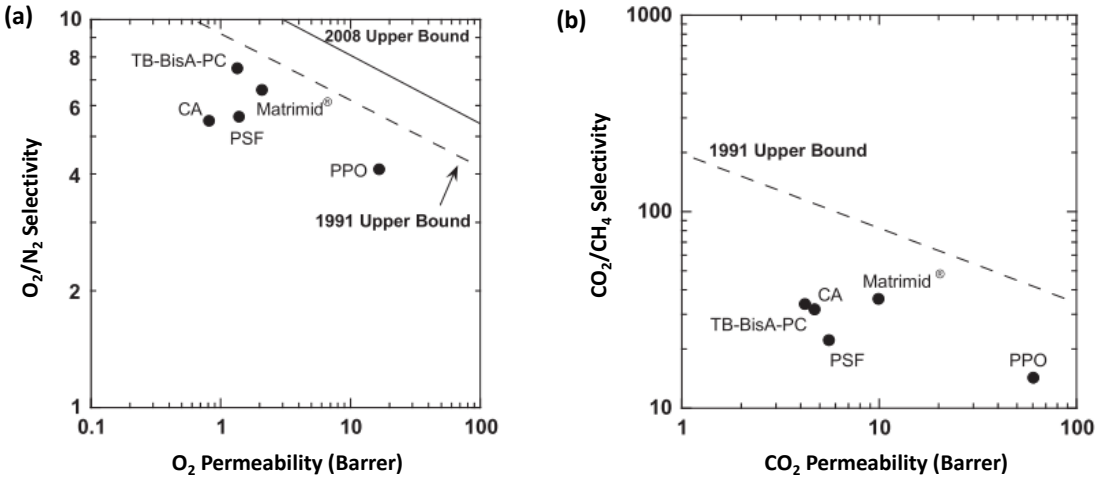

Figure 1.14 Gas separation performance for commercial membranes aginst 1990 (dashed line) and 2008 (solid line) Roberson upper bounds for (a) O_2/N_2 and (b) CO_2/CH_4.[36]

Table 1.4 Gas transport properties for commercial materials and PIMs

Polymer	Pemeability (Barrer)					Selectivity			Ref.
	H_2	N_2	O_2	CH_4	CO_2	H_2/N_2	O_2/N_2	CO_2/CH_4	
PSF [a]	14	0.25	1.4	0.25	5.6	56.0	5.6	22.4	47
CA-2.45 [b]	12	0.15	0.82	0.15	4.8	80.0	5.5	32.0	54
PPO	61	4.1	16.8	4.3	61	15.0	4.1	14.0	71
Matrimid [c]	18	0.32	2.1	0.28	10	56.0	6.6	36.0	33, 85, 98
Teflon AF2400	2090	480	960	390	2200	—	2.0	5.7	100
Teflon AF1600	550	110	270	80	520	—	2.4	6.5	100
Cytop	170	5.0	16	2.0	35	—	3.2	18.0	100
PTMSP	13900	5510	7850	14500	28100	2.5	1.4	4.5	115
PIM-1 [d]	5010	823	2270	1360	13600	6.1	2.8	10.0	148
PIM-1 (1200)	2440	125	600	159	2840	19.5	4.8	17.9	152
PIM-SBF (180 µm) [d]	6320	786	2640	1100	13900	9.0	3.5	13.8	148
PIM-SBF (80 µm, 2088)	2190	87.5	486	102	2410	25.0	5.6	23.6	152
PIM-SBF-2	9160	1150	3820	2020	22300	8.0	3.2	11.0	152
PIM-SBF-2 (1295)	4240	166	910	184	3870	25.6	5.5	21.0	152
PIM-SBF-5	5590	1080	2750	2480	16400	5.2	2.6	6.6	152
PIM-SBF-5 (1439)	4710	550	1870	925	10000	8.4	3.4	10.8	152
PIM-EA-TB [d]	7760	525	2150	699	7140	14.8	4.1	10.2	1
PIM-EA-TB (470)	4442	188	933	219	2644	23.6	5	12.1	149
PIM-Trip-TB [d]	8039	629	2718	905	9709	12.8	4.3	10.7	149
PIM-Trip-TB (100)	4740	189	1073	218	3951	25.1	5.7	18.1	149
PIM-BTrip-TB [d]	9980	926	3290	1440	13200	10.8	3.6	9.2	150
PIM-Btrip-TB (166)	4280	216	1166	283	4147	19.8	5.4	14.7	150
TPIM-1 [e]	2666	54	368	50	1549	50.0	6.8	31.0	151
TPIM-1 (780)	1105	7.1	61	—	—	155.6	8.6	—	29
TPIM-2 [e]	655	18	101	18	434	37.0	5.7	24.0	151
TPIM-2 (720)	354	4	27	—	—	88.5	6.8	—	29
PIM-TMN-Trip [d]	16900	2230	7470	3420	33300	7.6	3.4	9.7	141
PIM-TMN-Trip (365)	9840	727	3160	943	14100	13.5	4.3	15	141
PIM-TMN-Trip-TB [d]	6100	396	2030	710	6060	15.4	5.1	8.5	141
PIM-TMN-SBI [d]	7190	1080	3200	2100	17500	6.7	3.0	8.3	141

[a] CO_2 and CH_4 at 10 bar and 35 ˚C; O_2, N_2 and H_2 at 1 bar and 35 ˚C.

[b] CA with 2.45 degree of acetylation, 1 bar and 35 ˚C.

[c] O_2, N_2 and CH_4 at 35 ˚C and 2 bar, CO_2 at 3.4 bar and 35 ˚C, H_2 at 4.1 bar and 35 ˚C.

[d] Methanol treated, air-dried and tested at 1 bar and 25 ˚C.

[c] Methanol treated, air-dried, then dried under vacuum at 120 ˚C overnight and aged 15 days, and tested at 2 bar and 25 ˚C.

1.6 Soluble microporous materials for gas separation

1.6.1 Perfluoropolymers

Perfluoropolymers possess excellent properties such as chemical and thermo-oxidative stabilities, arising from the stable C-C (360 KJ/mol)[99] and C-F (485 KJ/mol)[99] bonds and the protective sheath of fluorine atoms around the carbon backbone.[100, 101] The first generation of perfluoropolymers (i.e. polytetrafluoroethylene (PTFE)) was not investigated in depth in gas separation applications.[102] This is mainly due to their semicrystalline nature and poor solubility in common solvents leading to a low gas permeability and poor processability.[102] The breakthrough of perfluoropolymers in gas separation was the development of Teflon AF by DuPont in the 1980s (**Figure 1.15**).[103] The Teflon AF series are copolymers consisting of tetrafluoroethylene and 2,2-bis(trifluoromethyl)-4,5-difluoro-1,3-dioxole, which can be dissolved in fluorinated solvents and made into membranes by membrane casting methods. The adjacent dioxole rings in Teflon AF structures cannot rotate freely because of the high energy barrier (ca. 60 KJ/mol), and their bulky structure frustrates the efficient chain packing. [6] As a result, Teflon AF polymers are amorphous with high free volume and hence high gas permeability. This is evidenced by molecular modelling [104] and the positron annihilation lifetime spectroscopy (PALS),[105] which indicated the presence of large micropores in Teflon AF. This new generation of perfluoropolymers demonstrated exceptional gas separation performances and helped to redefine the 2008 Roberson upper bounds for light-gas pairs, including N_2/CH_4, He/CH_4, He/N_2 and He/CO_2.[26, 100] The exceptional performance originates from the unique solubility property of hydrocarbons in fluoropolymers, i.e. hydrocarbon-vapours (*e.g.* CH_4) have low solubility compared to light gases (*e.g.* N_2) because of the C-F bonds,[100] and simultaneously, the low hydrocarbon sorption of perfluropolymers improves their plasticization resistence.[100] For example, Cytop showed stable selectivity with in the whole pressure range for propylene/propane separations, while polyimides membranes drop significantly from a high selectivity of 8 to *ca.* 1.[100] Therefore, perfluoropolymers can be used as membrane materials for many challenging separation applications, such as hydrocarbon gas pairs, where polymers tolerating high level of plasticizing species are desired.

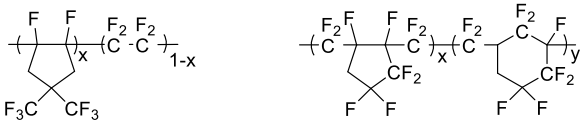

Teflon AF1600 (x=0.65)
Teflon AF2400 (x=0.87)

Cytop x >> y

Figure 1.15 Chemical structure of perfluoropolymers.

1.6.2 Substituted polyacetylenes

In 1983, Masuda *et al.*[106] reported a substituted polyacetylene, poly(1-trimethylsilyl-1-propyne) (PTMSP) (**Figure 1.16**), with an outstandingly high gas permeability. The extremely high gas permeability is mainly attributed to its ultrahigh fractional free volume (as large as 20-34%).[104, 107-109] PTMSP chains are highly rigid due to the conjugated double bonds structure along the main chain.[110] The high backbone stiffness and bulky trimethylsilyl side groups force the backbone folding into contorted structure and hinder polymer chain packing, leading to the ultrahigh free volume. In the solid state, the rigid and contorted polymer chains yield polymers with large connected micropores (around 0.68 nm in radius) as demonstrated by molecular modelling [104] and PALS [105, 111]. Large connected micropores lead to high gas diffusivity coefficients, and the high free volume provides large adsorption sites and hence give rise to high solubility coefficients. The combination of high diffusivity coefficients and solubility coefficients gives ultra-high gas permeability (one of the most permeable polymers to date) along with extremely low selectivity which limited its practical applications (**Table 1.4**). Much research on the introduction of substituents on polyacetylenes was carried out to investigate the structure-performance relationships.[112-115] The indanyl group acted as an efficient interchain spacer which improved the gas permeability of the polyacetylene, and thus indan-containing poly(diphenylacetylene) became the most permeable polymer to date.[114] However, the long *n*-alkyl and phenyl groups increased the packing efficiency leading to a moderate increase in gas selectivity but a notable decrease in permeability.[113] In general, the permeability/selectivity tradeoff trend was observed for most of these substituted polyacetylenes. Another limitation of PTMSP as separation membranes is the rapid physical aging,[116-119] i.e. the gas permeability of PTMSP decreases significantly over time because of the collapse of large pores.[117] For example, the CO_2 permeability decreased by 70% after storage for one year (29796 to 8045 Barrer).[117] The aging history can be reversed by soaking the membrane in a non-solvent (e.g. ethanol or methanol).[118, 120] Alternatively,

crosslinking,[121, 122] addition of nanoparticles or microporous fillers[123-127] have also been tried to mitigate the physical aging.

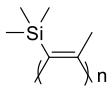

Figure 1.16 Chemical structure of PTMSP.

1.6.3 Thermally rearranged polymers

Park *et al.* reported a new family of polymeric membranes termed as thermally rearranged (TR) polymer membranes.[128] TR polymer membranes are achieved using a post-membrane fabrication method via a thermal rearrangement of polyimide membranes which have thermally labile substituents on the ortho position to the imide rings. Thermal rearrangement is a thermal reaction where the poly(hydroxyimide) precursors are converted into polybenzoxazole (PBO) with the loss of carbon dioxide at high temperature (350-450 ˚C) under an inert atmosphere (**Figure 1.17**).[129, 130] The polymer structures undergo two major rearrangements (**Figure 1.17**) during thermal treatment, i.e. the meta- and para-linked position yields random chain conformations, and then converting to a single long flat plane from the relatively flexible, twisted short flat planes to generate greater rigidity.[128] Molecular modelling and PALS demonstrated that the structural rearrangements resulted in larger, better-connected free-volume elements with narrower size distribution as compared to the precursor polymers.[128] As a result, the gas permeabilities of TR polymers are generally two orders of magnitude or more higher than those of the precursor membranes with higher gas selectivities achieved simultaneously.[128, 131, 132] In particular, TR polymers show outstanding separation performance for CO_2/CH_4 gas pairs, with the data points located above the 2008 Roberson upper bound.[26] The other above mentioned polymers usually suffer from plasticization, i.e. the CO_2/CH_4 selectivity decrease significantly in mixed-gas system, but in contrast, TR polymers exhibit strong plasticization resistance in mixed-gas system even when the CO_2 partial pressure increased up to 20 bar.[128] The imidization methods of the precursor polyimides were observed to have a profound impact on the gas transport property of TR polymers.[133] Hydroxyl-containing polyimide are typically synthesised by thermal imidization, while acetate-containing polyimides are achieved by chemical imidization. After thermal rearrangement, these two polyimide precursors generate TR polymers with the same

chemical structure but different gas transport properties. The acetate groups appear to generate large free volume in the TR polymers and thus increase the gas permeability.[133] Although the high thermal and chemical stability and strong plasticization resistance of TR polymers make them promising materials for gas separations, their practical application is limited by the relatively poor mechanical property of TR membranes due to the high thermal treatment temperature.[134]

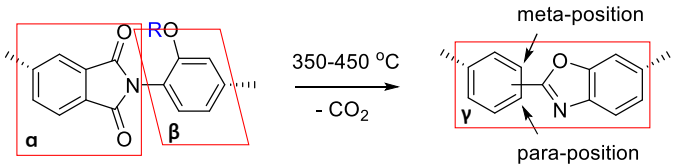

Thermal imidization R: H

Chemical imidization R: $COCH_3$

Figure 1.17 General scheme of thermal rearrangement of poly(hydroxyimide)s (α plane, phthalic imide ring; β plane, ortho-funcational phenylene ring; γ plane, newly created bezoxazole-phenylene ring).

1.6.4 Polymers of intrinsic microporosity

Polymers of intrinsic microporosity (PIMs) are a class of linear or networked polymers featuring 'intrinsic microporosity' which is defined as "a continuous network of interconnected intermolecular voids, which forms as a direct consequence of the shape and rigidity of the component macromolecules''.[135] In 2004, the term 'Polymer of intrinsic microporosity (PIMs)' was first formally introduced by McKeown and Budd.[136] PIMs are designed to have a wholly fused-ring contorted backbone which has high rigidity. Such contorted and rigid polymer chains cannot pack efficient when polymer in the solid state, providing PIMs with high free volume. This design principal was corroborated by high nitrogen uptake of PIMs at low pressures, indicating high microporosity densities (**Figure 1.18**).[27] The BET surface area of PIMs are 2 orders of magnitude higher than that for conventional polymer, e.g. PPO. In addition, linear PIMs have good solution processability making them promising membrane materials for a wide-range of applications, such as pervaporation,[137-139] gas separation[1, 140, 141]and ion-selective membranes[142-145].

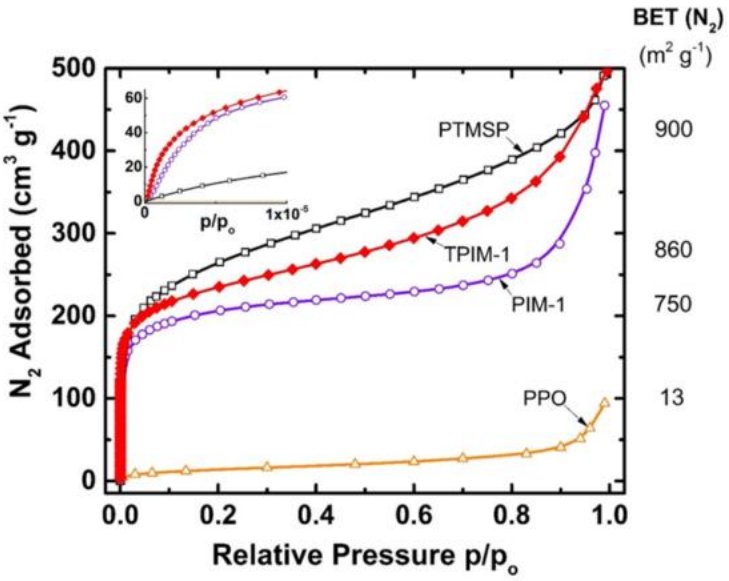

Figure 1.18 Nitrogen adsorption isotherms obtained at 77k. The BET surface areas are listed on the right.[27]

1.6.4.1 Rigid, three-dimensional (3D) ladder polymers of intrinsic microporosity

The initial PIMs were synthesised via the benzodioxin formation reaction through the double nucleophilic aromatic substitution (S_NAr) of biscatechol and tetrahalogenated monomers.[146] According to the design principle, at least one of the monomers are contorted to ensure a kinked structure of the resulting polymer chains. The first PIM (named PIM-1) was prepared through the S_NAr reaction using two commercially available monomers, 2,4,5,6-tetrafluoroterephthalonitrile (TFTPN) and 5,5',6,6'-tetrahydroxy-3,3,3',3'-tetramethyl-1,1'-spirobisindane (TTSBI), (**Figure 1.19**) at 65˚C in anhydrous dimethylformamide (DMF) for 70 h.[147] The resulting PIM-1 has a high molecular weight and a good membrane-forming capability. The TTSBI monomer contains a tetrahedral carbon fused by two rings and exhibits a non-linear V-shaped geometry, affording a contortion site. A ladder structure is then achieved after the formation of dioxin linkages and lead to a significantly limited rotation freedom of polymer chains compared to the conventional polymers. The rigid, contorted ladder backbones provide PIM-1 with abundant microporosity as indicated by the high surface area (750 m^2 g^{-1}, **Figure 1.18**). In gas separation applications, PIM-1 exhibited promising performance with a high permeability and a moderate selectivity and contributed to the redefinition of the 2008 Robeson upper bounds (**point 1, Figure 1.22**).[147]

In an effort to improve the gas separation performance according to Freeman theory, the McKeown group designed a new PIM (PIM-SBF) utilizing spirobifluorene in place of spirobisindane units.[148] Molecular modelling indicated that spirobifluorene is more rigid than spirobisindane due to the additional fused benzene rings in spirofluorene, limiting the movement around the spiro-centre. PIM-SBF exhibited similar permeabilities as PIM-1, but a better selectivity. The gas separation data point of PIM-SBF (**point 2, Figure 1.22**) lies above the 2008 Roberson upper bound for technologically relevant gas pairs: O_2/N_2, CO_2/CH_4, CO_2/N_2, H_2/N_2. This improvement in performance is ascribed to the higher chain stiffness and thus an enhanced diffusivity selectivity and greater molecular sieving.

The inherent flexibility of the spiro-centers and dioxin linkages motivated the design of new monomers with greater shape-persistence. Molecular modelling of potential structures suggests that bridged bicyclic molecules are highly stiff compared to the spiro-centers and dioxin linkage. According to this result, the McKeown group reported a wholly new PIM (PIM-EA-TB) which was prepared utilizing ethanoanthracene (EA) as the building block via a new polymerisation method, where diamine monomers undergo condensation reactions, with formaldehyde or its equivalent, to generate a bridged bicyclic structure named Troger's base (TB).[1] The highly rigid, contorted ladder structure of PIM-EA-TB contributes to its extremely high surface area (1028 $m^2\ g^{-1}$). The gas permeabilities and selectivities of PIM-EA-TB are simultaneously increased as compared with those of spiro-contorted PIMs, especially for air separation (O_2/N_2) and gas pairs that include H_2. Hence, the data point of PIM-EA-TB (**point 5**) lies far above the 2008 upper bound for O_2/N_2, H_2/N_2, H_2/CH_4 and H_2/CO_2 (**Figure 1.22**). The remarkable enhancement in performance is attributed to its superior polymer stiffness resulting in an improved molecular sieving which favours the transport of small molecules (e.g., H_2, O_2) over large molecules (e.g., N_2, CH_4). Moreover, hydrogen is more permeable than carbon dioxide for PIM-EA-TB which is different from most of the PIMs, further highlighting its enhanced size-sieving property. Overall, these results confirm the importance of polymer backbone rigidity in improving the selectivity.

Polybenzodioxin (nucleophilic aromatic substitution reaction)

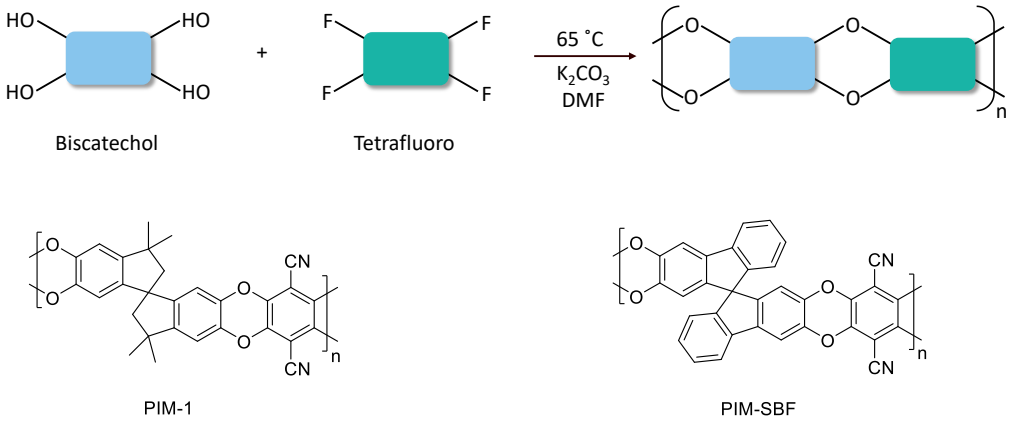

Tröger's base (TB) polymerisation

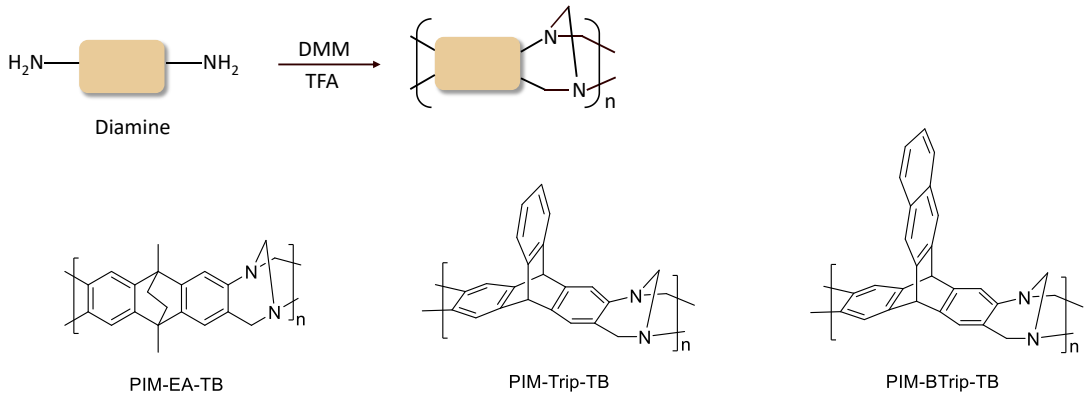

Figure 1.19 Synthesis scheme and polymer structures for polybenzodioxin polymers and TB polymers

The bridgehead methyl substituents on PIM-EA-TB was designed to increase interchain distance to promote permeability. However, the turnstile-like rotary thermal motion of the methyl substituents facilitate transport of large molecules and thus reduce gas selectivity. In order to further improve size selectivity of polymers, triptycene was used to maintain the interchain distances, and the bridgehead methyl substituents were removed aiming for the improvement of gas selectivities.[149] As a result, PIM-Trip-TB (**point 6**) gave an increase in both gas selectivities and permeabilities relative to PIM-EA-TB (**Figure 1.22**). From the gas permeability and adsorption data, the enhanced performance of PIM-Trip-TB is attributed to the greater diffusivity selectivity arising from the both higher chain rigidity and higher amount of ultramicropores than those of PIM-EA-TB. Following this work, the McKeown group developed a new semi-ladder polymer PIM-BTrip-TB synthesized via TB polymerisation using benzotriptycene (BTrip) as the monomer, which is an extended structure of triptycene

and expected to provide polymers with high free volume.[150] The incorporation of benzotriptycene increased gas permeability at the cost of gas selectivity. Even though, PIM-BTrip-TB (**point 7**) still exhibit promising gas separation performance with the data point located at or above the 2008 Roberson upper bounds for CO_2/CH_4, O_2/N_2, H_2/N_2 and H_2/CH_4 (**Figure 1.22**).

1.6.4.2 Rigid, two-dimensional (2D) ladder polymers of intrinsic microporosity

A few ladder polymers with highly rigid and ribbon-like macromolecular structure have been synthesised to date. They show a strikingly different structure with the abovementioned PIMs because spiro-centers or TB structure which exhibit a 3D propagation. In 2014, Ghanem *et al.* first reported two full-ladder polymers TPIM-1 and TPIM-2 which were prepared by self-polycondensation using substituted triptycene monomers containing dihydroxyl on one end and difluoro groups on the other end.[151] The self-polymerisation gives high molecular weights but without strict stoichiometric control. Both TPIM-1 (**point 8**) and TPIM-2 (**point 9**) showed excellent gas separation performances with data point locating over the 2008 Roberson upper bounds (**Figure 1.22**). The work also focused on the effect of the bridgehead substituents of triptycene on gas transport, showing that TPIM-1 with branched isopropyl groups gave higher gas permeability and selectivity than TPIM-2 (with linear propyl units) due to the simultaneously enhanced concentration of ultra-microporosity and microporosity. Although it is not as permeable as aforementioned TB polymers, TPIM-1 showed extraordinary gas selectivity at such a high gas permeability level.

Later, the McKeown group reported a new 2D polymer PIM-TMN-Trip with ultrahigh permeability similar to that of PTMSP (one of the most permeable polymers to date) but with substantially higher selectivity than PTMSP (**Table 1.4**).[141] The effect of polymer morphology on gas transport was firstly investigated in detail in this work. The 2D PIM-TMN-Trip was prepared through an S_NAr reaction using a substituted triptycene biscatechol and tetrafluoroterephthalonitrile (TFTPN) monomers. The fused tetramethyltetrahydronaphthalene (TMN) group on the triptycene enhances the 2D aspect ratio and can improve the polymer solubility. To compare, a 3D PIM-TMN-SBI with chains contorted in three-dimensions was synthesized using the same polymerisation reaction. Notably, PIM-TMN-Trip was the most permeable PIM reported to date (**Figure 1.22**) with the

permeability around twice that of PIM-TMN-SBI, and an even higher selectivity (**Table 1.4**). This result is confirmed with the molecular simulations that the packing of 2D polymer chains in a 3D amorphous matrix can generate more microporosity compared to 3D polymer chains (**Figure 1.20c**). This conclusion is further confirmed by the comparison of PIM-TMN-Trip with 3D PIM-TMN-Trip-TB. PIM-TMN-Trip-TB was prepared using a nearly identical triptycene unit without methyl substituent on the bridgehead via TB polymerisation to create the 3D polymer chains (**Figure 1.20a**). However, PIM-TMN-Trip-TB only showed moderate permeability which is 3-5 times less than that of 2D PIM-TMN-Trip (**Table 1.4**). The good combination of permeability and selectivity drives PIM-TMN-Trip (**point 10**) to the unpopulated area over the Roberson plots for CO_2/N_2 and CO_2/CH_4 (**Figure 1.22**).

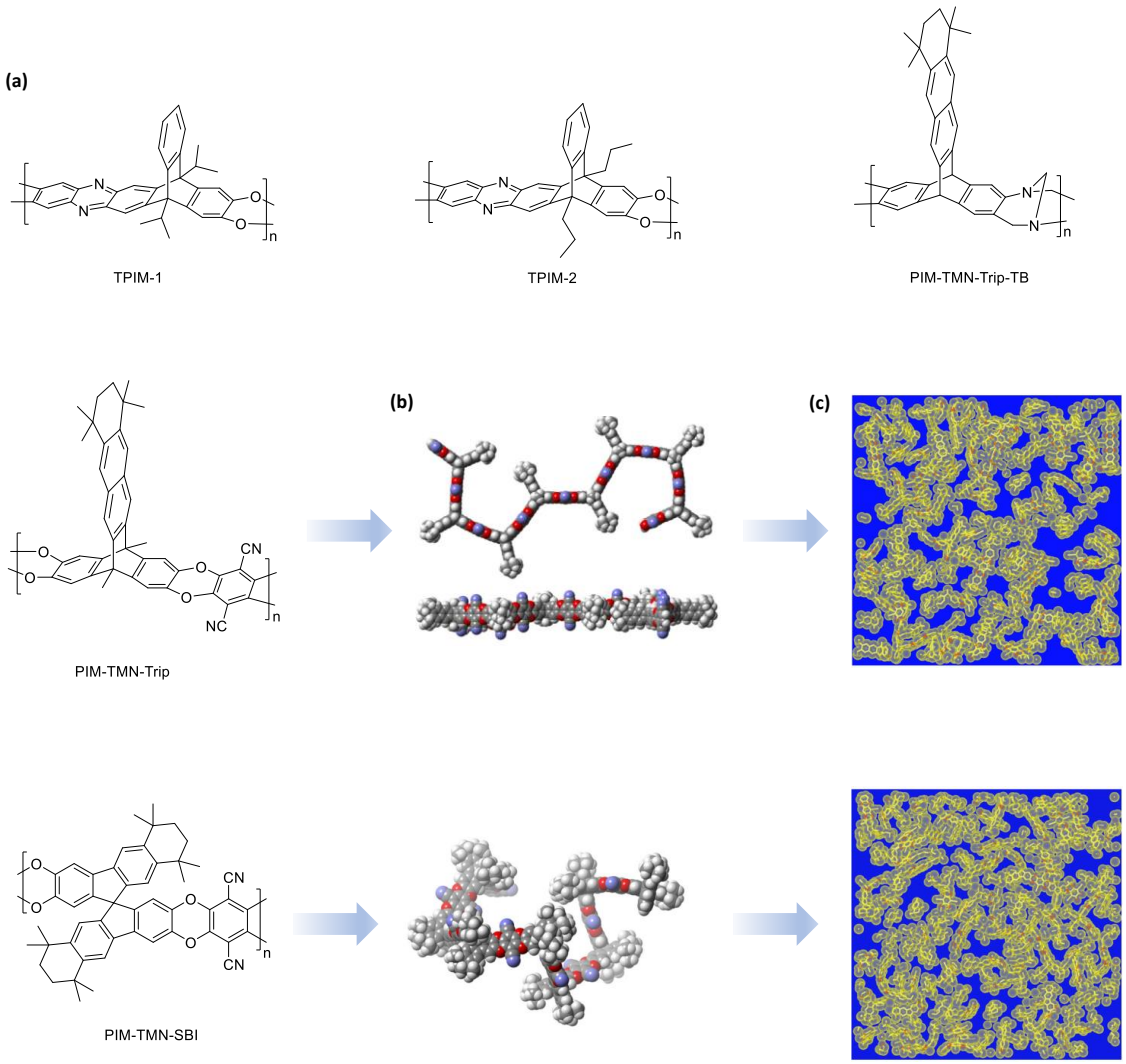

Figure 1.20 (a) polymer structures for 2D PIMs (TPIM-1, TPIM-2 and PIM-TMN-Trip) and 3D PIMs (PIM-TMN-SBI and PIM-TMN-Trip-TB) (b) The energy-minimized conformation of chain fragments for 2D

PIM-TMN-Trip and 3D PIM-TMN-SBI (c) Molecular simulated packing (9 × 9 × 9 nm^3) for PIM-TMN-Trip and PIM-TMN-SBI

1.6.4.3 Substituent groups on the PIM chains

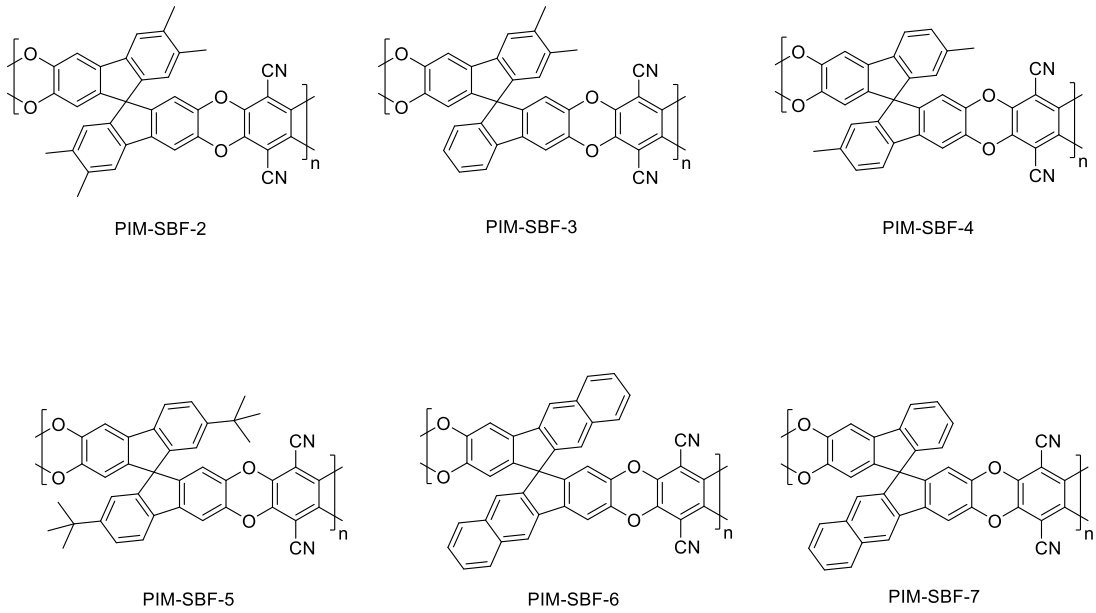

Figure 1.21 Structures of PIMs-SBF with various substituent groups.

The previous sections demonstrated that the promotion of the overall separation performance can be achieved by changing building units to increase backbone rigidity and interchain distances. The introduction of substituents on the polymer backbone is another way to tune gas separation performance. Macromolecular packing simulation has illustrated that methyl substituents on SBF unit will generate greater intrinsic microporosities.[152] To explore the effect of substituent groups, different substituents were introduced to the SBF unit on PIMs-SBFs, such as methyl, t-butyl and fused benzo groups (**Figure 1.21**).[152] Unfortunately, fused benzene substituted PIM-SBFs are insoluble and cannot be solvent-casted into films for gas permeability measurements. All the substituted PIMs-SBF showed higher permeability than the unsubstituted PIM-SBF. The order of permeability of increasing magnitude is: PIM-SBF < PIM-SBF-4 ≈ PIM-SBF-3 < PIM-SBF-5 < PIM-SBF-2 (**Table 1.4**). This is consistent with the results from the molecular simulation and the gas adsorption measurement that both methyl and t-butyl groups result in a moderate to large increase in microporosities. In addition, various substituents can generate different pore size distributions. For example, PIM-SBF-2 with four methyl groups has a greater fraction of

ultramicropores (< 0.7 nm), whereas PIM-SBF-5 with two t-butyl groups has more micropores. Therefore, PIM-SBF-2 (**point 3**) is much more selective than PIM-SBF-5 (**point 4**), leading to an outstanding combination of permeability and selectivity and drives the data point far above the 2008 upper bounds (**Figure 1.22**).

1.6.4.4 Physical aging study of PIMs

Long-term physical aging studies were carried out for PIMs to investigate how aging affect their gas separation performances. Most PIMs shows a graceful aging profile for H_2/N_2 separation where the selectivity gain outweighs the H_2 permeability loss. For example, PIM-1 demonstrates a 46% loss of H_2 permeability but a significant increase of 268% in gas selectivity after 1360 days aging (**point 1', Figure 1.22d**).[29] It means N_2 permeability underwent higher losses relative to H_2. This reflects that larger micropores collapse during aging, which effectively reduces the permeability of large gases more significant than smaller ones and thus improved the size-sieving ability of membranes.

For PIMs-SBF series, the substituted PIMs-SBF exhibited better aging profile relative to unsubstituted PIM-SBF, which is more evident for CO_2/CH_4 (the selectivity gain of substituted PIMs-SBF overweighed the permeability reduction) (**Figure 1.22f**).[152] Surprisingly, the aging process improve the overall gas separation performance for substituted PIMs-SBF. For instance, PIM-SBF-5 displayed a nearly 40% reduction in CO_2 permeability but a nearly 64% increase in CO_2/CH_4 selectivity, pushing its data point up to the 2008 upper bound (**point 4'**, **Figure 1.22f**). For air separation, PIM-SBF-2 shifted from near the 2008 upper bound to a bit below the 2015 upper bound after aging for 1300 days (**point 3'**, **Figure 1.22a**). This indicates the addition of substituents on SBF units contribute to more size-selective ultramicropores formation upon aging. In addition, the aging of PIM-SBF-5 is notably slower than PIM-SBF-2. Over similar aging time of about 1300 days, PIM-SBF-2 (**point 3'**) lost 76% of O_2 permeability, while PIM-SBF-5 (**point 4'**) only lost 32% (**Figure 1.22b**). Notably, within PIMs-SBF series only PIM-SBF-5 maintained higher CO_2 permeability than H_2 after four years aging. These two observations indicate the bulky t-butyl group is more effective in maintaining inter-chain distances during aging than methyl groups.

PIMs with bridged bicyclic structure (PIM-EA-TB, PIM-Trip-TB and PIM-BTrip-TB) showed promising initial gas separation performance and attractive aging trends for H_2/N_2 and air separation which are steeper or parallel to the upper bound (**point 5',6' and 7'**, indicating an improved separation performance, **Figure 1.22b and d**). Overall, PIM-Trip-TB exhibited the best separation performance for H_2/N_2 after aging and even exceeding the PIM-EA-TB (which has better initial separation performance).[149] The outstanding performance of the 100-day-aged PIM-Trip-TB (PH_2 = 4740 Barrer and $\alpha H_2/N_2$ = 25.1) contributed to establishing the 2015 H_2/N_2 upper bound.[27] For CO_2/CH_4, an obviously different aging trend was observed. PIM-EA-TB experienced 63% decrease in permeability but only 19% increase in selectivity, leading to its data point going further below the 2008 upper bound. However, PIM-Trip-TB was seen to give a significant increase of 70% in selectivity with a similar loss in permeability, surpassing the 2008 upper bound after aging.

Notably, TPIM series aged faster and more significantly than other PIMs mentioned here.[29] After 780 days of aging, the H_2 permeabilities of TPIM-1 (**point 8'**) and TPIM-2 (**point 9'**) were decreased by 74% and 65% respectively with a nearly 900% increase in H_2/N_2 selectivities (**Figure 1.22d**). PIM-EA-TB which has higher free volume and a 2-fold higher initial O_2 permeability than TPIM-1, did not exhibit such drastic aging. Only a 43% reduction in H_2 permeability and a 60% gain in selectivity were observed after 470 days aging. This unique aging behaviour of TPIM series is hypothesized to be related to the unique 2D structure of the polymer chains which pack more efficiently in the equilibrium state than 3D polymer chains. The low specific volume at equilibrium (v_∞) is translated into a high driving force for physical aging of 2D ladder polymers according to Struik theory mentioned above, thus leading to a greater aging extent as compared to PIM-EA-TB, PIM-1, etc. For TPIM series, the aging was also found to strongly depend on the substituent groups. As mentioned above, TPIM-1 and TPIM-2 displayed similar changes in gas permeability and selectivity for H_2/N_2 over aging. However, for air separation, TPIM-1 (**point 8'**) with the bulky *isopropyl* substituents acquired a notable increase of 115% for O_2/N_2 selectivity compared to a 55% increase for TPIM-2 (**point 9'**) with linear propyl group, despite a similar loss in O_2 permeability (95% for both) after aging for 780 days (**Figure 1.22b**). This indicates that the branched group can generate more ultramicropores locating between the diameter of O_2 (3.45 Å) and N_2 (3.64 Å) compared to the linear propyl group. After aging, TPIM-1 exhibited extraordinary combination of permeability and selectivity which helped to redefine the 2015

upper bounds for H_2/N_2, H_2/CH_4 and O_2/N_2. The previous observations reflect that the substituents and macromolecular geometry can significantly affect the reorganisation of free volume during aging.

Unlike the TPIM series, PIM-TMN-Trip shows a typical aging behaviour which is similar to most of the PIMs.[141] After 365 days aging, PIM-TMN-Trip (**point 10'**) lost 42% H_2 permeability (from 16900 to 9840 Barrer) but give a 78% increase in H_2/N_2 selectivity, which pushed its data further above the 2008 upper bound (**Figure 1.22c**). For air separation, PIM-TMN-Trip experienced a 58% decrease in O_2 permeability and a 30% increase in O_2/N_2 selectivity after aging, and thus moved up to the 2015 upper bound (**Figure 1.22a**). The ultrapermeable property and promising aging trend of PIM-TMN-Trip motivate us to investigate the potential of the benzotriptycene-based polybenzodioxin polymers in gas separation applications, which will be discussed in detail in Chapter 2.

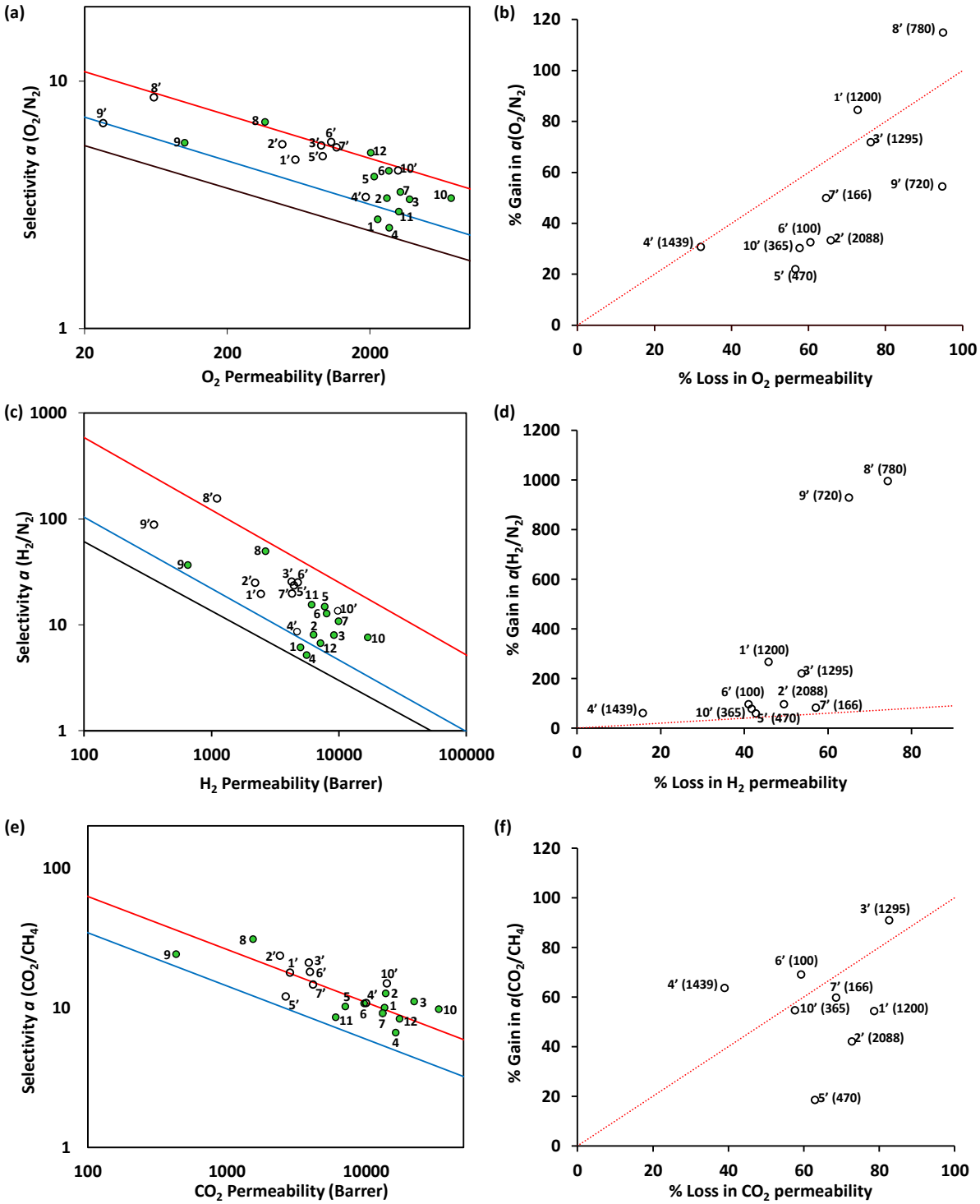

Figure 1.22 Initial and aged gas separation performance of PIMs for (a) O_2/N_2, (c) H_2/N_2 and (f) CO_2/CH_4; Effects of physical aging on gas permeability and selectivity of various PIMs for (b) O_2/N_2, (d) H_2/N_2 and (e) CO_2/CH_4. The number of aging days is shown in parentheses. (1, 1') PIM-1; (2, 2') PIM-SBF; (3, 3') PIM-SBF-2; (4, 4') PIM-SBF-5; (5, 5') PIM-EA-TB; (6, 6') PIM-Trip-TB; (7, 7') PIM-BTrip-TB; (8, 8') TPIM-1; (9, 9') TPIM-2; (10, 10') PIM-TMN-Trip; (11) PIM-TMN-SBI; (12) PIM-TMN-Trip-TB.

1.7 Project aim

According to the previous research summarised above, the gas separation performance of polymers can be tuned via two strategies: (1) introducing functional groups or polar atoms to improve the solubility selectivity of polymers; (2) using new monomers which tune the free-volume elements and free-volume element distribution to improve size-sieving property.

Fluoropolymers display exceptional gas separation performances and helped to redefine the 2008 Roberson upper bounds for light-gas pairs (e.g., N_2/CH_4, He/CH_4, He/N_2 and He/CO_2).[26, 100] This exceptional performance is related to their relatively low solubility for hydrocarbon-vapour (e.g. CH_4) compared to light gases (e.g. N_2).[100] For example, the N_2/CH_4 solubility selectivity of polyimides is about 0.3, reducing the overall N_2/CH_4 selectivity. In contrast, the N_2/CH_4 solubility selectivity for perfluoropolymers is close to 1.[100] Therefore, CF_3 substituent was designed to be incorporated on the benzotriptycene-based polybenzodioxin PIM (PIM-TMN-Trip), which was reported as ultrapermeable as PTMSP (one of the most permeable polymers).[141] The incorporation of CF_3 (PIM-TFM-BTrip) was anticipated to decrease hydrocarbon solubility, so improving the selectivity of benzotriptycene-based PIMs for CO_2/CH_4 and He related gas pairs and also improving the plasticisation resistance.

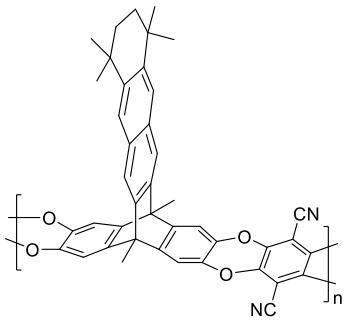

PIM-TMN-Trip

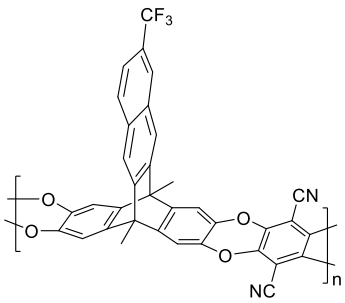

PIM-TFM-BTrip

In the second part, a fluorinated and non-fluorinated benzomethanoanthracene PIMs (PIM-OCF and PIM-OCP) were designed and synthesized in which fluorine atoms was anticipated to have a minor effect on polymer microstructure. This should allow to clearly demonstrate the role of fluorinated substituents in the enhancement of solubility selectivity.

Benzomethanoanthracene with bridged-bicyclic structure was chosen as the building units to ensure high free volume and high diffusivity selectivity.

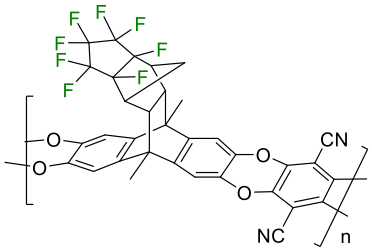

PIM-OCF

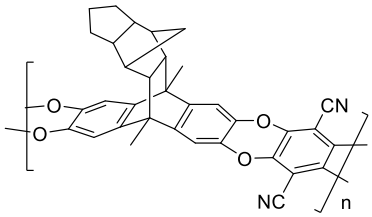

PIM-OCP

The research of benzotriptycene-based PIMs demonstrates that two-dimensional (2D) ladder polymer structure leading to a more finely tuned microporosity relative to its 3D counterpart. Dibenzeno-6,13-methanopentacene (DBMP) has high rigidity and bulkier structure than triptycene. It can be easily prepared by fewer synthetic steps with cheaper starting materials than iptycenes, so DBMP is an attractive motif to create a new 2D PIMs.

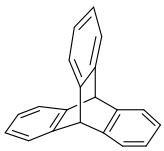

Triptycene

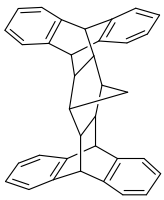

DBMP

The overall aim of the work is to investigate the structure-property relationship so that to guide the design of novel PIMs that can provide outstanding gas separation performance to replace the traditional energy-costly thermal-driven separation.

Chapter 2 Fluorinated benzotriptycene-derived polybenzodioxin polymers for gas separation

2.1 Introduction

Polymeric membrane-based gas separation has become an important and fast-growing separation technology with advantages in cost and energy consumption.[2, 20, 134, 143, 153, 154] It has been used in a wide field of small-scale gas separations, including oxygen or nitrogen enrichment (O_2/N_2), hydrogen recovery during ammonia preparation (H_2/N_2), post-combustion carbon capture (CO_2/N_2) and natural gas upgrading (CO_2/CH_4).[4] However, presently used commercial polymeric membranes are not always competitive with the traditional technologies, such as cryogenic distillation, chemical adsorption and pressure swing adsorption, especially for large scale separations, due to the low gas permeability resulting in low flux or productivity.[61] Therefore, to be compatible with large-scale industrial separations, polymeric membranes are desired to have high permeability in combination with good selectivity. Unfortunately, this is challenging for polymeric membranes because of the trade-off relationship between gas permeability and selectivity (as noted in Chapter 1). For instance, poly(trimethylsilylpropyne) (PTMSP) is known as an ultrapermeable polymer, but its properties do not translate into practical applications because of low selectivity for the transport of one gas over another.[1]

One strategy to overcome this trade-off relationship is to develop polymeric materials that mimic the structure of zeolites or metal-organic frameworks (MOFs) which have high selectivity due to their well-defined pore size and rigidity. Polymers of intrinsic microporosity (PIMs) with highly rigid polymer structures demonstrate great potential to achieve this target.[36] Since being discovered, many PIMs have been developed and shown to demonstrate good gas separation performance and therefore were used to redefine the new upper bounds for a variety of gas pairs in 2008 and later in 2015.[26, 27] Recently, the McKeown group reported a benzotriptycene-based PIM (**Figure 2.1**), showing permeabilities as high as the ultrapermeable PTMSP with improved selectivities, which were contributed by the high rigidity of the benzotriptycene motif with the bridged bicyclic structure.[141] The

benzotriptycene units were fused together with dibenzodioxin linking groups to construct PIMs with discrete 2D macromolecular chains. Importantly, the 2D ribbon shape of benzotriptycene-based PIMs proved to contribute to the ultrapermeability in comparison with its 3D counterpart PIMs.[141] In addition, it was found that the gas transport properties of benzotriptycene-based PIMs can be tuned by introducing various substituents. The bulky aliphatic (e.g. HMI and TMN) substituents can further improve the gas permeability although accompanied with a reduction of gas selectivity due to the increased interchain spacing. The gas transport in the dense membrane depends on solution-diffusion model. In order to achieve a good combination of gas permeability and selectivity, many studies have been conducted to adjust the *diffusivity* selectivity of PIMs by the incorporation of more rigid building blocks[1, 27, 148, 156] far less attention has been made to tune the *solubility* selectivity of PIMs.[43, 157, 158]

Perfluorinated aliphatic polymers have been reported to have exceptional gas separation performances and helped to redefine the 2008 Roberson upper bounds for certain gas pairs, including N_2/CH_4, He/CH_4, $He/N_2$and He/CO_2.[26, 100] The exceptional performance originates from the unique solubility property of fluoropolymers that have low solubility for hydrocarbon-vapours (e.g. CH_4) compared to other light gases (e.g. N_2) because of the carbon-fluorine bonds.[159] Hence, fluorination can be a means of tuning membrane separation performances via solubility selectivity. In this work, two CF_3 substituted benzotriptycene-based PIMs were synthesised and their gas separation performances were investigated.

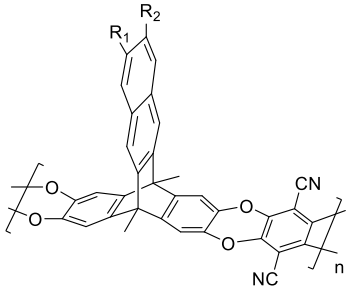

a) PIM-BTrip: $R_1 = R_2 = H$ b) PIM-DM-Trip: $R_1 = R_2 = Me$

c) PIM-TMN-Trip: R_1 and R_2 = 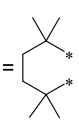 d) PIM-HMI-Trip: R_1 and R_2 = 

Figure 2.1 The structure of benzotriptycene-based PIMs series.

2.2 Synthesis of fluorinated benzotriptycene-based polybenzodioxin polymers

The general synthesis of the substituted benzotriptycene monomers is shown in **Scheme 2.1**. The fluorinated benzotriptycene monomers were prepared by adaptation of the classic benzotriptycene synthesis. In the first step, the fluorinated dienophiles **2** and **3** were generated via the Diels-Alder (DA) reaction between fluorinated chlorobenzenes and furan in the presence of *n*-BuLi at -78 °C. The obtained dienophiles were further reacted with anthracene via a Diels-Alder reaction in a microwave reactor to generate the oxygen-bridged tetramethoxy benzotriptycenes **4** and **5**. Subsequently, the oxygen bridge was removed using methanesulfonic acid at room temperature to give **6** and **7**. The following demethylation of **6** and **7** using BBr_3 afforded the final fluorinated benzotriptycene biscatechols **8** and **9**.

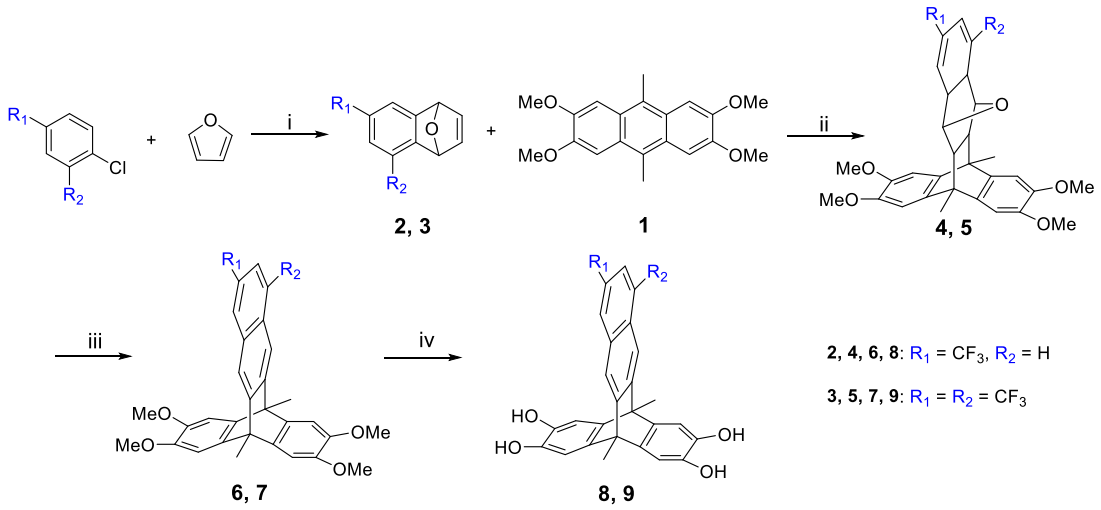

Scheme 2.1 Structure and synthesis route for fluorinated benzotriptycene biscatechols. Reagents and conditions: i. *n*-BuLi, furan, THF, -78 °C, 1.5 h; ii. DMF, 250 °C, 7 bar, 2 h, microwave irradiation; iii. $MeSO_3H$, RT, 24 h; iv. BBr_3, DCM.

The fluorinated dienophiles (**Scheme 2.2**) were prepared according to the procedure reported by Bailly *et al*.[160] Benzyne intermediates were firstly synthesised and subsequently transferred to the 20 equivalents of furan. When transferring the benzyne intermediates, they need to be kept cool due to the rapid decomposition of the benzyne intermediates at room temperature (**Table 2.1**). The yields of these two products were also affected by the

amount of furan. Introduction of higher molar equivalents of furan improved the yield (**Table 2.1**). In addition, removal of molecular oxygen dissolved in furan by degassing gave a higher yield. Low addition rate of the benzyne was needed to avoid side products due to the instability and dimerization of benzyne at room temperature.

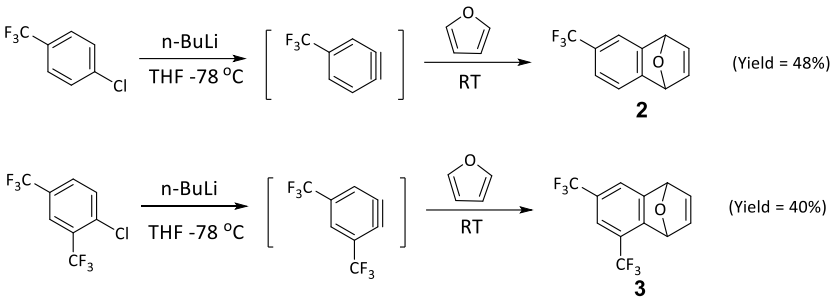

Scheme. 2.2 Synthetic mechanism of fluorinated dienophiles

Table 2.1 Reaction conditions used for the yield optimisation of **2**

Conditions	Equivalent of Furan	Benzyne intermediate kept cooled	Furan Degassed and dried	Yield of 2
Batch 1	10	x	x	/
Batch 2	10	√	x	5.7 %
Batch 3	10	√	√	6.5 %
Batch 4	20	√	√	39.5 %
Batch 5	30	√	√	40.3 %

The demethylation reactions of the fluorinated benzotriptycenes were carried out using boron tribromide (BBr_3) as a Lewis acid.[141] Compound **9** with high purity was achieved in nearly quantitative yield under the general condition involving the use of 3 equivalents of BBr_3 for 3 h. However, there were some impurities generated for biscatechol **8** when using the same conditions (**Figure 2.2a**). Through the optimization of reaction conditions, **8** was obtained in high purity and good yield of 65 % using only 2 equivalents of BBr_3 and reaction for 2 h (**Figure 2.2b**).

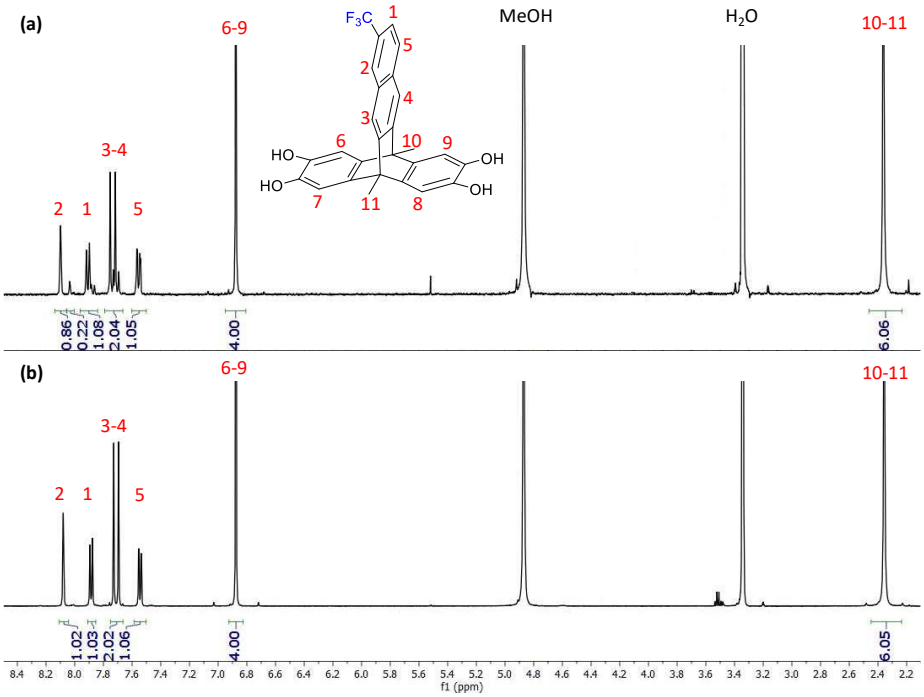

Figure 2.2 The proton NMR spectra for biscatechol **8** using (a) unoptimised and (b) optimised reactions.

With the successfully synthesised fluorinated benzotriptycene biscatechol in hand, polymerisations were carried out using the dibenzodioxin-forming polycondensation with the commercially available 2,3,5,6-tetrafluoroterephthalonitrile (TFTPN) (**Scheme 2.3**) using the optimized conditions developed for the synthesis of PIM-1. Hence, fluorinated benzotriptycene biscatechols and 2,3,5,6-tetrafluoroterephthalonitrile were polymerised in the presence of K_2CO_3 in DMF. This type of step-growth polymerisation is based on a double aromatic nucleophilic substitution which forms two covalent bonds simultaneously. The electron-withdrawing CN substituents in 2,3,5,6-tetrafluoroterephthalonitrile contribute to high reactivity of monomers which improves polymerisation efficiency. In a typical polycondensation reaction, the polymerisation is directly affected by the stoichiometry and the monomer concentrations. High purity of monomers and accurate weight measurements are required to ensure equimolar amounts of monomers, which are needed to obtain high molecular weight polymers. The polymerisation must be carried out under nitrogen and anhydrous conditions as the biscatechols were easily oxidized into quinones. The amount of solvent also plays an important role in polymerisation because high monomer concentrations lead to insoluble crosslinked materials whereas low concentrations result in reduced reaction rates and oligomers. The optimised concentration appears to be different for each monomer and has to be determined by trial and error. For example, the optimal monomer

concentration range for PIM-1 is 3-5 mol/L. The fluorinated benzotriptycene-based polymerisation system forms a thick solid that stops stirring using this monomer concentration. It was found that the optimal concentration for benzotriptycene-based polymers is around 10-13 mol/L. The light-yellow oligomers were usually formed after 15-30 min (depending on the activity of monomers). The reactions were left for 72 h to allow the formation of high molecular weight polymers. These two polymers were found to be only soluble in the high boiling point solvent quinoline, so that the traditional purification process – reprecipitation was avoided due to the difficulties of complete removal of the quinoline. Purification of both polymers was performed by washing with water, acetone and then refluxed in THF twice to afford the polymers with high yields of 79% and 84% for PIM-TFM-BTrip and PIM-DTFM-BTrip, respectively.

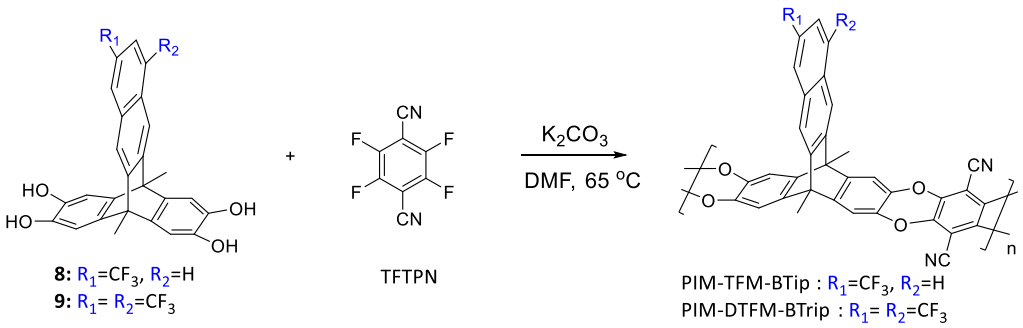

Scheme 2.3 General synthesis of substituted benzotriptycene-based PIMs.

2.3 Physical properties and microporosity analysis

As mentioned previously, PIM-TFM-BTrip and PIM-DTFM-BTrip are only soluble in quinoline (similar to the non-substituted benzotriptycene-PIM (PIM-BTrip)). The poor solubility of PIM-TFM-BTrip and PIM-DTFM-BTrip may be due to the high rigidity of polymer chains and strong intermolecular interactions. Fortunately, they could be cast into mechanically robust free-standing films (**Figure 2.3a**) using quinoline as the solvent (around 3 wt% solution). The obtained films were soaked in methanol for 48 h and dried under vacuum at 40 ˚C for 12 h to remove the residual casting solvent. Thermal gravimetric analysis (TGA) was carried out for PIM-TFM-BTrip and PIM-DTFM-BTrip films. Both of PIM-TFM-BTrip and PIM-DTFM-BTrip exhibited good thermal stability with onset decomposition temperature up to around 500 ˚C in a nitrogen atmosphere (**Figure 2.3b**). There was no obvious weight loss observed before

the decomposition temperature confirming the complete removal of the quinoline casting solvent (**Figure 2.3b**).

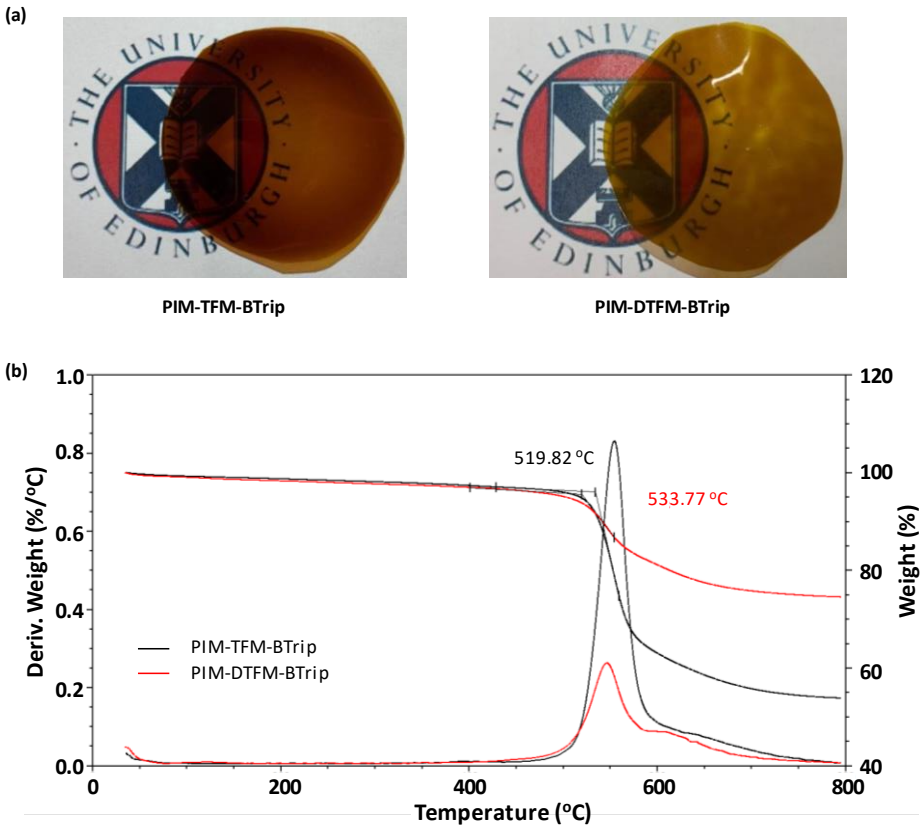

Figure 2.3 (a) Solvent cast free-standing films; (b) Thermogravimetric analysis (TGA) of methanol treated PIM-TFM-BTrip and PIM-DTFM-BTrip films.

Nitrogen adsorption/desorption isotherms for PIM-TFM-BTrip and PIM-DTFM-BTrip powders were measured at 77 K (**Figure 2.4a**). Both polymers show significant nitrogen adsorption at low relative pressures ($P/P_o < 0.01$), confirming their microporous structures. The shape of nitrogen adsorption isotherm for PIM-TFM-BTrip is similar to that of PIM-BTrip, while for PIM-DTFM-BTrip there is a high N_2 adsorption at high relative pressure with a large hysteresis between adsorption and desorption. This may be due to the two CF_3 substituents protruding out of the 2D plane of the polymer chain, leading to a weak cohesion between chains. Brunauer-Emmett-Teller (BET) surface area (SA_{BET}) and total pore volume (V_{Total}) were calculated from nitrogen adsorption isotherms (**Table 2.2**). PIM-TFM-BTrip and PIM-DTFM-BTrip possess high SA_{BET} of 848 and 964 m^2/g, similar to that of PIM-BTrip (911 m^2/g). These values are some of the highest for solution processable polymers. The total pore volumes at

relative pressure P/P_o = 0.98 are 0.66 and 1.02 mL/g for PIM-TFM-BTrip and PIM-DTFM-BTrip, respectively (**Table 2.2**), higher than PIM-BTrip (0.63 mL/g). The results illustrate that CF_3 substituents improve the intrinsic microporosity by increasing the inter-chain distances.

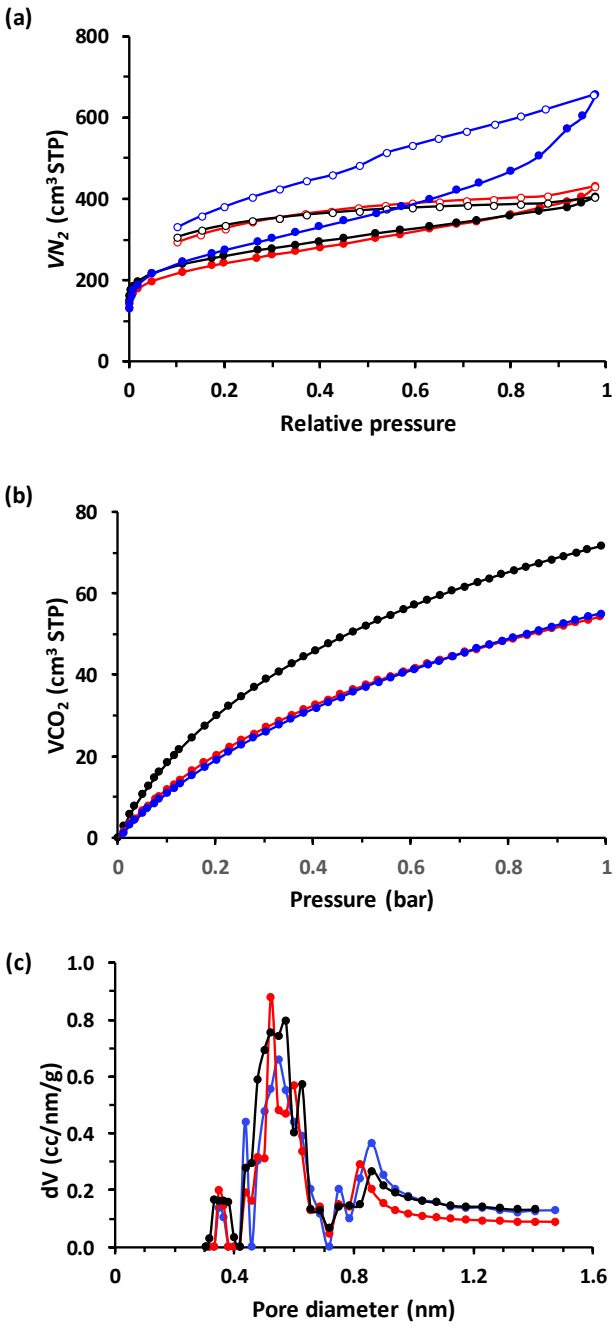

Figure 2.4 (a) Nitrogen adsorption (solid circle) and desorption (open circle) isotherms at 77 K for powdered samples; (b). Carbon dioxide adsorption isotherms at 273 K for powdered samples; (c) Pore size distribution (PSD) calculated from CO_2 adsorption data using non-local density functional theory (NLDFT) model; PIM-BTrip (●), PIM-TFM-BTrip (●), PIM-DTFM-BTrip (●).

Table 2.2 Physical and gas adsorption properties of benzotriptycene-PIMs

Polymer	Solubility	SA_{BET}[a] (m^2/g)	V_{Total}[b] (ml/g)	CO_2 uptake[c] (mmol/g)
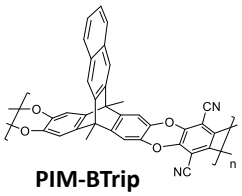 **PIM-BTrip**	Quinoline	911	0.63	3.2
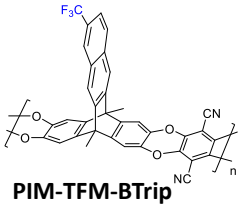 **PIM-TFM-BTrip**	Quinoline	848	0.66	2.5
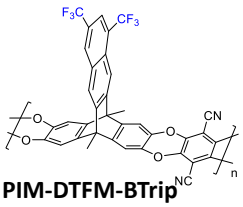 **PIM-DTFM-BTrip**	Quinoline	964	1.02	2.5
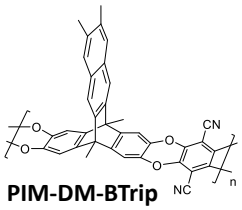 **PIM-DM-BTrip**	Quinoline	920	0.72	3.0
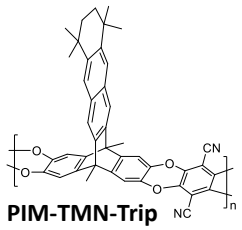 **PIM-TMN-Trip**	Chloroform	1034	0.87	3.3
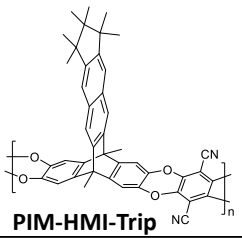 **PIM-HMI-Trip**	Chloroform	1033	0.71	3.0

[a] BET surface area (SA_{BET}) obtained from nitrogen adsorption at 77 k; [b] Total pore volume calculated from nitrogen uptake at P/P_o = 0.98; [c] CO_2 adsorption at 1 bar and 273 K.

PIM-TFM-BTrip and PIM-DTFM-BTrip show lower uptake of CO_2 (2.5 mmol/g) at 1 bar/273 K than PIM-BTrip (3.2 mmol/g) (**Table 2.2**), possibly related to a lower concentration of ultramicropores (diameter < 0.7 nm) than PIM-BTrip. The pore-size distributions (PSDs) were investigated using their CO_2 adsorption isotherms based on non-local density functional theory (NLDFT) model. As shown in PSDs (**Figure 2.4c**), the pores of these benzotriptycene-PIMs are composed of ultramicropores (diameter < 0.7 nm, improving gas selectivity) and larger pore (diameter > 0.7 nm, improving gas permeability). The PSDs confirm that PIM-BTrip has a higher density of ultramicropores, whereas fluorinated PIMs have higher densities of large pores (> 0.7 nm) due to the disruption of chain packing by the CF_3 substituents which leads to larger inter-chain spacing, especially PIM-DTFM-BTrip with two CF_3 substituents.

2.4 Gas transport properties

Single gas permeabilities and ideal gas selectivities of PIM-TFM-BTrip and PIM-DTFM-BTrip films were measured to explore the effects of substituents. The gas permeabilities of polymers are greatly influenced by their film histories and thickness. Methanol treatment was carried out prior to measurement to reverse the effects of physical aging, which allowed the direct comparison of different polymers. All the freshly methanol treated films of benzotriptycene-based PIMs possess exceptionally high gas permeabilities (*e.g., P*co_2 = 21–53 × 10^3 Barrer) (**Table 2.3**), which are comparable to those of ethanol treated ultrapermeable PTMSP (*e.g., P*co_2 = 28–47 × 10^3 Barrer),[114, 161] with selectivities (α_{CO_2/N_2} = 14.2-21.8) that are significantly higher than PTMSP (α_{CO_2/N_2} = 4.0-5.1). The improved performance of benzotriptycene-based PIMs compared to PTMSP stems from the bimodal size distribution of pores generated by the inefficient packing of 2D polymer chains, while PTMSP contains a higher density of large pores.[156] The gas permeabilities of both freshly methanol treated PIM-TFM-BTrip and PIM-DTFM-BTrip films showed the following order: $CO_2 > H_2 > O_2 >$ He > $CH_4 > N_2$, the same as that for other substituted benzotriptycene-PIMs, except for PIM-BTrip (He permeability is higher than O_2). This is due to the higher density of ultramicropores in the PIM-BTrip film accounting for the performance as a molecular sieve which favours the transport of small He molecules.

Table 2.3 Thickness (*L*, μm), ideal gas permeabilities (P_X, Barrer) and selectivities ($\alpha_{X/Y}$) of freshly methanol treated and aged films measured at 25 ˚C and 1 bar of feed pressure.

PIM-	*L* (μm)[a]	P_{N_2}	P_{O_2}	P_{CO_2}	P_{CH_4}	P_{H_2}	P_{He}	α_{O_2/N_2}	α_{H_2/N_2}	α_{CO_2/N_2}	α_{CO_2/CH_4}
BTrip	160	1190	4330	21500	1690	12100	4540	3.64	10.2	18.1	12.7
(490)[b,c,d]	160	195	1240	6060	203	6380	2650	6.34	32.6	31.0	29.9
TFM-Btrip[c,d]	176	1830	6210	33700	2280	13600	5150	3.39	7.43	18.4	14.8
(496)[b]	176	722	3260	15600	792	9760	3920	4.51	13.5	21.6	19.7
DTFM-BTrip	112	3000	7770	42600	4340	14700	5860	2.59	4.90	14.2	9.82
(490)	112	864	3490	16900	890	10400	4770	4.04	12.1	19.6	19.0
DM-BTrip[d]	114	1020	3950	22000	1570	11400	4000	3.90	11.3	21.8	14.0
(128)[d]	114	521	2640	12200	599	9870	3650	5.07	18.9	23.4	20.4
TMN-Trip	166	3540	10400	52800	7250	18800	6490	2.94	5.31	14.9	7.28
(426)	166	1100	4620	20400	1440	14100	5420	4.20	12.8	18.5	14.2
HMI-Trip[d]	135	2560	8540	44200	4870	16600	5700	3.34	6.48	17.3	9.08
(426)	135	804	3580	16400	967	11000	4150	4.45	13.7	20.4	16.9

[a] Thickness did not exhibit significant change upon ageing; [b] Number in parentheses is the ageing time in days after methanol treatment; [c] The data used to define the proposed CO_2/N_2 upper bound; [d] The data used to define the proposed CO_2/CH_4 upper bound.

Comparing data from approximately like-for-like samples, PIM-TFM-BTrip (176 μm) has higher gas permeabilities than PIM-BTrip (160 μm) for all gases. Even the thinner PIM-DTFM-BTrip (112 μm) possesses higher gas permeabilities than PIM-BTrip (160 μm) Typically, thinner films have a lower gas permeability due to the fast physical-ageing rate. As noted in Chapter 1, the gas permeability in the dense polymer films depends on the gas diffusivity coefficient (*D*) and solubility coefficient (*S*) which can be obtained from the permeability measurements. Therefore, the ideal selectivity ($\alpha_{X/Y}$) can be expressed as the product of the diffusivity selectivity (D_X/D_Y) and solubility selectivity (S_X/S_Y). For comparison, the gas transport data of benzotriptycene-based PIMs have been listed **in Table 2.3, 2.4 and 2.5**. As can be seen, the higher permeabilities of CF_3 substituted benzotriptycene-PIMs compared to PIM-BTrip result from the higher diffusivity coefficients because of the higher free volume induced by the CF_3 substituents (**Table 2.4**).

The diffusivity selectivity appears reduced due to the larger inter-chain spacing induced by the CF_3 substituent. The molecular sieving effect is well illustrated by the correlation between the square of the effective gas diameter (d^2_{eff}) and the diffusivity coefficient (D_X) (**Figure 2.5**), where the slope represents the diffusivity selectivity. It is clear that the diffusivity selectivity of PIM-BTrip is exceptionally high. In contrast, the solubility selectivity is enhanced by CF_3 addition, although the solubility coefficients decrease. The decreased solubility coefficients may be due to the reduced number of gas adsorption sites, so that PIM-TFM-BTrip has lower CO_2 adsorption than PIM-BTrip (as shown in **Figure 2.4b**). The solubility selectivity showed a significant increase for CO_2/CH_4 (3 times as compared to 2 times for O_2/N_2, H_2/N_2 and CO_2/N_2) (**Table 2.5**). This phenomenon may be related to the unique hydrocarbon-phobic property of fluoropolymers, leading to the larger reduction of absorption sites for CH_4 in comparison to CO_2. Consequently, the gas selectivities of O_2/N_2 and H_2/N_2 dominated by the diffusivity selectivity exhibit a reduction with CF_3 substitution (**Figure 2.6a and Table 2.4**), while for CO_2/N_2 the selectivity shows little variation as a result of the increased solubility selectivity offsetting the decrease of diffusivity selectivity with CF_3 substitution (**Figure 2.6a**). Surprisingly, considering the well-defined trade-off relationship, the CO_2/CH_4 gas selectivity of PIM-TFM-BTrip increases slightly with increased CO_2 permeability (**Figure 2.6a**). This result suggests that PIM-TFM-BTrip has better overall gas separation performance for CO_2/CH_4, even though it is not as effective at size-sieving as PIM-BTrip.

Table 2.4 Thickness (*L,* μm), diffusivity coefficients (D_X, 10^{-12} m^2 /s) and diffusivity selectivities (D_X/D_Y) of freshly methanol treated films measured at 25 ˚C and 1 bar of feed pressure.

PIM-	*L* (μm)	D_{N_2}	D_{O_2}	D_{CO_2}	D_{CH_4}	D_{H_2}	D_{He}	D_{O_2/N_2}	D_{H_2/N_2}	D_{CO_2/N_2}	D_{CO_2/CH_4}
BTrip	160	100	422	172	36.1	7660	9300	4.22	76.6	1.72	4.76
TFM-BTrip	176	542	1130	464	264	13800	16700	2.08	25.5	0.86	1.76
DTFM-BTrip	112	375	1110	430	165	10300	11100	2.96	27.5	1.15	2.61
DM-BTrip	114	182	608	242	65.9	8930	10300	3.34	49.0	1.33	3.65
TMN-Trip	166	803	1700	641	413	15900	20600	2.12	19.8	0.80	1.55
HMI-Trip	135	550	1360	496	286	12500	14000	2.47	22.7	0.90	1.73

Table 2.5 Thickness (*L*, µm), solubility coefficient (S_X, cm^3_{STP} cm^{-3} bar^{-1}) and solubility selectivity (S_X/S_Y) of freshly methanol treated films measured at 25 ˚C and 1 bar of feed pressure.

PIM-	*L* (µm)	S_{N_2}	S_{O_2}	S_{CO_2}	S_{CH_4}	S_{H_2}	S_{He}	S_{O_2/N_2}	S_{H_2/N_2}	S_{CO_2/N_2}	S_{CO_2/CH_4}
BTrip	160	8.85	7.69	94.1	35.2	1.18	0.37	0.87	0.13	10.6	2.67
TFM-BTrip	176	2.53	4.11	54.4	6.47	0.74	0.23	1.62	0.29	21.5	8.41
DTFM-BTrip	112	6.00	5.26	74.3	19.7	1.07	0.40	0.88	0.18	12.4	3.77
DM-BTrip	114	4.37	5.20	73.1	17.1	0.94	0.28	1.19	0.21	16.7	4.27
TMN-Trip	166	3.31	4.60	61.8	13.2	0.89	0.24	1.39	0.27	18.7	4.68
HMI-Trip	135	3.50	4.70	66.7	12.8	1.00	0.31	1.34	0.29	19.1	5.21

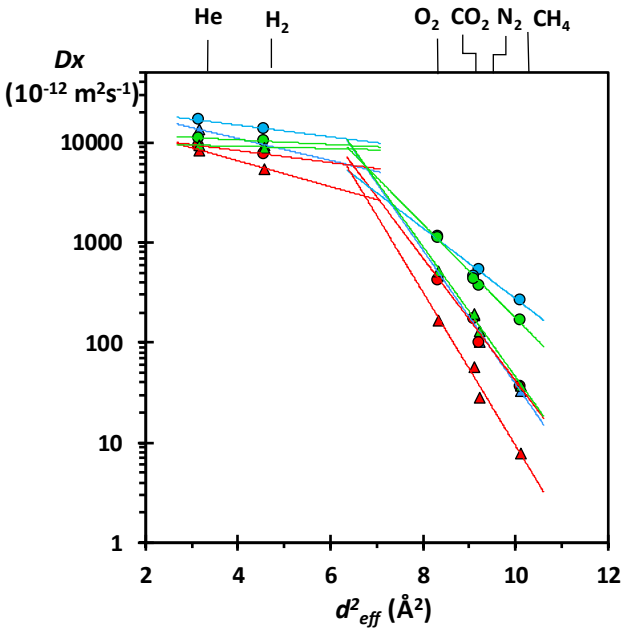

Figure 2.5 Correlation of diffusivity coefficient (D_x) with the squared effective gas diameter (d^2_{eff}) (d_{eff} = effective diameter of gas molecule : He = 1.78; H_2 = 2.14; O_2 = 2.89; CO_2 = 3.02; N_2 = 3.04; CH_4 = 3.18 Å) for fresh (circle) and one year aged (triangle) films of PIM-BTrip (● ▲), PIM-TFM-BTrip (● ▲) and PIM-DTFM-BTrip (● ▲).

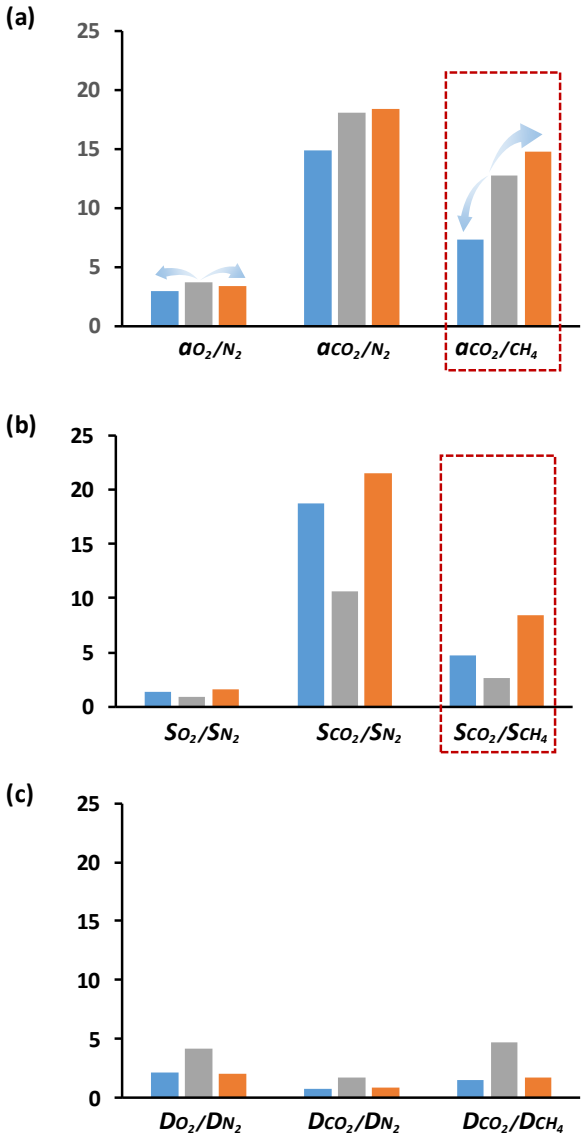

Figure 2.6 (a) The gas selectivity $\alpha_{X/Y}$; (b) the gas solubility selectivity S_X/S_Y; (c) the diffusivity selectivity D_X/D_Y for O_2/N_2, CO_2/N_2 and CO_2/CH_4 from the fresh methanol treated PIM-BTrip (160 µm, ■), PIM-TMN-Trip (166 µm, ■) and PIM-TFM-BTrip (176 µm, ■).

In contrast, the gas solubility selectivities of PIM-TMN-Trip (with an aliphatic substituent, 166 µm) increased by similar extent for all gas pairs relative to PIM-BTrip, which is less significant than the decrease of diffusivity selectivity. Therefore, PIM-TMN-Trip exhibits an increase in gas permeabilities coupled with a reduction in gas selectivities for all gas pairs compared with PIM-BTrip (**Table 2.3**), following the trade-off relationship between gas permeability and selectivity. PIM-TFM-BTrip (176 µm) possesses lower gas permeability, but higher gas selectivity in comparison with PIM-TMN-Trip which has a relatively large

size substituent. It is found that the gas selectivity of CO_2/CH_4 was increased significantly (103 %) when the TMN substituent was changed to CF_3 groups, while only 15-40 % increases in gas selectivities were observed for other gas pairs (**Figure 2.6a**). The **Figure 2.6b** demonstrates the significant increase in CO_2/CH_4 selectivity mainly derives from the remarkable enhancement of S_{CO_2}/S_{CH_4} (80 %), whereas the S_X/S_Y for other gas pairs showed only 7-17 % increase. This may also be attributed to the low hydrocarbon solubility in fluoropolymers evidenced by the far larger reduction of S_{CH_4} (51 %) in comparison to other gases (10 %-20 %) (**Table 2.5**).

PIM-DTFM-BTrip possesses the highest permeability among all benzotriptycene-PIMs due to the high gas diffusivity, but low gas selectivity for all gas pairs. It reflects that the two CF_3 substituents disrupt the polymer chains packing and increase the intra-chain spacing efficiently compared with other substituted PIMs. It is consistent with the N_2 adsorption data that PIM-DTFM-BTrip shows a unique high uptake of N_2 at relative high pressure demonstrating the high content of larger pores.

As noted above, there is a significant variability of gas permeability from differing film thicknesses and histories. The direct way to evaluate and compare gas separation performance of different polymers is to place their permeability data on a Robeson plot. As mentioned in Chapter 1, the Robeson upper bounds represent the state of the art polymer films for the gas separations. The position of the data of a new polymer relative to the Roberson upper bounds is used as a performance indicator. As shown in **Figure 2.7**, significant improvements in permeability-selectivity combinations are observed for benzotriptycene-based PIMs, with all gas permeability data points exceeding the 2008 upper bounds for all gas pairs. For O_2/N_2 and H_2/N_2, PIM-BTrip is close to the 2015 upper bounds due to its good size-sieving property relative to substituted benzotriptycene-based PIMs.

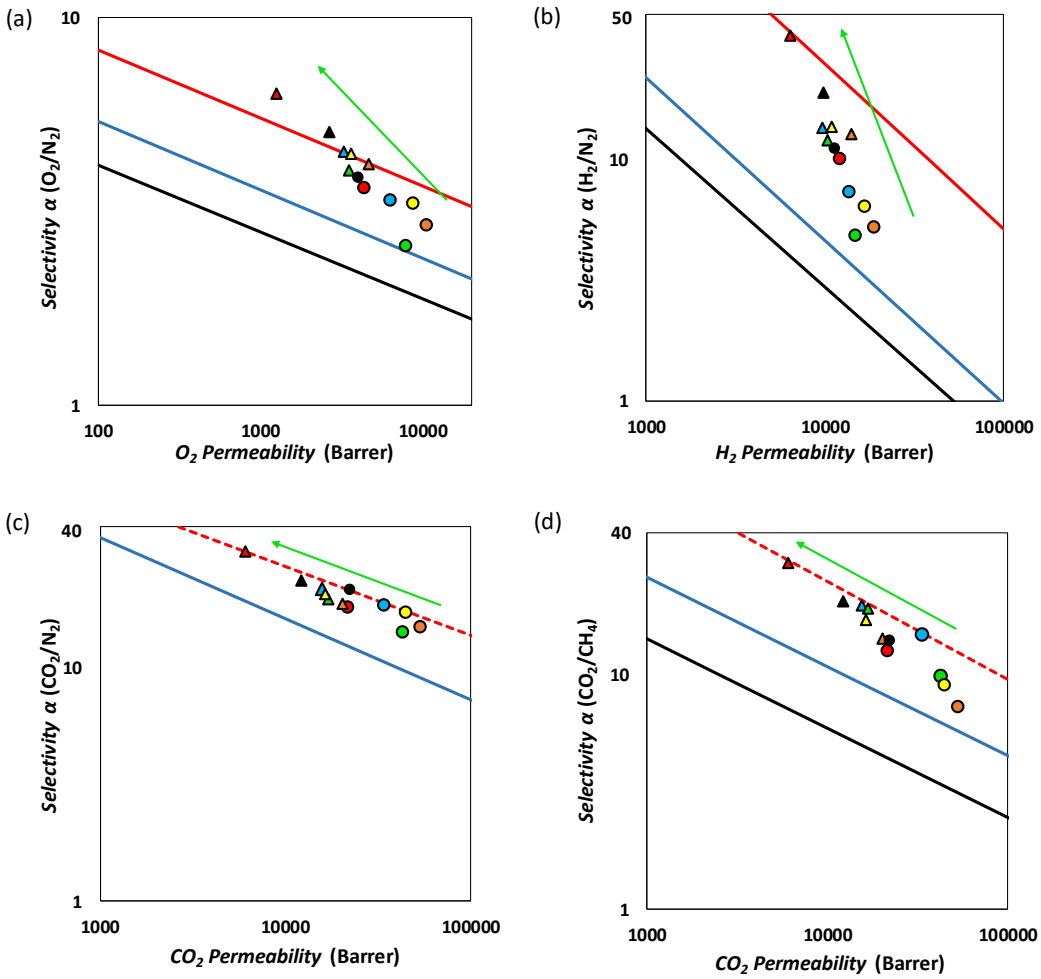

Figure 2.7 Robeson plots for the (a) O_2/N_2, (b) H_2/N_2, (c) CO_2/N_2 and (d) CO_2/CH_4 gas pairs showing the position of the fresh (circle) and aged (triangle) films of PIM-BTrip (● ▲), PIM-TMN-Trip (● ▲), PIM-HMI-Trip (● ▲), PIM-DM-BTrip (● ▲), PIM-TFM-BTrip (● ▲) and PIM-DTFM-BTrip (● ▲). The black and blue lines represent the 1991 and 2008 upper bounds, and the red solid lines are the proposed 2015 upper bound for O_2/N_2 and H_2/N_2. The proposed revised upper bounds for CO_2/N_2 and CO_2/CH_4 are shown as dotted red lines. The green arrows show the ageing trend-lines.

For CO_2 involving gas pairs, the separation mechanism is more complicated, as S_{CO_2} governs the transport, especially for CO_2/N_2 because the two gas molecules have similar effective diameters. Generally, the diffusivity selectivity of CO_2/N_2 for PIMs is around 1 because of the small diameter differences, whereas the solubility selectivity lies in the range 15-20. **Figure 2.7c** shows that all the data points of benzotriptycene-based PIMs lie far above the 2008 CO_2/N_2 upper bound. The impressive performance of PIM-BTrip is attributed to the high value of D_{CO_2}/D_{N_2} (around 2), whereas for PIM-TFM-BTrip it is due to the greater value of S_{CO_2}/S_{N_2} (~21.5) (**Table 2.5**). The data points of PIM-BTrip, PIM-TFM-

BTrip, PIM-HMI-Trip and PIM-DM-BTrip are in a good linear correlation and significantly above the 2008 upper bound. This allows us to propose a new upper bound representing the new state of the art of polymeric films for CO_2/N_2 gas separation (**Figure 2.7c**).[155] In addition, the benzotriptycene-based PIMs show good separation performance toward CO_2/CH_4 for which the data lie well above the 2008 upper bound. The data for PIM-BTrip and PIM-TFM-BTrip yield a new upper bound with a selectivity 2.5 times higher than that for the 2008 upper bound (**Figure 2.7d**).

Physical aging is a typical phenomenon for glassy polymers, in which the polymer develops a more tightly packed state leading to the reduction of gas permeability but a corresponding increase of gas selectivity. Ageing studies were carried out on the films of the benzotriptycene-based PIMs using the same measurement conditions as for the freshly methanol treated films. For O_2/N_2 and H_2/N_2 gas pairs, the trend lines of ageing data are steeper in gradient than the Roberson upper bounds (green lines in **Figure 2.7a and b**). This reflects that physical ageing causes the preferential collapse of large micropores leading to the larger reduction of permeabilities of larger molecules (N_2 and CH_4) as compared to smaller gases (H_2 and O_2). Therefore, the size-sieving behaviours for all benzotriptycene-based PIMs were enhanced after ageing, as illustrated by the correlation between the square of the effective gas diameter (d^2_{eff}) and the diffusivity coefficient (D_X), of which the slope is steeper after ageing (**Figure.2.5**). Notably, the data point for PIM-BTrip after one year ageing (P_{O_2} = 1240 Barrer; P_{O_2}/P_{N_2} = 6.3) lies far beyond the 2015 upper bounds for O_2/N_2, and for PIM-TFM-BTrip the ageing data point locates on the 2015 O_2/N_2 upper bounds. Therefore, the aged films of PIM-BTrip and PIM-TFM-BTrip demonstrate further enhancement in O_2/N_2 and H_2/N_2 gas separation.

In contrast, the trend lines of ageing data for CO_2/N_2 and CO_2/CH_4 are relatively shallow and approximately parallel to the upper bounds. This is due to the gas selectivity of these two gas pairs largely contributed by solubility selectivity which were not significantly changed over ageing. PIM-BTrip exhibits impressive separation performance after one-year aging (P_{CO_2} = 6060 Barrer; α_{CO_2/N_2} = 31). Indeed, few such highly permeable polymers possess a CO_2/N_2 selectivity > 30,[40, 43, 162, 163] which is the lower limit of interest for a first-pass polymer membrane for post-combustion carbon capture.[164]

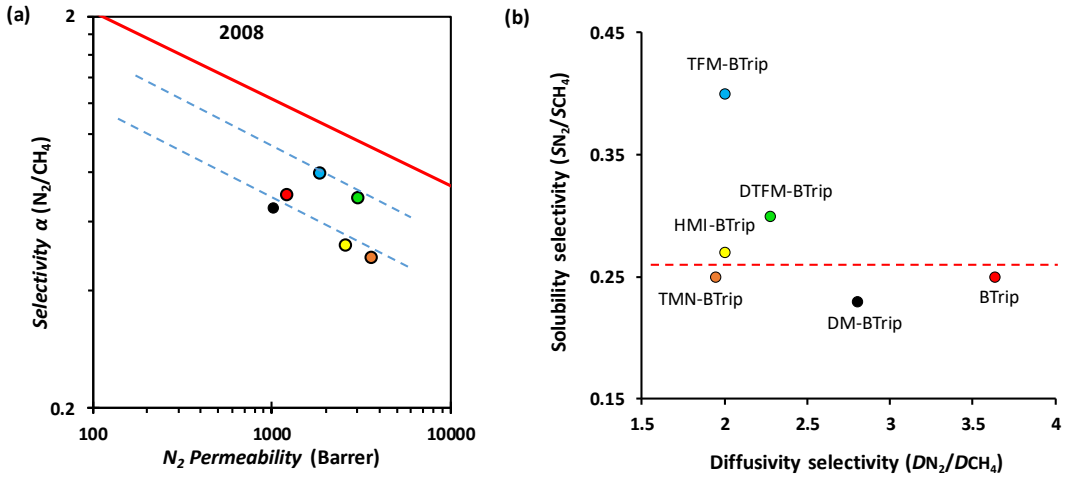

Figure 2.8 (a) Robeson plots for N_2/CH_4 showing the data of the fresh films of PIM-BTrip ( ), PIM-TMN-Trip ( ), PIM-HMI-Trip ( ), PIM-DM-BTrip ( ), PIM-TFM-BTrip ( ) and PIM-DTFM-BTrip ( ). The red solid line represents the 2008 upper bound; (b) N_2/CH_4 solubility selectivities versus diffusivity selectivities for benzotriptycene-based PIMs.

For the N_2/CH_4 gas pair, the gas permeability data of all benzotriptycene-PIMs lie blow the upper bound (**Figure 2.8a**). It is notable that the benzotriptycene-based PIMs are divided into two classes according to the distance of the gas permeability data relative to the upper bound. Data for the fluorinated PIMs lie closer to the 2008 upper bound than that of the aliphatic substituted PIMs or unsubsituted PIM-BTrip due to higher gas selectivity. An analysis of the individual effects of solubility and diffusivity selectivity on N_2/CH_4 selectivity can provide an insight on why fluorinated PIMs exhibit better N_2/CH_4 selectivity as compared to aliphatic substituted PIMs. **Figure 2.8b** shows N_2/CH_4 diffusivity selectivity versus solubility selectivity. The diffusivity selectivities for all benzotriptycene-based PIMs are higher than 1 due to the smaller diameter of N_2 than CH_4 (**Figure 2.8b**). PIM-BTrip possesses the highest diffusivity selectivity because of its strongest size sieving performance, and as expected, the diffusivity selectivity decreased with increasing the size of substituents (**Figure 2.8b**). The solubility selectivties for all benzotriptycene-based PIMs are less than 1 due to CH_4 more condensable than N_2, so the solubility selectivity acts to reduce the overall N_2/CH_4 selectivity. It is of interest to observe that the solubility selectivity of PIM-TFM-BTrip (~0.4) and PIM-DTFM-BTrip (~0.3) are higher than for the other benzotriptycene-based PIMs (around 0.26). Therefore, fluorinated benzotriptycene PIMs have higher overall N_2/CH_4 selectivity. This behaviour is consistent with perfluoropolymers which set the position of the 2008 upper bound for N_2/CH_4 due to their

high solubility selectivity ($S_{N_2}/S_{CH_4} \rightarrow 1$).[26, 100] The unique solubility selectivity of N_2/CH_4 is related to the relatively high light-gas solubility (e.g., N_2) but low hydrocarbon solubility (e.g., CH_4) in perfluoropolymers.[159] The promising result of fluorinated benzotriptycene PIMs encourage us to design and synthesize new PIMs with more fluorines to improve the gas separation performance of polymeric membranes as described in Chapter 3.

Overall, the benzotriptycene-based PIMs exhibit ultrahigh permeabilities with high selectivities due to the inefficient packing of their 2D ladder-like macromolecular strucutres. The substituents on the benzotriptycene were observed to have a profound effect on their gas separation performance. The bulky substituents (TMN and HMI) leaded to an increase in permeability with a loss in selectivity, obeying the trade-off relationship. However, the CF_3 group improved the gas selectivity of CO_2/CH_4 and N_2/CH_4 for PIM-TFM-BTrip due to the notably enhanced solubility selectivity, although this group degraded its size-sieving property.

Chapter 3 Fluorinated benzomethanoanthracene based polymers

3.1 Introduction

Pervious work in the McKeown group has shown that ladder polymers built using benzomethanoanthracene units displayed high surface areas. Benzomethanoanthracene contains a rigid bridged-bicyclic structure where a norbornene unit is connected to the anthracene (**Figure 3.1**) using a Diels-Alder (DA) reaction under mild conditions. In comparison, the synthesis of triptycene which has a similar bridged-bicyclic structure to benzomethanoanthracene requires the formation of highly reactive benzyne intermediates. Therefore, ladder polymers based on benzomethanoanthracene can be synthesized more easily than triptycene based PIMs, and possess high free volume and rigidity. In addition, norbornene has been used as a monomer for ring-opening metathesis polymerisations for a long time, therefore there are many norbornenes with various substituents at the *a* or *b* positions, such as carboxyl group,[165] trimethylsilyl group,[166] halogens,[167] nitriles[168]. The variety of substituted norbornenes provides the benzomethanoanthracene unit with many possible functionalities to tune the structures and properties of the resulting polymers.

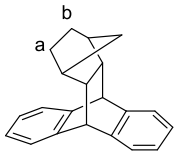

Figure 3.1 The molecule structure of benzomethanoanthracene.

3.2 Octafluorocyclopentyl benzomethanoanthracene based polybenzodioxin polymers

Based on the results presented above, it appears that the introduction of fluorocarbon units to PIMs should result in enhanced performance, particularly for the commercially important CO_2/CH_4 gas pair, which is of relevance to natural gas and biogas purification. However, it is a very difficult challenge to demonstrate that any observed improvement results from

increased solubility selectivity (i.e. S_{CO_2}/S_{CH_4}) originating from lower S_{CH_4} that is due exclusively to the inclusion of the fluorocarbon unit. This is because the fluorocarbon unit may have a profound effect on the conformation and rigidity of the polymer chain, thereby changing packing within the polymer film and the size distribution of free volume elements. Therefore, for most polymers the simple substitution of a hydrocarbon unit for a fluorocarbon unit may result in complex, interrelated differences to gas transport properties with consequences for both D_X/D_Y and S_X/S_Y, which are difficult to distinguish. In an attempt to enhance CO_2/CH_4 solubility selectivity and to demonstrate the utility of fluorinated substituents, an increase in concentration of fluorine atoms within 2D PIMs was considered. This section describes the design, synthesis and performance of two PIMs (PIM-OCF and PIM-OCP **Figure 3.1**) with structures that should allow the role of fluorinated substituents in the enhancement of solubility selectivity to be established. Design features include: (i) a rigid bridged-bicyclic structure to ensure high diffusivity selectivity, similar to that of PIMs, which were used to define the recently modified upper bounds (above); (ii) a conformationally-locked cyclic substituent in either a fluorinated or non-fluorinated form, which would be expected to have no effect on chain conformation or rigidity.

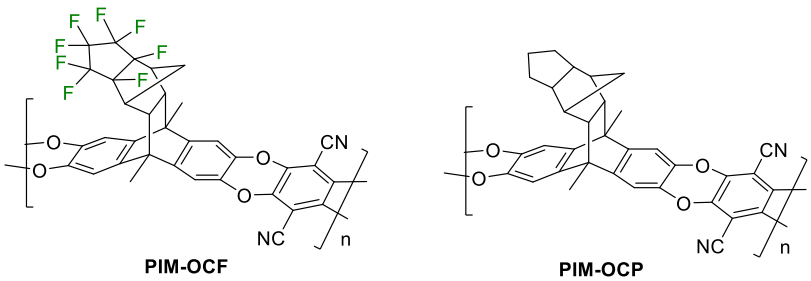

Figure 3.1 Polymer structures of PIM-OCF and PIM-OCP

3.2.1 Synthesis of octafluorocyclopentyl benzomethanoanthracene based polybenzodioxin polymers

The first step in the synthesis of PIM-OCF and PIM-OCP, via the desired monomers **14** and **15**, was to prepare the required substituted norbornenes **10a** and **11** via the Diels-Alder (DA) reaction (**Scheme 3.1**). The DA reaction between octafluoropentene (**OCF**, 1.3 eq.) and cyclopentadiene (**CPD**, 1 eq.) (obtained by dicyclopentadiene cracking) was performed at 150 °C according to a reported method.[169] The desired product **10a** was achieved in a yield

of 30% as a mixture of endo/exo-isomers. In this DA reaction, a side product **10b** fused with one more cyclopentadiene was also formed in a 19% yield. Interestingly, the required DA adduct product **12** was afforded in a yield of about 40 % using either **10a** or **10b** as the dienophile in the DA reaction with 2,3,6,7-tetramethoxy-9,10-dimethylanthracene under microwave irradiation at 250 °C, so that separation of **10a** and **10b** proved unnecessary. The required dienophile **11** was prepared using a slightly modified method reported by Hong *et al* (**Scheme 3.2**).[170] This reaction was performed at 200 °C which was higher than the cracking temperature of dicyclopentadiene (**DCPD**). Therefore, **DCPD** (1 eq.) in this method was used directly in the DA reaction with an excess of commercially available material cyclopentene (**COP**, 7 eq.) to afford **11** in a 39% yield as a mixture of endo/exo-isomers. Compound **11** underwent a DA reaction with 2,3,6,7-tetramethoxy-9,10-dimethylanthracene under microwave irradiation at 250 °C for 2 h to generate the expected product **13a** in a 18% yield, together with the unexpected product **13b**, presumably derived from the retro-Diels-Alder reaction of **11**, in a 30% yield. The extension of reaction time to 4 h failed to improve the yield of **13a**. A lower reaction temperature of 230 °C was then used for this DA reaction, but only **13b** was formed in a 27% yield. This implies that the DA reaction product **11** "cracks" at 230 °C and cyclopentene is more reactive than **11** in the DA reaction with 2,3,6,7-tetramethoxy-9,10-dimethylanthracene.

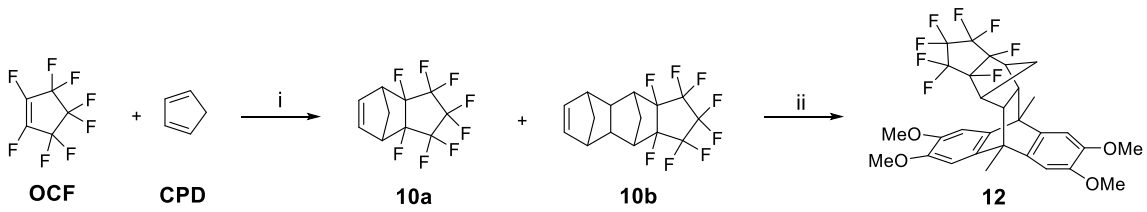

Scheme 3.1 Synthesis route for octafluorocyclopentyl tetramethoxybenzomethanoanthracene **12**. Reagents and conditions: i 150 ˚C, 72 h, high pressure reactor; ii 2,3,6,7-Tetramethoxy-9,10-dimethylanthracene, DMF, 250 °C, 7 bar, 2 h, microwave irradiation.

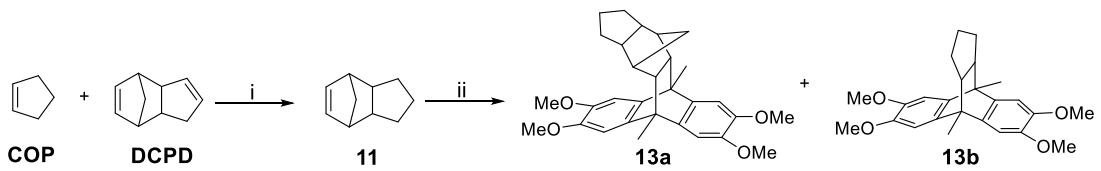

Scheme 3.2 Synthesis route for cyclopentyl tetramethoxybenzomethanoanthracene **13a**. Reagents and conditions: i 200 ˚C, 15 h, high pressure reactor; ii 2,3,6,7-Tetramethoxy-9,10-dimethylanthracene, DMF, 250 °C, 7 bar, 2 h, microwave irradiation.

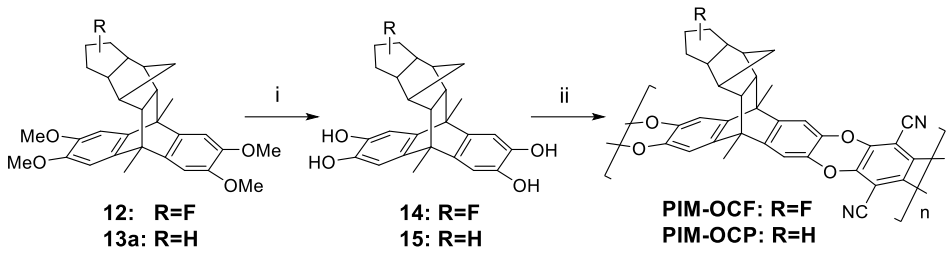

Scheme 3.3 Synthesis route for polymers. Reagents and conditions: i BBr_3, anhydrous DCM, RT; ii Tetrafluoroterephthalonitrile (TFTPN), K_2CO_3, DMF, 65 ˚C, 72 h.

After demethylation of compounds **12** and **13** using boron tribromide, the biscatechol monomers **14** and **15** were achieved in over 80% yield (**Scheme 3.3**). As shown in the NMR spectra (**Figure 3.2**), one of the hydrogens on the methano-bridge carbons of **14** and **15** is found at a low chemical shift which is close to (for **14**) or below (for **15**) 0 ppm, suggesting that this hydrogen is inserted into the adjacent benzene ring which has a strong deshielding effect on it. This structural feature may improve the rigidity of the molecules and therefore may contribute to an improved rigidity of the resulting polymer chains. In addition, it was observed that the DA adduct **13a** was a mixture of isomers while **12** was synthesised as a single product. This is probably due to a higher steric hindrance of the fluorines. These monomers were polymerised with the commercially available tetrafluoroterephthalonitrile (TFTPN) using the standard reaction condition for polybenzodioxin PIMs to form the desired polymers (PIM-OCF and PIM-OCP) (**Scheme 3.3**). PIM-OCF and PIM-OCP possess good solubilities in THF and 1,1,2,2-tetrachloroethane (TCE), respectively. As compared with the benzotriptycene-based PIMs, the replacement of fused aromatic rings with the cycloalkyl fused rings improved polymer solubility. Optically clear and robust films were then achieved by casting these polymer solutions (**Figure 3.3**)

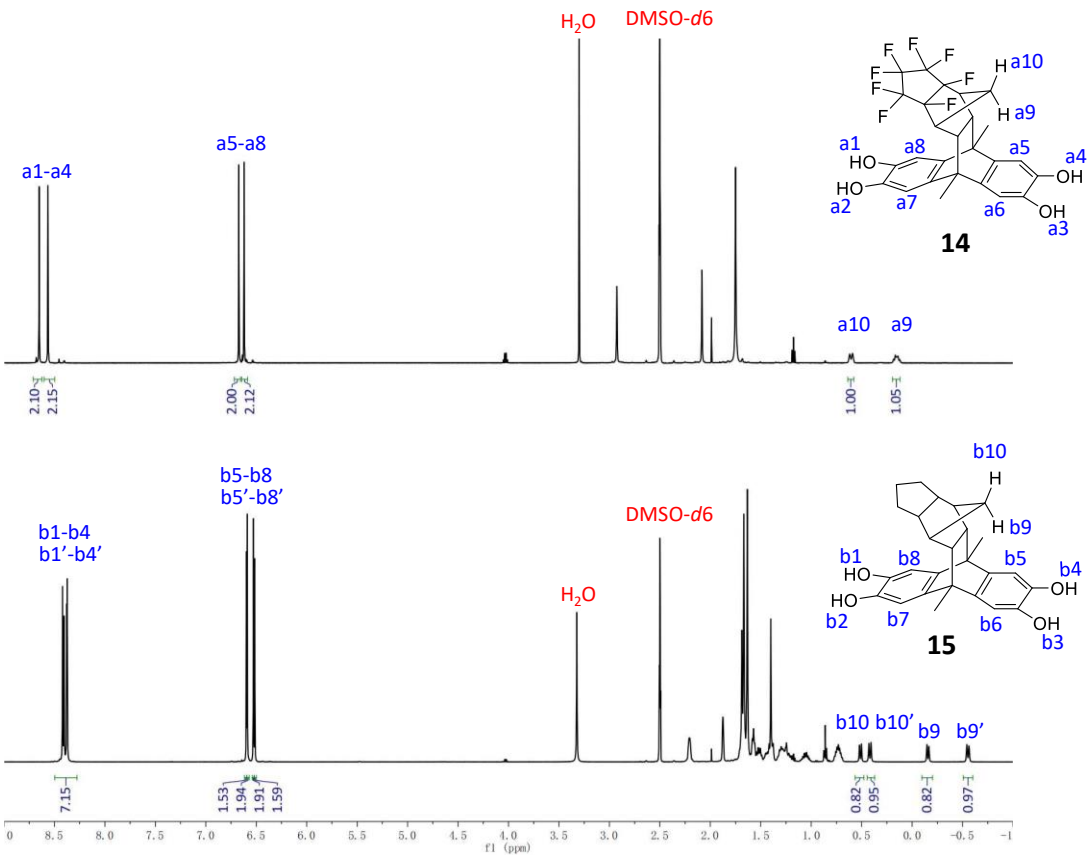

Figure 3.2 NMR spectra for biscatechols **14** and **15** (bn and bn' represent the regioisomers).

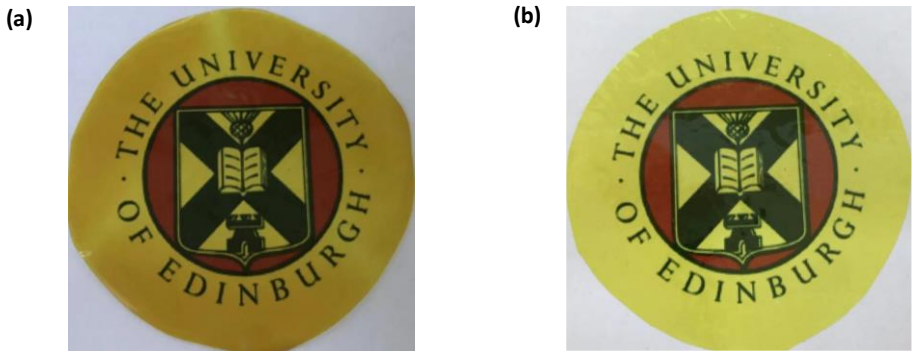

PIM-OCF PIM-OCP

Figure 3.3 The film photos of PIM-OCF and PIM-OCP.

3.2.2 Microporous analysis

The microporous structures of PIM-OCP and PIM-OCF were analysed using gas adsorption and molecular modelling analysis of chain-packing performed by the research group of Prof.

Coray Colina at the University of Florida. The N_2 adsorption/desorption isotherms were measured using PIM-OCP and PIM-OCF powder at 77 K. Significant N_2 uptakes at low relative pressure was observed for both of their N_2 adsorption isotherms, suggesting the presence of the accessible microporosities (**Figure 3.4a**). As calculated from the N_2 adsorption isotherms, PIM-OCP and PIM-OCF possess high BET surface areas of 1062 and 928 m^2/g, respectively, which are higher than the surface areas of 802 and 625 m^2/g obtained from the molecular modelling, presumably due to the polymer swelling during the adsorption measurements (**Table 3.1**). However, both molecular modelling and gas adsorption analysis showed that PIM-OCP has a slightly higher BET surface area than PIM-OCF, for which the difference can be mainly accounted for simply by the greater mass of fluorine than hydrogen and its contribution to the mass of a repeat unit (668 g/mol for PIM-OCF versus 524 g/mol for PIM-OCP). Therefore, PIM-OCP would be expected to demonstrate a significantly higher N_2 and CO_2 adsorption than PIM-OCF (**Figure 3.4a and b**) even if the chain packing were identical, as suggested by packing simulation. The pore-size distributions of PIM-OCP and PIM-OCF were analysed by CO_2 adsorption using DFT model (**Figure 3.2c**), confirming that PIM-OCF has a denser packing and thus a slightly higher fraction of small micropores (< 0.5 nm) than PIM-OCP which has a greater contribution from larger micropores (>0.5 nm). Importantly, the PSDs from molecular modelling correlates well with the result from the CO_2 adsorption isotherm (**Figure 3.2d**), which validates the packing simulation. The molecular modelling demonstrates that PIM-OCP and PIM-OCF have similar fractional free volumes (FFV) of about 30%, which is almost as high as the ultrapermeable PIM-TMN-Trip (around 31%),[141] demonstrating the possibilities of obtaining membranes with high gas permeabilities.

Table 3.1 Physical properties of PIM-OCF and PIM-OCP.

Polymer	SA_{BET}[a] (m^2/g)	Modelling SA_{BET} (m^2/g)	V_{Total}[b] (ml/g)	CO_2 uptake[c] (mmol/g)	Solubility
PIM-OCF	928	625±43	0.74	2.6	THF, NMP
PIM-OCP	1062	802 ± 58	0.82	2.9	1,1,2,2-Tetrachloroethane (TCE)

[a] BET surface area (SA_{BET}) obtained from nitrogen adsorption at 77 k; [b] Total pore volume calculated from nitrogen uptake at P/P_o = 0.98; [c] CO_2 adsorption at 1 bar and 273 K.

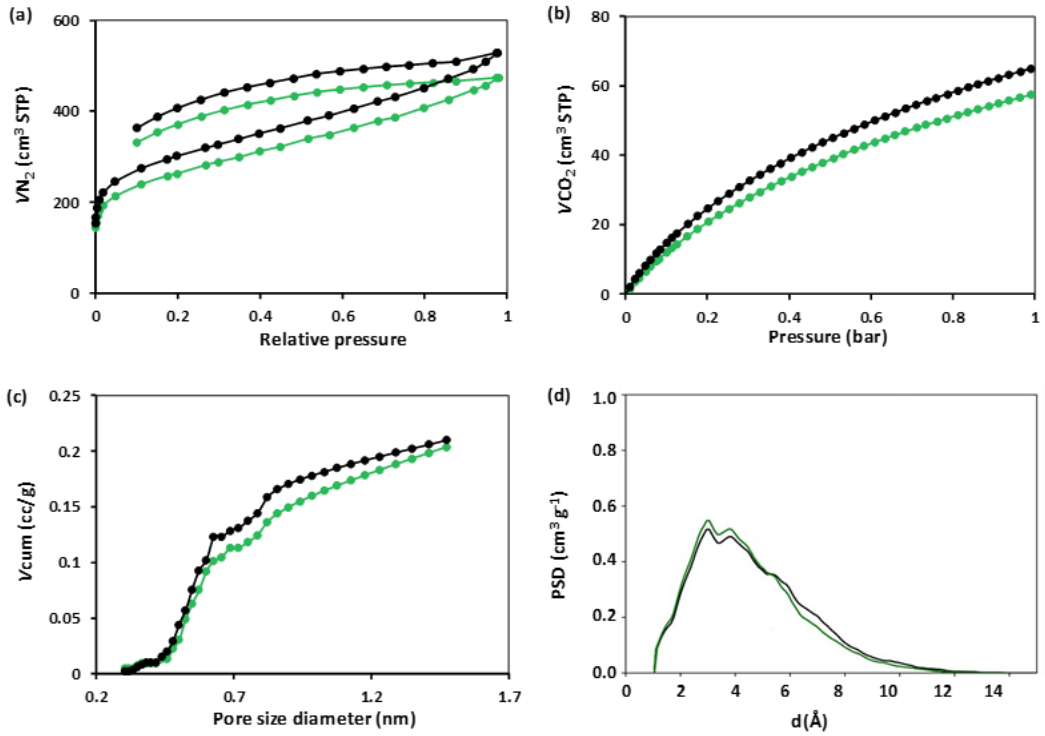

Figure 3.4 (a) Nitrogen adsorption and desorption isotherms at 77 K for powdered samples; (b) Carbon dioxide adsorption isotherms at 273 K for powdered samples. (c) Cumulative pore volume calculated from CO_2 adsorption data using non-local density functional theory (NLDFT) model; (d) Pore size distributions (PSDs) calculated from the molecular simulations.PIM-OCF (—) and PIM-OCP (—)

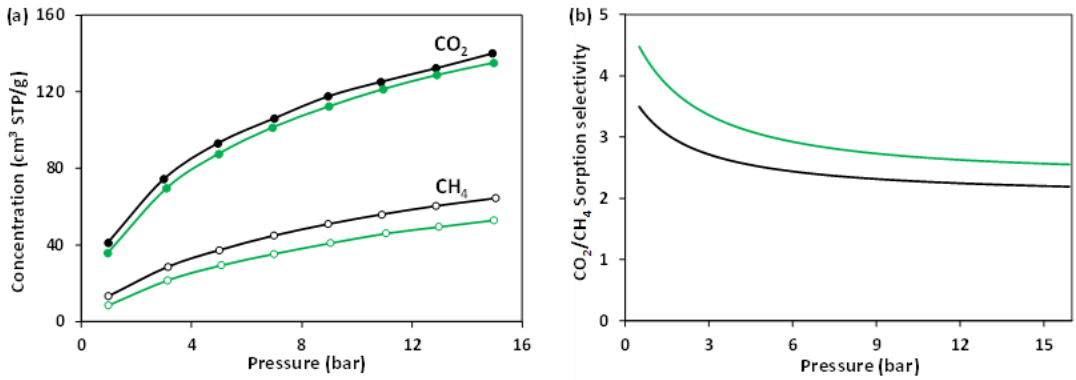

Figure 3.5 (a) CO_2 and CH_4 sorption isotherms for films at 25˚C from 1 to 15 bar fitted by dual-mode sorption (DMS) model. (b) Sorption selectivities at 25˚C from 1 to 15 bar fitted by dual-mode sorption (DMS) model. PIM-OCF (—) and PIM-OCP (—)

The CO_2 and CH_4 adsorption behaviours of PIM-OCP and PIM-OCF membranes were measured, by the Group of Prof. Karel Friess at the Institute of Chemical Technology, at 25

˚C with an increasing pressure from 1 to 15 bar, which shows a typical dual-model adsorption (**Figure 3.5a**). Both polymers demonstrated higher CO_2 sorption ability than CH_4, which is consistent with the condensability of gases. As shown in the adsorption isotherms, PIM-OCF possesses a significantly lower CH_4 sorption than PIM-OCP by around 20% as compared to a slightly lower CO_2 sorption by around 4% in the measured pressure range. Therefore, the CO_2 solubility coefficients calculated from the adsorption measurement are similar for PIM-OCF and PIM-OCP (41.2 and 39.3 $cm^3STP/cm^3/bar$, respectively) while the CH_4 solubility coefficients is decreased by 26% from 12.8 $cm^3STP/cm^3/bar$ of PIM-OCP to 9.5 $cm^3STP/cm^3/bar$ of PIM-OCF. These results illustrated the CH_4-phobic property of PIM-OCF induced by the fluorine atoms. Therefore, the CO_2/CH_4 sorption selectivity of PIM-OCF is higher than most of the reported PIMs including PIM-OCP (**Figure 3.5b**), and is only lower than the amino PIM-1 which converted the nitrile groups to the CO_2-philic amine groups.[171]

Films of the PIMs were sent to our collaborators at the Institute for Technology of Membranes (ITM), Italy for gas permeability measurements. Initial results were encouraging with both polymers demonstrating high permeability and excellent diffusivity selectivity due to their rigid structures. In addition, the preliminary results appeared to demonstrate the expected enhanced solubility selectivity S_{CO_2}/S_{CH_4} for PIM-OCF over PIM-OCP. However, some inconsistent results were obtained, presumably due to the failure to remove the casting solvent in one sample film. Further testing is planned but results for this thesis were delayed due to the Covid-19 lock-down in Italy in February 2020.

3.3 Perfluoroalkyl chain substituted benzomethanoanthracene based polymers

The above work has shown fluorines provide polymers with the CH_4-phobic property. Therefore, the perfluoroalkyl chain was introduced to benzomethanoanthracene units for polymer preparation to further improve their fluorine concentration. Furthermore, the long fluoroalkyl chains improve the hydrophobicity of polymers and is anticipated to enhance polymer separation performance in humid circumstances where water molecules have shown a significant negative impact on the permeability of PIM-1.[172].

3.3.1 Synthesis of perfluoroalkyl chain substituted benzomethanoanthracene based polybenzodoxin polymer

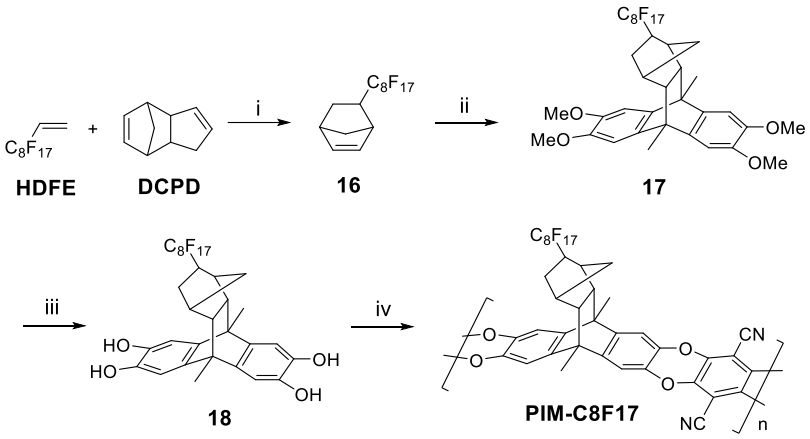

Scheme 3.4 Structure and synthesis of PIM-C8F17. Reagents and conditions: i. 200 °C, 0 bar, 2 h, microwave irradiation; ii. 9,10-Dimethyl-2,3,6,7-tetramethoxyanthracene, xylene, 260 °C, 96 h; iii. BBr_3, DCM, 3 h; iv. TFTPN, DMF, K_2CO_3, 65 °C, 72 h.

The synthesis route for the tetrahydroxybenzomethanoanthracene with the perfluoroalkyl chain substituent is shown in **Scheme 3.4**. The fluorinated norbornene **16** was synthesised via the Diels-Alder (DA) reaction between dicyclopentadiene (**DCPD**) and an excess of 1H, 1H, 2H-heptadecafluorodec-1-ene (**HDFE**) resulting in a mixture of endo/exo-isomers (with a 76% yield). The reaction temperature was higher than the cracking temperature of dicyclopentadiene, therefore dicyclopentadiene was used directly instead of using pre-cracked cyclopentadiene. This DA reaction was carried out under microwave irradiation at 200 °C without solvent. The polar C-F bonds in **HDFE** enables this reaction system to reach 200 °C in a few minutes without the need of a polar solvent (e.g., DMF). An excess of 1H,1H,2H-heptadecafluorodec-1-ene was used to prevent the self-polymerisation of cyclopentadiene. Compound **16** was then utilized as the dienophile in a second DA reaction to react with 2,3,6,7-tetramethoxy-9,10-dimethylanthracene affording the substituted tetramethoxylbenzomethanoanthracene **17** in a 41% yield as a mixture of isomers. Finally, the biscatechol monomer **18** was achieved in a quantitative yield by demethylation in DCM using BBr_3 as the Lewis acid.

Monomer **18** with a good solubility in DMF was used for the synthesis of the polybenzodioxin polymer PIM-C8F17 via the same polymerisation reaction with TFTPN as used for other PIMs

as described above. Unfortunately, the resulting polymer has poor solubility in either hydrocarbon or fluorinated solvents (e.g., dichloromethane, chloroform, tetrahydrofuran, *N*-methyl-2-pyrrolidone (NMP), N,N-dimethylformamide (DMF), quinoline, hexafluoroisopropanol (HFIP), trifluoroacetic anhydride (TFAA), hexafluorobenzene, perfluorohexane). This is probably due to the high fluorine density in PIM-C8F17. At last it was found to be soluble in a mixture of chloroform and trifluoroacetic anhydride with the volume ratio of 3:2. These two solvents are miscible with each other at such volume ratio at room temperature and have similar boiling points (61 °C and 40 °C for chloroform and trifluoroacetic anhydride, respectively). A freestanding film of PIM-C8F17 was prepared by solution casting method using this solvent mixture (**Figure 3.6a**). After drying at ambient condition, this membrane was soaked in methanol for 24 h and then dried under vacuum at 40 °C to remove solvent residual. The complete removal of casting solvent was confirmed by thermogravimetric analysis where there is no evident mass loss before 150 °C. The onset temperature of the decomposition of PIM-C8F17 is at around 319 °C originating from the reverse Diels-Alder reaction of the bridged-bicyclic structure.

3.3.2 Synthesis of perfluoroalkyl chain substituted benzomethanoanthracene based Tröger base polymer

The Tröger base (TB) polymer was prepared using the perfluoroalkyl chain substititued diaminobenzomethanoanthracene. The highly rigid, bridged diazocene ring in the TB polymer provides a near 90° angle to adjacent monomeric units, which is different from the dibenzodioxin linkage provide a coplanar arrangement. Therefore, the polymer chains of PIM-C8F17-TB are three dimensional in space which was expected to have lower interchain interactions and thus better solubility than PIM-C8F17 with 2D polymer chains.

The synthesis route for the fluorinated diaminobenzomethanoanthracene is shown in **Scheme 3.5**. Compound **19** was achieved in a 62% yield with a mixture of isomer products via the DA reaction between **16** and anthracene under microwave irradiation at 250 °C. This microwave-assisted DA reaction was also utilised a solvent free condition because anthracene (Mp = 218 °C) melts at the reaction temperature. Compound **19** was then nitrated using potassium nitrate and trifluoroactic anhydride to afford **20** in a yield of 83%. The nitrate

product **20** can be easily reduced by tin powder in a hydrochloric acid/ethanol mixture to provide the desired product **21** in a 94% yield.

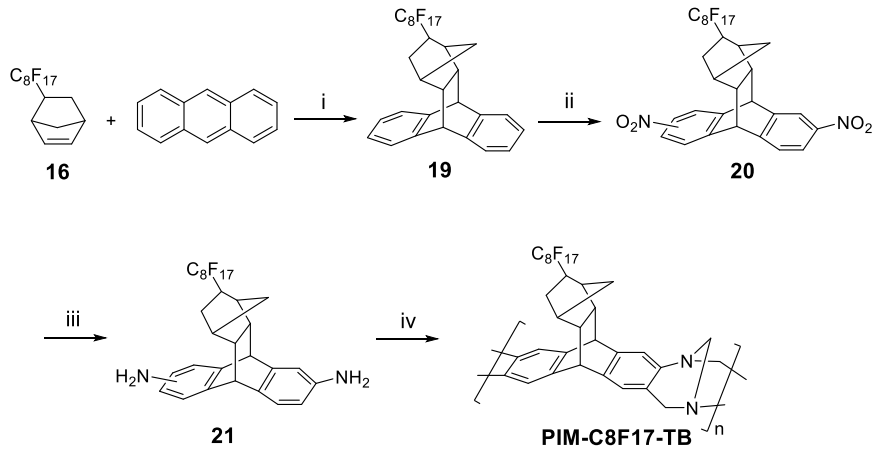

Scheme 3.5 Structure and synthesis route for PIM-C8F17-TB. Reagents and conditions: i. 250 °C, 10 bar, 4 h, microwave irradiation; ii. KNO_3, TFAA, RT; iii, HCl/ethanol, tin powder, refluxing for 24 h; iv. Dimethoxymethane (DMM), trifluoroacetic acid (TFA), RT.

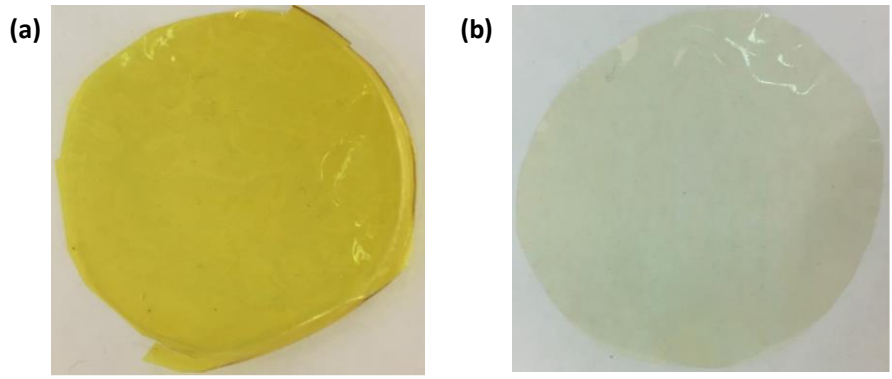

Figure 3.6 The photos for (a) PIM-C8F17 and (b) PIM-C8F17-TB freestanding films.

Following the standard TB polymerisation procedure developed by our group, one equivalent of diamine **21** was dissolved in five equivalents of dimethoxymethane at 0 °C. TFA was then added dropwise to the reaction system at 0 °C, the reaction mixture was then left stirring at room temperature. After 16 hours, the solution reached a desired viscosity and then was quenched by adding ammonium hydroxide. As expected, the resulting polymer has a good solubility in HFIP and a high molecular weight for film formation. An optically clear and robust film of PIM-C8F17-TB was prepared by casting from its HFIP solution and treated with methanol to remove the residual HFIP (**Figure 3.6b**).

3.3.3 Gas transport property

The microporous properties of PIM-C8F17 and PIM-C8F17-TB were investigated by analysing their N_2 and CO_2 adsorptions. The BET surface area of PIM-C8F17 powder is about 569 m^2/g calculated from N_2 adsorption isotherm at 77 K. A significant uptake of N_2 at low relative pressure was observed, indicating the microporous property of PIM-C8F17 (**Figure 3.7a**). Surprisingly, PIM-C8F17-TB powder showed low N_2 uptake at low relative pressure, suggesting limited micropores accessible to N_2. As a result, an extremely low surface area (25 m^2/g) was calculated from the N_2 adsorption isotherm. This is most likely because the pores (which are accessible to N_2 in PIM-C8F17-TB) are instead occupied by the flexible long fluorinated side group. In contrast, PIM-C8F17-TB exhibit a high CO_2 uptake at low pressure compared to N_2, and is even higher than PIM-C8F17 (**Figure 3.7b**). This reflects a high concentration of small micropores (which are accessible to CO_2) in PIM-C8F7-TB cannot be filled in by the bulky side group. As shown in PSDs calculated from CO_2 adsorption using the NLDFT model (**Figure 3.7c**), PIM-C8F17-TB has a slightly higher fraction of ultramicropores (< 0.7 nm), while experiences a significant reduction in micropores (> 0.7 nm) as compared to PIM-C8F17.

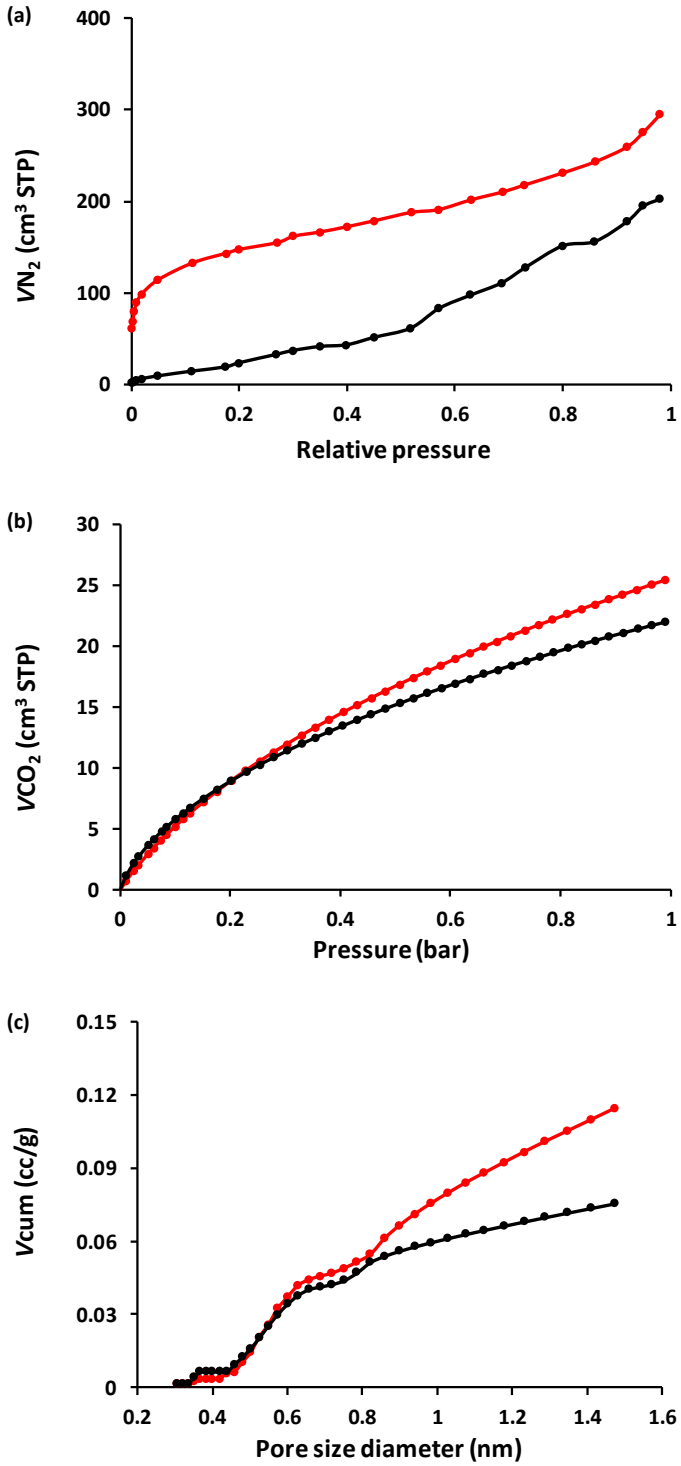

Figure 3.7 (a) Nitrogen adsorption isotherms at 77 K for powdered samples; (b). Carbon dioxide adsorption isotherms at 273 K for powdered samples; (c) Cumulative pore volume calculated from CO_2 adsorption data using non-local density functional theory (NLDFT) model; PIM-C8F17 (●), PIM-C8F17-TB (●).

The gas permeability data for freshly methanol-treated films of PIM-C8F17 and PIM-C8F17-TB were placed on the Robeson plots and compared to that of PIM-1 (**Figure 3.3**). Although PIM-C8F17 (569 m^2/g) possesses a lower surface area than PIM-1 (720 – 820 m^2/g), it shows higher permeabilities for all gases measured (**Table 3.2**). This is probable due to the local motion of the flexible side groups on PIM-C8F17 which facilitates the diffusion of penetrants in the polymer matrix especially for larger molecules (i.e., CH_4), as confirmed by the higher diffusivity coefficients of PIM-C8F17 than those of PIM-1 (**Table 3.3**). Therefore, the size selectivity of PIM-C8F17 was mitigated, which reduces the polymer overall selectivity. With the low gas selectivity, PIM-C8F17 locates below the 2008 Roberson upper bounds for CO_2/CH_4 and CO_2/N_2 and locates on the 1990 upper bound for H_2/CH_4. However, the abundant C-F bonds in PIM-C8F17 provides this polymer with a high solubility selectivity for He/CH_4, contributing to a better gas separation performance for PIM-C8F17 compared with PIM-1. As shown in **Figure 3.8**, PIM-C8F17 locates on the 1991 upper bound for He/CH_4, where PIM-1 falls below the upper bound. With the low surface area, PIM-C8F17-TB displayed lower gas permeabilities coupled with higher selectivities than PIM-C8F17, obeying the typical 'trade-off' relationship between gas permeability and selectivity.

Table 3.2 Ideal gas permeabilities (P_x, Barrer) and selectivities ($\alpha_{x/y}$) of freshly methanol treated films of PIM-C8F17 and PIM-C8F17-TB measured at 25 ˚C and 1 bar of feed pressure.

Polymer	P_{N_2}	P_{O_2}	P_{CO_2}	P_{CH_4}	P_{H_2}	P_{He}	α_{CO_2/CH_4}	α_{CO_2/N_2}	α_{H_2/CH_4}	α_{He/CH_4}
PIM-1	773	2135	12775	1281	4711	1830	9.97	16.5	3.68	1.43
PIM-C8F17	2147	4053	20862	3137	6964	3693	6.65	9.72	2.22	1.18
PIM-C8F17-TB	91	241	986	120	579	459	8.21	10.8	4.82	3.82

Table 3.3 Diffusivity coefficients (D_x, 10^{-12} m^2/s) and diffusivity selectivities (D_X/D_Y) of freshly methanol treated films of PIM-C8F17 and PIM-C8F17-TB measured at 25 ˚C and 1 bar of feed pressure.

Polymer	D_{N_2}	D_{O_2}	D_{CO_2}	D_{CH_4}	D_{H_2}	D_{He}	D_{CO_2} /D_{CH_4}	D_{CO_2} /D_{N_2}	D_{H_2} /D_{CH_4}	D_{He} /D_{CH_4}
PIM-1	186	512	226	79	4200	5500	2.9	1.2	53	70
PIM-C8F17	-	1126	497	282	5103	5050	1.7	-	10	18
PIM-C8F17-TB	39	87	26	13	1419	3380	2.0	0.7	109	260

Table 3.4 Solubility coefficients (S_X, cm^3_{STP} cm^{-3} bar^{-1}) and solubility selectivities (S_X/S_Y) of freshly methanol treated films of PIM-C8F17 and PIM-C8F17-TB measured at 25 ˚C and 1 bar of feed pressure.

Polymer	S_{N_2}	S_{O_2}	S_{CO_2}	S_{CH_4}	S_{H_2}	S_{He}	S_{CO_2} /S_{CH_4}	S_{CO_2} /S_{N_2}	S_{H_2} /S_{CH_4}	S_{He} /S_{CH_4}
PIM-1	3.52	3.54	48.1	13.7	0.17	0.19	3.51	13.7	0.01	0.01
PIM-C8F17	-	2.70	31.5	8.4	1.02	0.55	3.75	-	0.12	0.06
PIM-C8F17-TB	1.76	2.08	28.1	7.1	0.31	0.10	3.96	16.0	0.04	0.02

Although the overall performance of PIM-C8F17 and PIM-C8F17-TB are not as good as most of the reported PIMs, they may provide a promising performance for hydrogen recovery in refineries. The high concentration of hydrocarbon vapor (C_1-C_5) in the refinery gas streams limit the separation efficiency of hydrocarbon membranes due to the fouling, plasticization and condensation of hydrocarbon vapor on the membrane surfaces. In contrast, the low hydrocarbon sorption in these two fluorinated polymers may mitigate these issues making membrane more stable under high hydrocarbon vapor conditions, which is the subject to the future research. In addition, the performance of PIM-C8F17 and PIM-C8F17-TB under humid conditions will be investigated as well. Furthermore, the presented data is only for freshly methanol treated films. The rate of aging may be modified for these polymers so that they retain their high permeability for longer than other PIMs. This too may have advantages for some applications. For example, contact membranes are used to help dissolve CO_2 in aqueous base or amine solvents and require high, stable CO_2 permeability but extreme hydrophobicity to prevent the water blocking transport. Hence PIM-C8F17 may be useful for this specific application.

In this chapter, a fluorinated and non-fluorinated PIMs (PIM-OCF and PIM-OCP) derived from benzomethanoanthracene were achieved. The benzomethanoanthracene unit was synthesised with an easier procedure and provided polymers with a better solubility as compared with the benzotriptycene unit. As expected, fluorine atoms showed a minor effect on chain packing behaviour confirmed by the molecular simulation of PIM-OCF and PIM-OCP. However, fluorine atoms decreased the CH_4 sorption of PIM-OCF, leading to a higher sorption selectivity of PIM-OCF than that of PIM-OCP. The perfluoroalkyl chain substitutes was also observed to reduce the CH_4 sorption. Therefore, fluorination of polymers is an effective way to improve solubility selectivities of CH4 relating gas pairs.

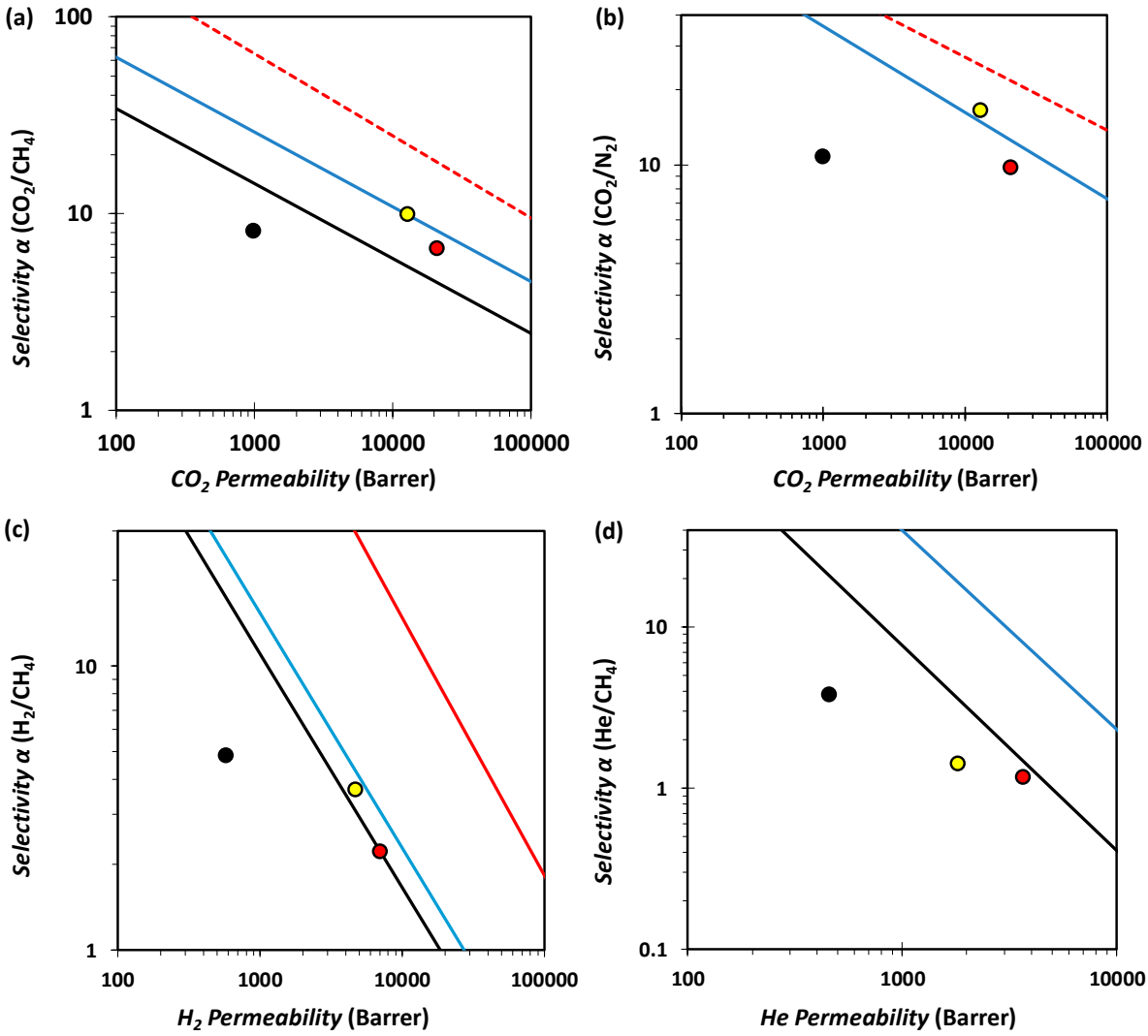

Figure 3.8 Robeson plots for the (a) CO_2/CH_4, (b) CO_2/N_2, (c) H_2/CH_4 and (d) He/CH_4 gas pairs showing the position of the fresh films of PIM-C8F17 (●), PIM-C8F17-TB (●) and PIM-1 (●). The black and blue lines represent the 1991 and 2008 upper bounds, the red solid line is the proposed 2015 upper bound for H_2/CH_4, and the dotted red lines are the revised 2019 upper bounds for CO_2/N_2 and CO_2/CH_4.

Chapter 4 Dibenzomethanopentacene (DBMP)-derived polybenzodioxin polymers for gas separation

4.1 Dibenzomethanopentacene (DBMP)/Tetramethylspirobisindane (TTSBI) Co-polymers

4.1.1 Introduction

The two previous chapters demonstrate PIMs built by triptycenes or related bridged bicyclic units to attempt to overcome the challenge posed by the permeability/selectivity tradeoff and defined new 2019 upper bounds for CO_2/CH_4 and CO_2/N_2.[141, 155] Molecular simulations and experimental measurements reveal that the exceptional performance of these PIMs is due to the two-dimensional (2D) ladder polymer structure leading to a more finely tuned microporosity relative to its 3D counterpart.[141] This exciting observation encourages us to design new polymers with 2D ribbon-like structure to explore the separation potential of this class of polymer.

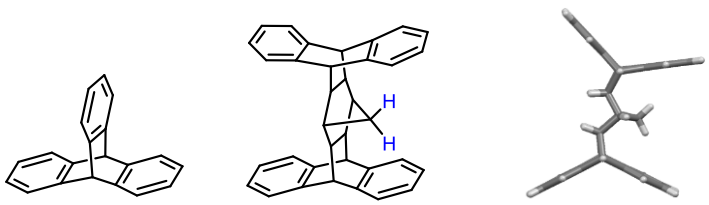

Figure 4.1 Structure of Dibenzomethanopentacene (DBMP).

Dibenzomethanopentacene (DBMP) has a similar 2D structure to triptycene, but is bulkier (**Figure 4.1**). 2D ladder polymer chains can be constructed with DBMP as the building block connected via dibenzodioxin linking groups. Although not previously reported in the literature, DBMP is easily prepared via the Diels-Alder addition between anthracene and norbornadiene. This molecule has a unique structure with two hydrogens on the methano-bridge inserting directly inside the adjacent aromatic rings as confirmed by their negative

chemical shift in the ^{1}H NMR spectrum of DBMP, similar to that found for benzomethanoanthracene-based PIMs. This unique geometry prevents the bending vibration of the anthracene wings and thereby enhances the rigidity of DBMP. In addition, DBMP provides abundant substitution sites on its benzene rings, which offers great opportunities to prepare polymers with distinct properties, such as enhanced gas diffusivity selectivity and solubility selectivity.[155] The simple preparation, high rigidity, versatile possibilities for substitution and 2D geometry structure make DBMP an attractive building unit for PIMs. In this chapter, DBMP-based full ladder PIMs and their properties are reported.

4.1.2 Synthesis of dibenzomethanopentacene (DBMP) monomer

It was hoped that tetramethoxy-DBMP could be synthesised via the Diels-Alder 2:1 cycloaddition between 2,3-dimethoxyanthracene **24** and norbornadiene. Initial attempts to synthesize 2,3-dimethoxyanthrancene **24** were carried out according to the procedure reported by Rafiq *et al*[173], as shown in **Scheme 4.1.** In this method, 1,3-dimethoxy-1,3-dihydroisobenzofuran **a** was firstly synthesised using *o*-phthalaldehyde (**OPA**) and methanol in acidic media (trifluoroacetic acid, TFA) followed by benz-annulation with veratrol in the presence of triflic acid (CF_3SO_3H) to afford **24** in a high yield of 84% but in milligram scale. However, for this work, the reported method was required to be scaled up to provide multi-gram quantities. The purified 1,3-dimethoxy-1,3-dihydroisobenzofuran **a** was achieved in a 63% yield, and was used to synthesise **24** using the same condition as reported. However, an unexpected low yield of 4.5% was observed. The crude product was analysed by ^{1}H NMR. The major components were found to be unreacted veratrol and *o*-phthalaldehyde (converted from **a**), while the expected product **24** was generated in an unacceptably low yield. In order to improve the yield, an extended reaction time from 2 h to 24 h was applied, but a similar yield was observed (by comparing the crude NMR spectra). On the other hand, the amount of acid was increased from 1 to 2 equivalents. It was found that the increased acid improved the conversion rate of acetal to aldehyde, whereas the product **24** could not be generated.

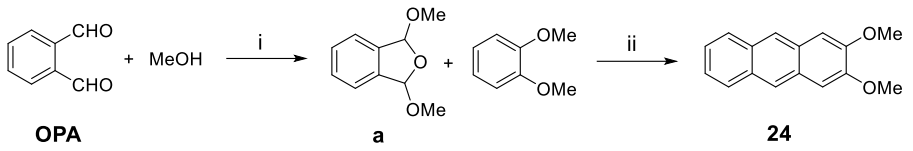

Scheme 4.1 Attempt synthesis of 2,3-dimethoxylanthrancene **2**. Reagents and conditions: i, TFA, RT, 24 h; ii. CF_3SO_3H, anhydrous EtOH, anhydrous DCM, RT, 2 h.

An alternative protocol reported by J. Veerman *et al*[174] was adopted to prepare **24** in a multi-gram scale (**Scheme 4.2**). The synthesis included the Friedel-Crafts acylation of phthalic anhydride (**PA**) with veratrol in the presence of Lewis acid $AlCl_3$ (obtaining **22**), followed by acid-mediated (methanesulfonic acid, $MeSO_3H$) cyclization (giving **23**) and reduction using sodium borohydride to afford **24**. This method yielded **24** in a large scale with an easy work-up procedure.

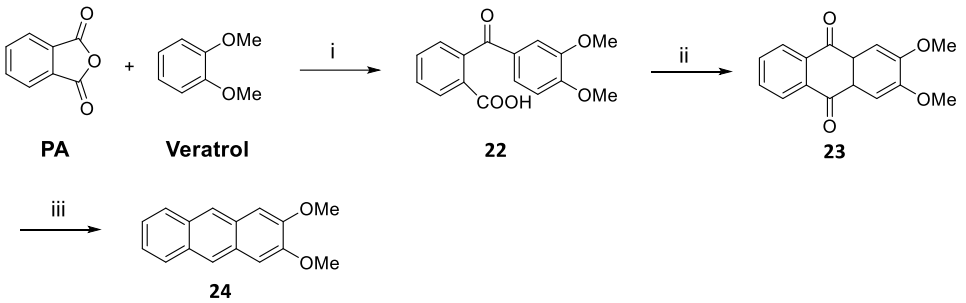

Scheme 4.2 Synthesis of 2,3-dimethoxylanthrancene **2**. Reagents and conditions: i. $AlCl_3$, 50 °C, 24 h; ii. $MeSO_3H$, 70 °C, 24 h; iii, $NaBH_4$, *i*-PrOH, 110 °C, 96 h.

DBMP monomers were prepared using the synthetic route shown in **Scheme 4.3**. The Diels-Alder reaction between **24** and norbornadiene was conducted in a sealed reaction vessel using xylene as the solvent at 260 °C for 96 h. After demethylation using BBr_3, three DBMP biscatechols were obtained with high purity and high total yield of over 90%. After the Diels-Alder cycloaddition, the three regioisomers of **25** were isolated via silica gel column chromatography with the ratio of 2.3:1.2:1 in a total yield of 67%. The three isomers can be identified by their ^{1}H NMR spectra. Isomer **25a** has five resonances in the aromatic region in ^{1}H NMR spectrum, while isomer **25b** and **25c** only have three in the same region due to their higher symmetry than **25a**. Notably, the protons on the methano-bridge of DBMP isomers have unique negative proton resonances (δ_H = -0.9 ppm) in ^{1}H NMR spectra (**Figure 4.2**). It implies these two hydrogens are placed directly inside the adjacent aromatic rings which

have pronounced shielded effect on them. Additionally, the methano-bridge protons of isomer **25b** are more shielded compared to those of isomer **25c** due to the higher electron density of the methoxylbenzene structure in **25b** than the benzene rings in **25c**. Therefore, the protons on the methano-bridge carbon of isomer **25b** appear in a relatively high-field position. These protons on **25a** are split into two resonances due to their different chemical environments, which further confirms the asymmetric structure of **25a**.

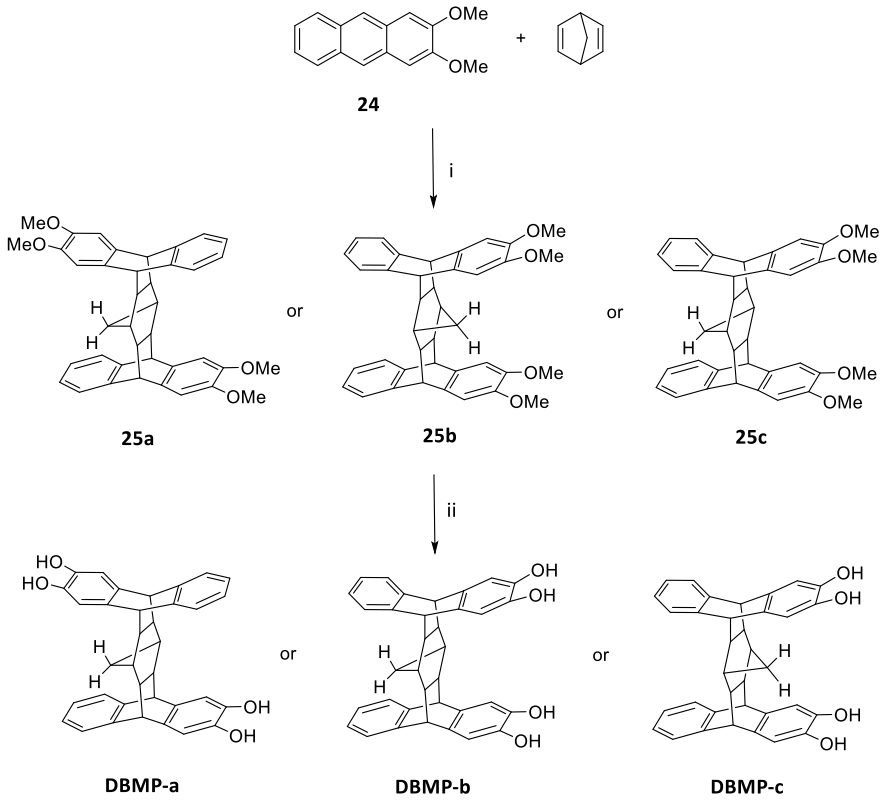

Scheme 4.3 Synthesis of the **DBMP** regiosomer monomers. Reagents and conditions: i. Xylene, 260 °C, 96 h; ii, BBr_3, DCM, RT, 3 h.

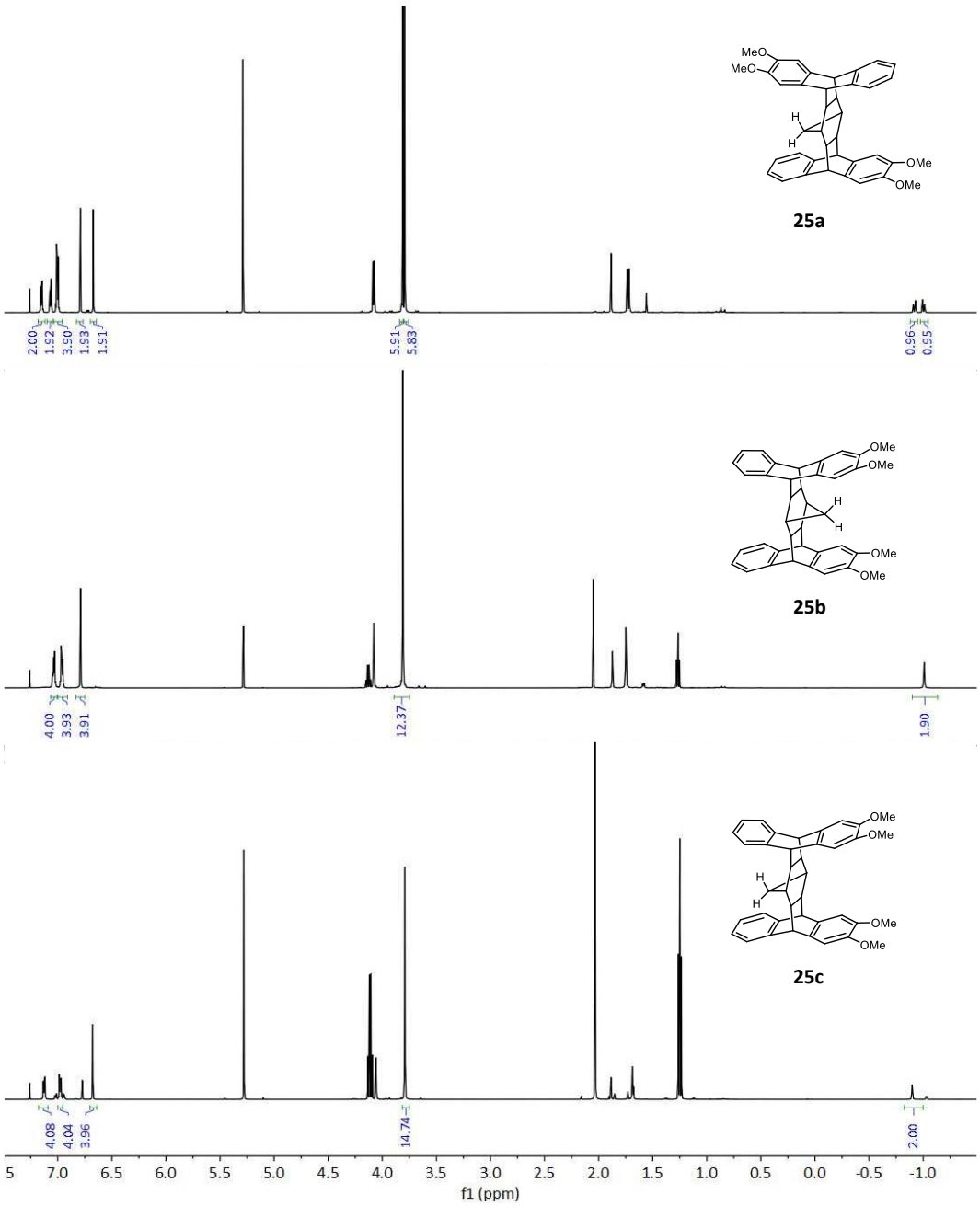

Figure 4.2 The NMR spectra of tetramethoxyl-DBMP isomers **25**.

4.1.3 Synthesis of DBMP based polymers (PIMs-DBMP)

These three monomers DBMP-a, DBMP-b and DBMP-c can be divided into two types based on the relative positions of catechol moieties on DBMP: *'trans-like'* orientation (DBMP-a) and *'cis-like'* orientation (DBMP-b and DBMP-c). In the Group's previous work on hexaphenylbenzene-based PIMs (HPB-PIMs),[175] it was reported that the molecular weight of

obtained PIMs varied significantly with the positions of catechol moieties relative to the central core of HPB. Polymerisation of the *meta*-HPB provided a polymer with high molecular weight allowing the successful formation of flexible self-standing films, while the *ortho*-HPB monomer mainly generated cyclic oligomers. In this work, the two types of monomers were polymerised with 2,3,5,6-tetrafluoroterephthalonitrile (TFTPN) separately using the general procedure for polybenzodioxin polymers (**Scheme 4.4**). PIM-DBMP-1 is based on DBMP-a and PIM-DBMP-2 is polymerised using DBMP-b and DBMP-c. These two polymers can only dissolve in the high boiling point solvent quinoline. Their poor solubility prohibits molecular weight analysis by Gel Permeation Chormatography (GPC). It was observed that PIM-DBMP-2 exhibited better solubility than PIM-DBMP-1, possibly because PIM-DBMP-2 (based on the '*cis-like*' monomer) contains more cyclic oligomers (**Scheme 4.4**) similar to HPB-PIMs. During film formation, the polymer solution of PIM-DBMP-1 turned into a thick gel-like matrix, while further concentration gave a cracked membrane (**Figure 4.3a**). The membrane of PIM-DBMP-2 also broke during casting but with less shrinking (**Figure 4.3b**). As known, the polymer molecular weight obtained by polycondensation is affected by monomer concentrations, reaction temperature and reaction time. Optimisation of the polymerisation was conducted by increasing the concentration of DBMP-a from 0.08 mmol/mL to 0.11 mmol/mL, elevating the reaction temperature to 80 °C and extending the reaction time to 120 h, but an insoluble polymer was obtained.

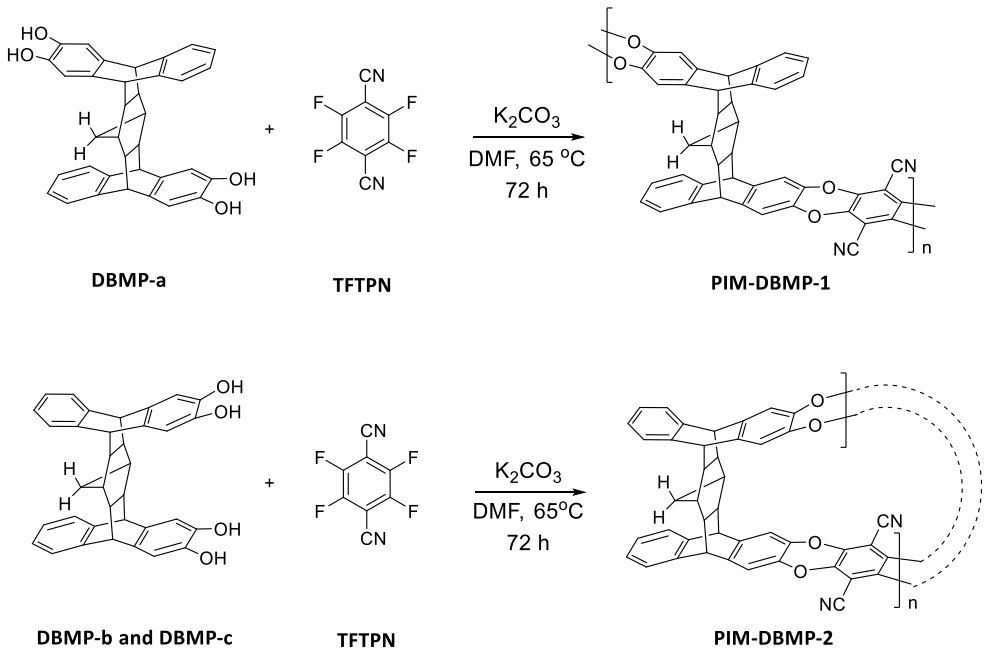

Scheme 4.4 Structure and synthesis of the PIMs-DBMP.

(a) 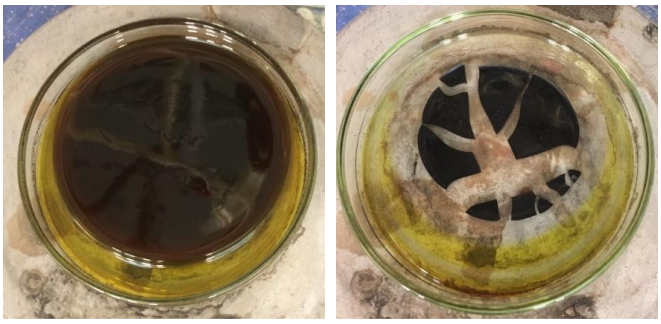 (b) 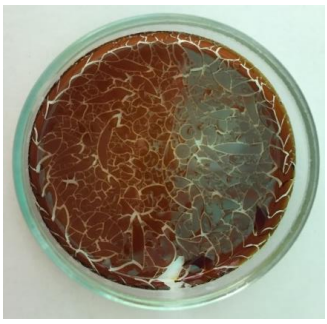

Figure 4.3 Membrane photos for (a) PIM-DBMP-1 and (b) PIM-DBMP-2.

In an attempt to explore the effect of DBMP units on the performance of gas separations, a series of copolymers composed of DBMP, commercially available TTSBI (the monomer used for PIM-1) and TFTPN were synthesised in a one-step polycondensation reaction and denoted as PIM-DBMP-co-TTSBI (m:n) (m:n represents the ratio of DBMP:TTSBI, **Scheme 4.5**). The polymerisation conditions for copolymers with different monomer ratios were the same as those for homopolymer PIM-DBMP-1 (**Scheme 4.5**). Their physical properties are listed in **Table 4.1** for comparison. Copolymers with DBMP contents less than 50% have good solubility in $CHCl_3$. Their average molecular weights (M_w) are in the range of 65000-120000 g mol^{-1} estimated by GPC (**Table 4.1)**. When DBMP contents exceed 75%, the copolymers are only soluble in quinoline. The diminished solubility of polymers may be due to the limited movement of the highly rigid ladder polymer segments built by DBMP or to their 2D structure. The improved rigidity was confirmed by the increased Young's modulus from 1247 MPa of PIM-1 membrane to 3145 MPa of PIM-DBMP-co-TTSBI (25:75) membrane measured by atomic force microscopy (AFM) (**Table 4.1**).[176]

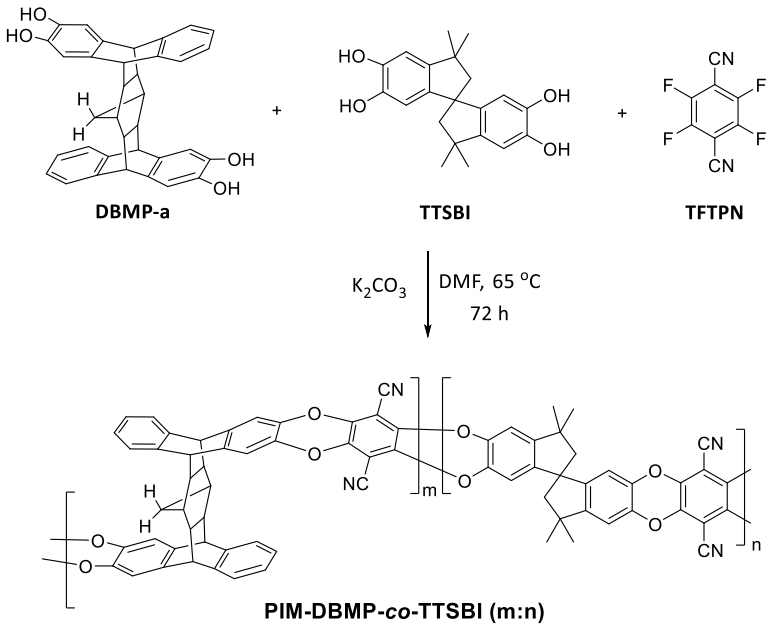

Scheme 4.5 Structure and synthesis of copolymers PIM-DBMP-*co*-TTSBI (m:n).

Table 4.1 Physical properties of DBMP-TTSBI copolymers.

Polymer	M_w (g/mol)	M_w/M_n	SA_{BET}[a] (m^2/g)	CO_2 uptake[b] (mmol/g)	V_{Total}[c] (ml/g)	Young's modulus (Mpa)	Solubility
PIM-DBMP-1	—[d]	—[d]	790	2.4	0.73	-	Quinoline
PIM-DBMP-*co*-TTSBI (90:10)	—[d]	—[d]	817	2.4	0.73	-	Quinoline
PIM-DBMP-*co*-TTSBI (75:25)	—[d]	—[d]	728	2.4	0.54	3145	Quinoline
PIM-DBMP-*co*-TTSBI (50:50)	65 000[e]	2.3	830	2.6	0.67	2873	$CHCl_3$
PIM-DBMP-*co*-TTSBI (25:75)	71 000[e]	1.7	760	2.4	0.62	2554	$CHCl_3$
PIM-DBMP-*co*-TTSBI (10:90)	125 000[e]	2.1	801	2.5	0.66	2422	$CHCl_3$
PIM-1	213 000[e]	2.4	774	2.0	0.57	1247	$CHCl_3$

[a] BET surface area (SA_{BET}) calculated from N_2 adsorption isotherm obtained at 77 K. [b] CO_2 uptakes at 1 bar/273 K. [c] Total free volume (V_{Total}) estimated from N_2 adsorption at P/P_o = 0.98. [d] Not measured due to insolubility in an appropriate solvent for GPC. [e] From GPC analysis relative to polystyrene standards.

Due to the solubility issue, the monomer compositions of PIM-DBMP-co-TTSBI (90:10) and PIM-DBMP-co-TTSBI (75:25) cannot be confirmed by ^{1}H NMR and therefore, this set of copolymers were characterised by thermal gravimetric analysis (TGA). PIM-DBMP-1 shows a

weight loss at the onset temperature around 359 °C due to the release of norbornadiene molecules resulting from the reverse Diels-Alder reaction of DBMP units (**Figure 4.4**), while PIM-1 remains stable until 500 °C. Therefore, the DBMP contents in copolymers can be estimated from TGA analysis. As expected, the copolymers exhibit weight loss in the same temperature range with PIM-DBMP-1 (**Figure 4.4**). The experimental weight losses of PIM-DBMP-co-TTSBI (90:10) and PIM-DBMP-co-TTSBI (75:25) are 12.1% and 10.7% at onset temperature of 359 °C, which is comparable with the theoretical values of 13.5% and 11.7% (calculated by comparing molecular weights of lost unit with the entire repeating unit). This indicates that the real monomer compositions of copolymers are consistent with the molar ratio of the feeding monomers. In the same manner, the compositions of more soluble copolymers were also assessed by TGA. The weight losses at 359 °C of PIM-DBMP-co-TTSBI (50:50), PIM-DBMP-co-TTSBI (25:75) and PIM-DBMP-co-TTSBI (10:90) are 9.4%, 4.7% and 1.9%, respectively, as recorded in the **Figure 4.4**, which are approximate equal to the theoretical values of 8.4%, 4.6% and 1.9%.

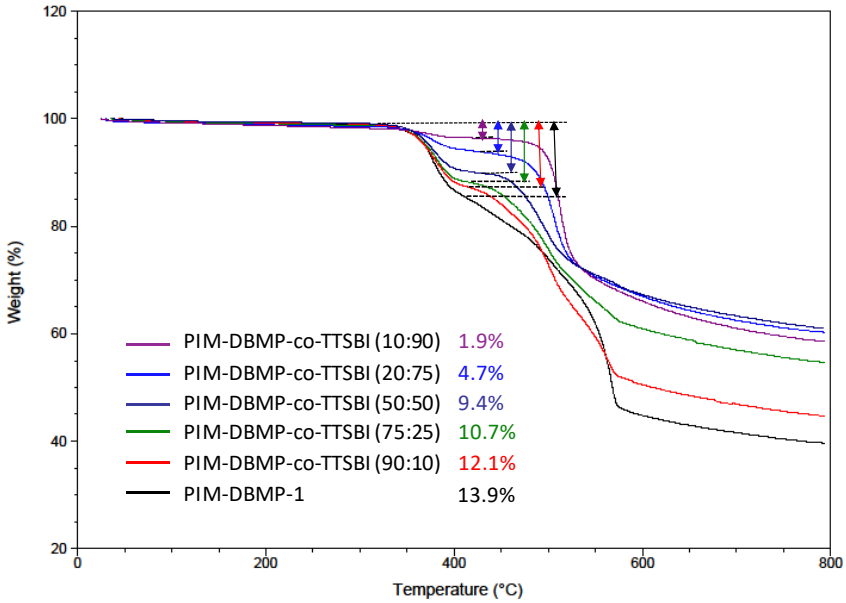

Figure 4.4 TGA analysis of PIM-DBMP-1 and PIMs-DBMP-*co*-TTSBI (m:n)

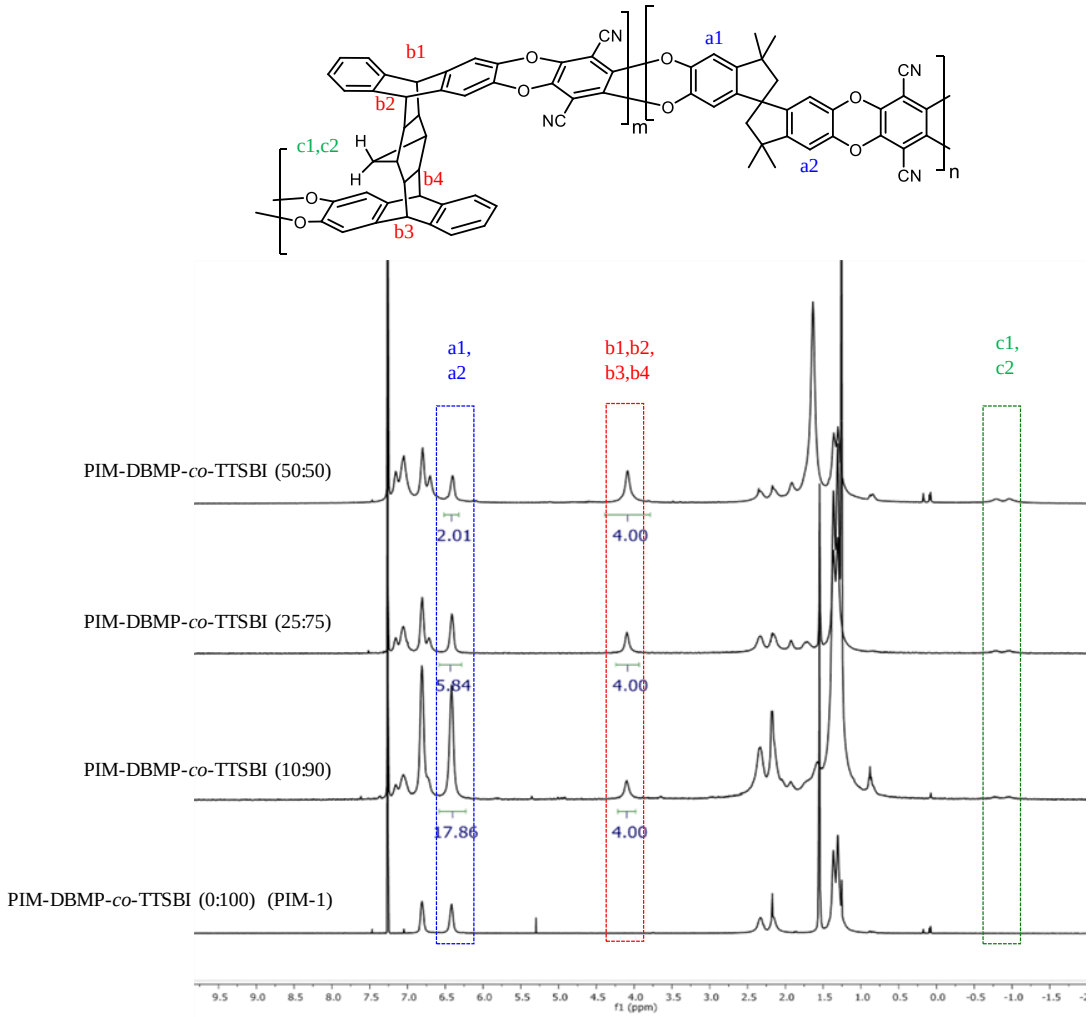

Figure 4.5 The NMR spectra for PIM-1 and PIMs-DBMP-co-TTSBI (m:n) in $CDCl_3$.

The monomer compositions of the more soluble copolymers were further confirmed using ^{1}H NMR by the integration of resonances specific to DBMP and TTSBI, as illustrated in **Figure 4.5** (the PIM-1 spectrum is included for comparison). The ^{1}H NMR spectra of the copolymers contain similar resonances to PIM-1, because of the presence of the same monomer TTSBI. The distinct signal at δ_H 6.44 ppm derives from the aromatic protons (**a1** and **a2**) of TTSBI monomers and the signal at δ_H 4.11 ppm originates from the bridgehead protons (**b1-b4**) of DBMP monomers (**Figure 4.5**). The monomer ratio of copolymers were determined to be 1:1, 1:3 and 1:9 for PIMs-DBMP-*co*-TTSBI (50:50), PIMs-DBMP-*co*-TTSBI (25:75) and PIMs-DBMP-*co*-TTSBI (10:90), respectively, according to the integral ratio of the two resonances at δ_H 6.44 and 4.11 ppm. In addition, the characteristic negative shifts (δ_H = -0.9 ppm) of DBMP units corresponding to the protons (**c1, c2**) on the methano-bridge carbon were clearly observed in the ^{1}H NMR of copolymers, further confirming the presence of DBMP units (**Figure 4.5**). All

of the abovementioned analysis indicate that the copolymers were successfully achieved in a one-step polycondensation via an aromatic double nucleophilic substitution between monomers of DBMP, TTSBI and TFTPN.

4.1.4 Microporosity analysis and gas transport property

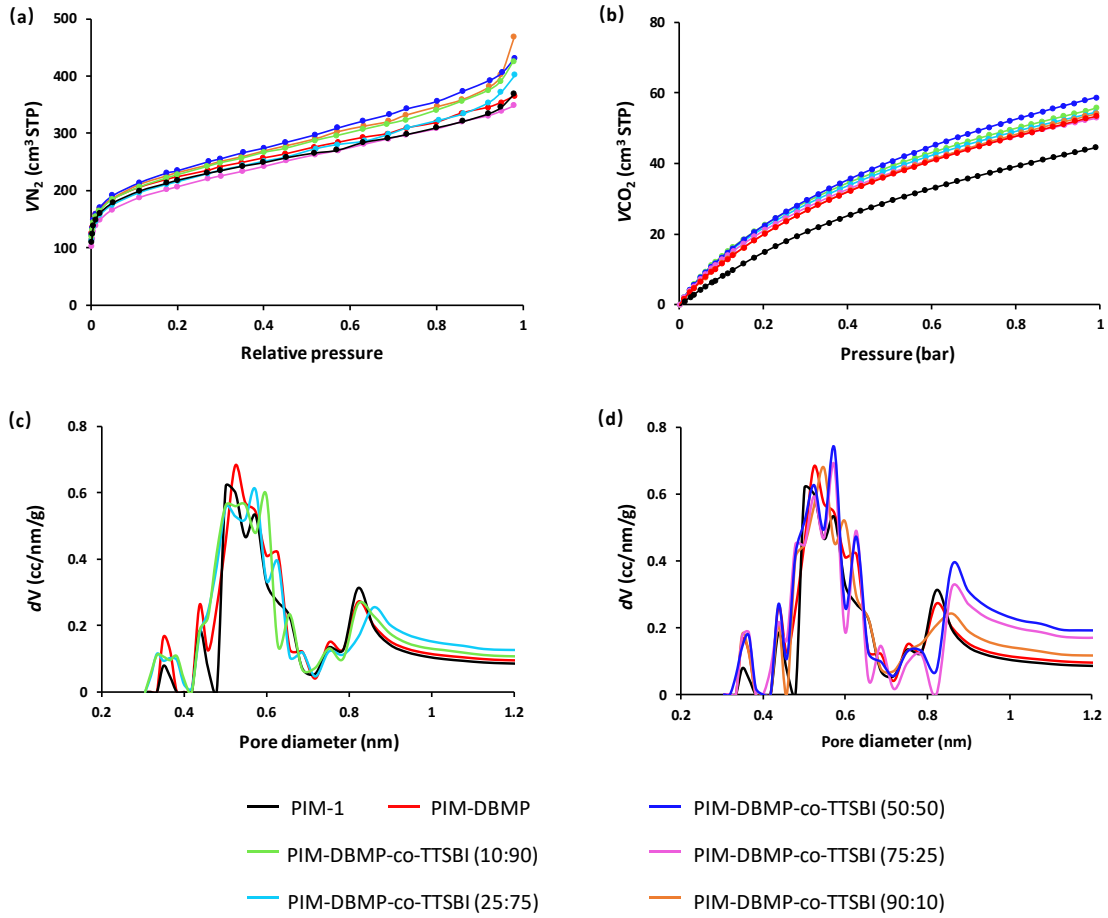

Figure 4.6 (a) N_2 adsorption isotherms at 77 K for powdered samples; (b). CO_2 adsorption isotherms at 273 K for powdered samples; (c) Pore size distribution (PSD) calculated from CO_2 adsorption data using non-local density functional theory (NLDFT) model based on carbon slit-pore geometry.

The impact of DBMP units on the microstructure of polymers was qualitatively investigated by gas physisorption and pore-size distribution (PSD) analyses. The N_2 adsorption isotherms obtained at 77 K for all the polymers show high N_2 uptakes at low relative pressure (P/P_o < 0.1 bar) (**Figure 4.6a**), indicative of microporous structure. All PIM-DBMP copolymers and PIM-1 possess similar BET surface areas (SA_{BET}) in the range 730-830 m^2/g (**Table 4.1**).

Increasing the amount of DBMP appears to enhance N_2 uptake marginally but overall the N_2 isotherms are all comparable to that of PIM-1. For CO_2 uptake at 273 K, all copolymers demonstrate similar isotherms with significantly larger gas adsorption than PIM-1 (**Figure 4.6b**), indicating the greater concentration of ultramicropores (< 0.7 nm) after incorporation of DBMP (**Figure 4.6c and d**).

The flexible free-standing membranes of PIM-DBMP-*co*-TTSBI (10:90), (25:75) and (50:50) were cast from their chloroform solutions, and PIM-DBMP-*co*-TTSBI (75:25) membrane was cast from the quinoline solution (**Figure 4.7**). Unfortunately, PIM-DBMP-*co*-TTSBI (90:10) failed to cast presumably because of the high DBMP proportion. The resultant membranes were soaked in methanol and then dried under vacuum oven at 40 °C for 24 h to remove the residual casting solvent.

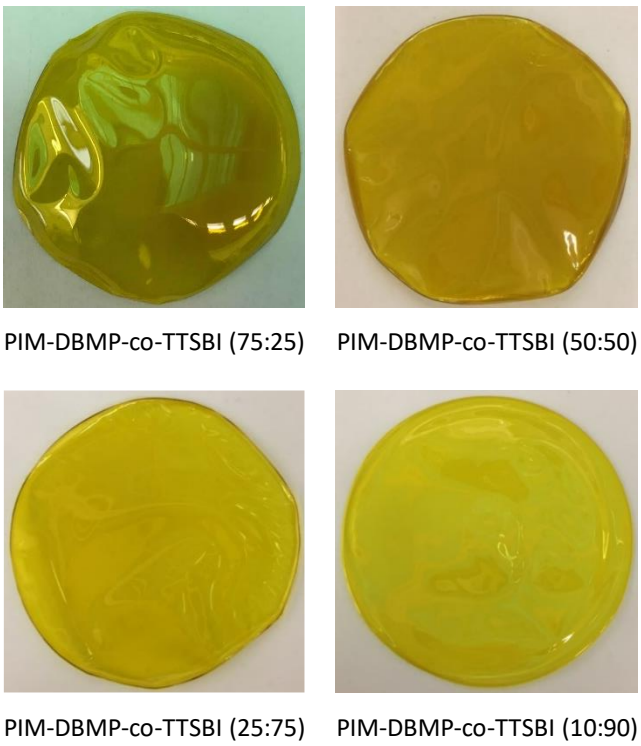

Figure 4.7 Photographs of the copolymer PIM-DBMP-co-TTSBI (m:n) membranes.

The single gas permeabilities were measured on these freshly methanol-treated membranes with similar thickness (100-130 μm) for N_2, O_2, CO_2, CH_4, H_2 and He. The gas permeability coefficients (P_X), ideal gas selectivities ($\alpha_{x/y}$) and film thickness (L) were summarized in **Table 4.2**. The gas permeability order for copolymers is $CO_2 > H_2 > O_2 >$He $> CH_4 > N_2$, which is the

same as that for PIM-1. Except for PIM-DBMP-*co*-TTSBI (10:90), its CH_4 permeability is higher than He due to the relatively larger improvement of CH_4 diffusivity coefficient relative to He (**Table 4.3**). This indicates that the inclusion of 10% DBMP weakens the size-sieving property which prefers to transport small gases. This may be related to the broad pore-size distribution of PIM-DBMP-*co*-TTSBI (10:90) in the ultramicroporous region (0.3-0.4 nm, size-sieving region) (**Figure 4.6c**). The low gas selectivity makes its gas permeability data located below the 1991 Roberson upper bounds for O_2/N_2 and H_2/N_2 (**Figure 4.9**). The separation of CO_2/CH_4 and CO_2/N_2 is mainly determined by the solubility selectivity, so the data of PIM-DBMP-*co*-TTSBI (10:90) locate near the 2008 upper bounds for these two gas pairs (**Figure 4.9**).

Table 4.2 Membrane Thickness (μm), ideal gas permeabilities (P_X, Barrer) and selectivities ($\alpha_{X/Y}$) of freshly methanol treated films measured at 25 ˚C and 1 bar of feed pressure.

PIM-	Thickness (μm)	P_{N_2}	P_{O_2}	P_{CO_2}	P_{CH_4}	P_{H_2}	P_{He}	α_{CO_2/CH_4}	α_{CO_2/N_2}	α_{O_2/N_2}	α_{H_2/N_2}
PIM-1	128	823	2270	13600	1360	5010	1950	10.0	16.5	2.8	6.1
DBMP-*co*-TTSBI (10:90)	102	1621	3355	21013	3326	6037	2344	6.3	13.0	2.1	3.7
DBMP-*co*-TTSBI (25:75)	121	1286	3722	21801	2076	7599	2736	10.5	17.0	2.9	5.9
DBMP-*co*-TTSBI (50:50)	125	1213	4081	22526	1843	8973	3148	12.2	18.6	3.4	7.4
DBMP-*co*-TTSBI (75:25)	110	973	3587	19646	1710	9060	3193	11.5	20.2	3.7	9.3
DBMP-*co*-TTSBI (75:25)	40	394	1933	9300	500	7212	2786	18.6	23.6	4.9	18.3
(215)[a]	40	109	679	3121	122	4211	1931	25.7	28.6	6.2	38.5

[a] Number in parenthesis is the ageing days after methanol treatment.

Table 4.3 Membrane Thickness (μm), diffusivity coefficients (D_x, 10^{-12} m^2 /s) and diffusivity selectivities (D_X/D_Y) of freshly methanol treated films measured at 25 ˚C and 1 bar of feed pressure.

PIM-	Thickness (μm)	D_{N_2}	D_{O_2}	D_{CO_2}	D_{CH_4}	D_{H_2}	D_{He}	D_{CO_2}/D_{CH_4}	D_{CO_2}/D_{N_2}	D_{O_2}/D_{N_2}	D_{H_2}/D_{N_2}
PIM-1	128	186	512	226	79	4200	5500	2.86	1.22	2.75	22.58
DBMP-*co*-TTSBI (10:90)	102	382	728	324	195	5762	6593	1.66	0.85	1.91	15.08
DBMP-*co*-TTSBI (25:75)	121	269	698	294	114	8511	9652	2.58	1.10	2.60	31.69
DBMP-*co*-TTSBI (50:50)	125	235	685	270	93	8671	10358	2.91	1.15	2.91	36.90
DBMP-*co*-TTSBI (75:25)	110	160	542	219	59	6978	9234	3.72	1.37	3.39	43.61
DBMP-*co*-TTSBI (75:25)	40	63	305	90	19	2060	2104	4.74	1.44	4.84	33.40
(215)[a]	40	18	107	34	4.7	1897	1980	7.23	1.89	5.94	105.39

[a] Number in parenthesis is the ageing days after methanol treatment.

Table 4.4 Membrane Thickness (μm), solubility coefficients (S_X, cm^3_{STP} cm^{-3} bar^{-1}) and solubility selectivities (S_X/S_Y) of freshly methanol treated films measured at 25 ˚C and 1 bar of feed pressure.

PIM-	Thickness (μm)	S_{N_2}	S_{O_2}	S_{CO_2}	S_{CH_4}	S_{H_2}	S_{He}	S_{CO_2}/S_{CH_4}	S_{CO_2}/S_{N_2}	S_{O_2}/S_{N_2}	S_{H_2}/S_{N_2}
PIM-1	128	3.3	3.3	45.1	12.9	0.9	0.3	3.50	13.60	1.00	0.27
DBMP-*co*-TTSBI (10:90)	102	3.2	3.5	48.6	12.8	0.8	0.3	3.81	15.26	1.09	0.25
DBMP-*co*-TTSBI (25:75)	121	3.6	4.0	55.6	13.7	0.7	0.2	4.07	15.49	1.11	0.19
DBMP-*co*-TTSBI (50:50)	125	3.9	4.5	62.7	14.9	0.8	0.2	4.20	16.20	1.15	0.21
DBMP-*co*-TTSBI (75:25)	110	4.6	5.0	67.4	21.8	1.0	0.3	3.09	14.77	1.09	0.22
DBMP-*co*-TTSBI (75:25)	40	4.7	4.8	77.7	19.7	2.6	1.0	3.94	16.53	1.02	0.55
(215)[a]	40	4.7	4.8	68.2	19.3	1.7	0.7	3.53	14.51	1.02	0.36

[a] Number in parenthesis is the ageing days after methanol treatment.

The gas permeabilities of all the copolymers are higher than those of PIM-1 for all gases with different increased extent depending on the gas molecular size. The diffusivity coefficients, solubility coefficients, diffusivity selectivities and solubility selectivities for copolymers and PIM-1 are listed in **Table 4.3** and **Table 4.4** to show the effect of DBMP molecules on the gas transport properties. The gas diffusivity coefficients of small gases (H_2 and He) are enhanced with increasing DBMP proportions, whereas larger gases (N_2, O_2, CO_2 and CH_4) experienced a downtrend. This is consistent with the microporous analysis that the introduction of DBMP generate more ultramicropores which is permeable to small gases, as demonstrated by the increased CO_2 adsorption for copolymers (**Figure 4.6b**). On the other hand, the promoted chain rigidity limits the motion of polymer segments which can open ultramicropores to enable large gas diffusion, so the diffusivity coefficients of large gases were decreased.[177, 178]. As a result, the diffusivity selectivity of small gases over large gases is improved by increasing DBMP contents, as illustrated by the correlation between the diffusivity coefficients and the square of gas kinetic diameter (**Figure 4.8**). The solubility coefficients for all gases increase with increasing DBMP contents, which may be also resulted from the enhanced contents of ultramicropores. The solubility selectivity shows small variations as the monomer compositions change (**Table 4.4**). Both of the increased diffusivity coefficients and solubility coefficients for H_2 and He lead to significant increases (by around 80%) in their gas permeabilities, with DBMP contents increasing from 10% to 75%. The gas permeabilities of O_2 and CO_2 remain stable when DBMP contents increase. In contrast, the gas permeabilities of N_2 and CH_4 decrease by 40% due to the significantly reduced diffusivity coefficients when the DBMP proportion increases from 10% to 75%.

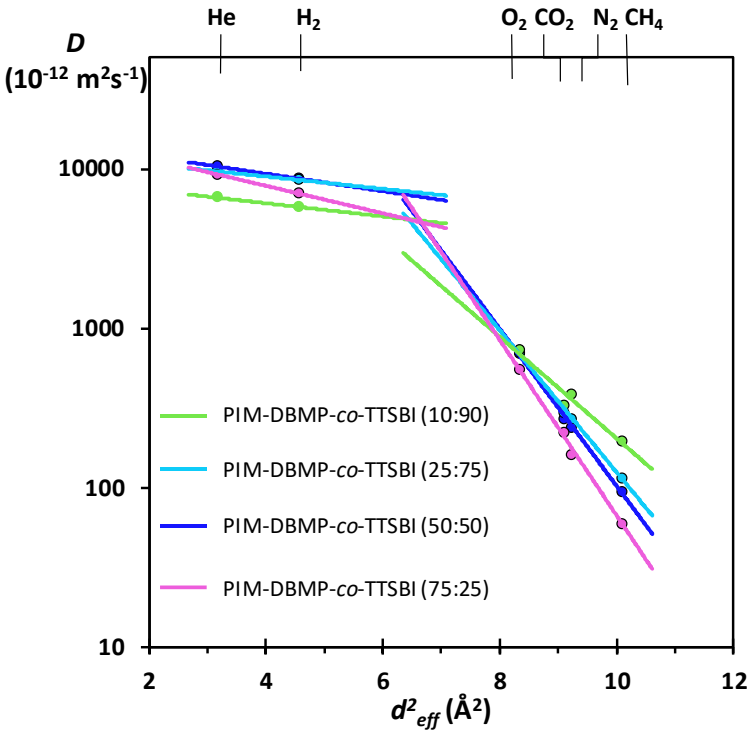

Figure 4.8 Correlation of diffusivity coefficient (D_x) with the squared effective gas diameter (d^2_{eff}) (He = 1.78, H_2 = 2.14, O_2 = 2.89, CO_2 = 3.02, N_2 = 3.04, CH_4 = 3.18 Å).

As expected, the gas selectivities show a growth with increasing DBMP proportion due to the improved diffusivity selectivity. When the DBMP contents are higher than 25%, copolymers exhibit both higher gas permeabilities and selectivities than PIM-1. Therefore, their gas permeability data are all located above the 2008 upper bounds for CO_2/CH_4, CO_2/N_2, O_2/N_2 and H_2/N_2 (**Figure 4.9**). The gas permeability and selectivity of copolymers increase together by increasing DBMP contents, so their gas permeability data shift towards the up-right corner on the upper bound plot, overcoming the challenged permeability/selectivity trade-off relationship. In particular, PIM-DBMP-*co*-TTSBI (75:25) is close to the newly defined 2019 CO_2/N_2 upper bound with the CO_2 permeability of 19646 Barrer and selectivity of 20.2. The separation performance for O_2/N_2 and H_2 including gas pairs are also improved significantly after the introduction of DBMP units. As exemplified for H_2/N_2 separation, the H_2 permeability increases from 5010 Barrer of PIM-1 to 9060 Barrer of PIM-DBMP-*co*-TTSBI (75:25) (by about 80%), and importantly the selectivity is also improved by about 50% (6.1 to 9.3).

To obtain high permeation rates in practical applications, the gas separation membrane is thin and supported on a porous substrate. The gas permeability of a thin film for PIM-DBMP-*co*-TTSBI (75:25) (40 μm) was measured and positioned on the Robeson plots. The thinner film possesses higher selectivities with lower permeabilities as compared to the thick film due to the accelerated physical aging of thin films.[31, 179-181] Upon aging, larger voids collapse preferentially leading to a reduction in large gas permeability (CO_2, N_2 and CH_4) as compared to that of small gases (H_2, He and O_2) coupled with a significantly increased gas selectivity. For example, the H_2 permeability of the thin film is 7212 Barrer (20% reduction), while the gas selectivity of H_2/N_2 increases from 9.3 to 18.3 by 50%. Extended aging studies were carried out on the thin film of PIM-DBMP-*co*-TTSBI (75:25) (40 μm), exhibiting permeability loss and concomitant selectivity gain over aging. After 200 days aged, the H_2 permeability exceeds CO_2, which is unusual for PIMs, indicating an improved size selectivity. Favourably, aged PIM-DBMP-*co*-TTSBI (75:25) (40 μm) exhibits a balanced combination of permeability and selectivity, so its data locate on or above the 2015 upper bounds for O_2/N_2 and H_2/N_2. For example, aged PIM-DBMP-*co*-TTSBI (75:25) (40 μm) demonstrates high H_2 permeability (PH_2 = 4211 Barrer) which is as permeable as the freshly methanol treated PIM-1 (PH_2 = 4711 Barrer, $\alpha H_2/N_2$=6.1), along with extraordinary H_2/N_2 selectivity (39, about 6 times higher than PIM-1). The exceptional gas separation performance of PIM-DBMP-*co*-TTSBI (75:25) demonstrate its potential use as separation membranes for hydrogen separations.

There were many studies utilizing copolymerisation to design more advanced microporous materials. However, the reported copolymers usually exhibit an increase in the selectivity while a reduction in the permeability relative to the homopolymer.[162, 182-189] In contrast, the DBMP motifs in our study simultaneously improve the polymer chain rigidity and the quantity of ultramicropores, leading to an improvement in both the gas permeability *and* selectivity. The extraordinary improvement may be related to the unique structure of DBMP contributing to the formation of 2D ribbon-like polymer chains with high rigidity which tend to generate more connected ultramicropores as compared to the 3D PIMs with irregular contortions.

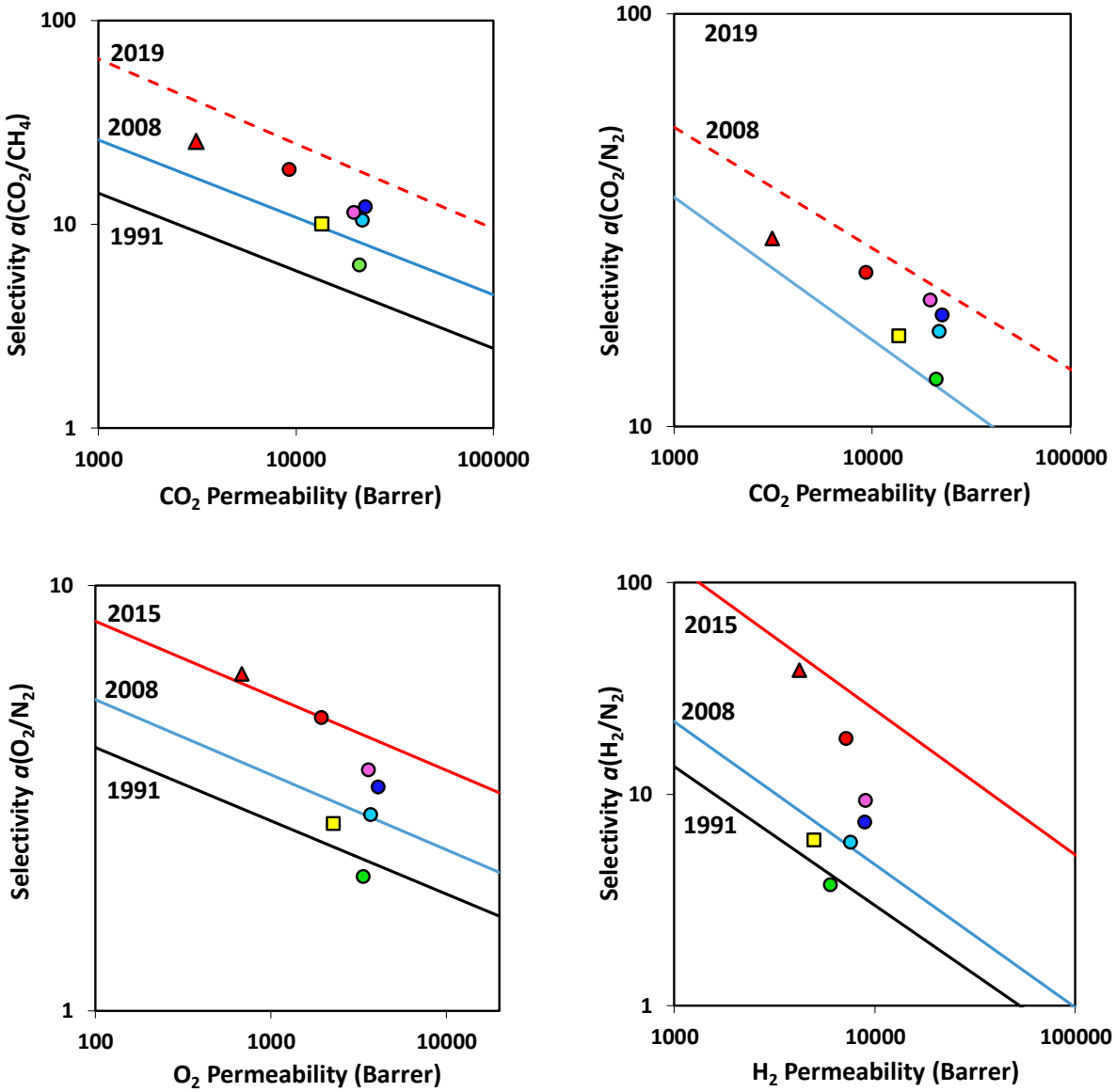

Figure 4.9 Robeson plots for the (a) CO_2/CH_4, (b) CO_2/N_2, (c) O_2/N_2, (d) H_2/CO_2 (e) H_2/N_2 and (f) H_2/CH_4 gas pairs showing the position of the fresh films of PIM-1 (128 µm □), PIM-DBMP-*co*-TTSBI (10:90) (●), PIM-DBMP-*co*-TTSBI (25:75) (●), PIM-DBMP-*co*-TTSBI (50:50) (●) and PIM-DBMP-*co*-TTSBI (75:25) (110 µm ●, 40 µm ●), 215 days aged PIM-DBMP-*co*-TTSBI (75:25) (40 µm ▲).

4.2 Amidoxime modified PIMs-DBMP

4.2.1 Introduction

The work of copolymers based on DBMP proves that DBMP is a promising building unit for separation membranes. The homopolymer PIM-DBMP may an even better combination of gas permeability and selectivity due to its 2D polymer chains which has been shown to be favourable in the previous two chapters.[128] Unfortunately, the homopolymer PIM-DBMP could not be cast into a flexible membrane. However, it was thought that post-polymerization modification at the nitrile groups which can increase the inter-chain interactions via the formation of charge-transfer complexes (CTCs) or hydrogen-bonding network maybe a means to improve the solubility for casting and mechanical property of resulting films.

In 2012, Patel and Yavuz reported a non-invasive post-polymerisation modification of PIMs using amidoxime functionalization. This modification can be achieved by a rapid reaction of the nitriles with hydroxylamine under reflux conditions.[43, 190, 191] The non-invasive effort of this modification means that it only causes a minor adverse effect on the physicochemical properties of polymers. For example, AO-PIM-1 still possesses good solution processability, although it became soluble in polar aprotic solvents (e.g., DMSO).[43, 192] AO-PIM-1 still shows high BET surface area of 482 $m^2 g^{-1}$,[43] which was among the highest ever reported for the various post modified PIM-1 materials (e.g. 263 $m^2 g^{-1}$ for thioamide PIM-1).[40, 157, 158, 163, 193-195] In addition, AO-PIM-1 demonstrated exceptional gas separation performance in a ternary feed mixture ($H_2S/CO_2/CH_4$) separation under aggressively high pressures of up to 77 bar.[191] This exceptional performance is due to the formation of cross-linked structures by hydrogen bonds which enhance its plasticization resistance. Inspired by this work, [43, 191] the amidoxime modification was applied to PIMs-DBMP, which is anticipated to get excellent membranes with good mechanical property and extraordinary gas separation performance.

4.2.2 Synthesis of amidoxime modified PIMs-DBMP (AO-PIMs-DBMP)

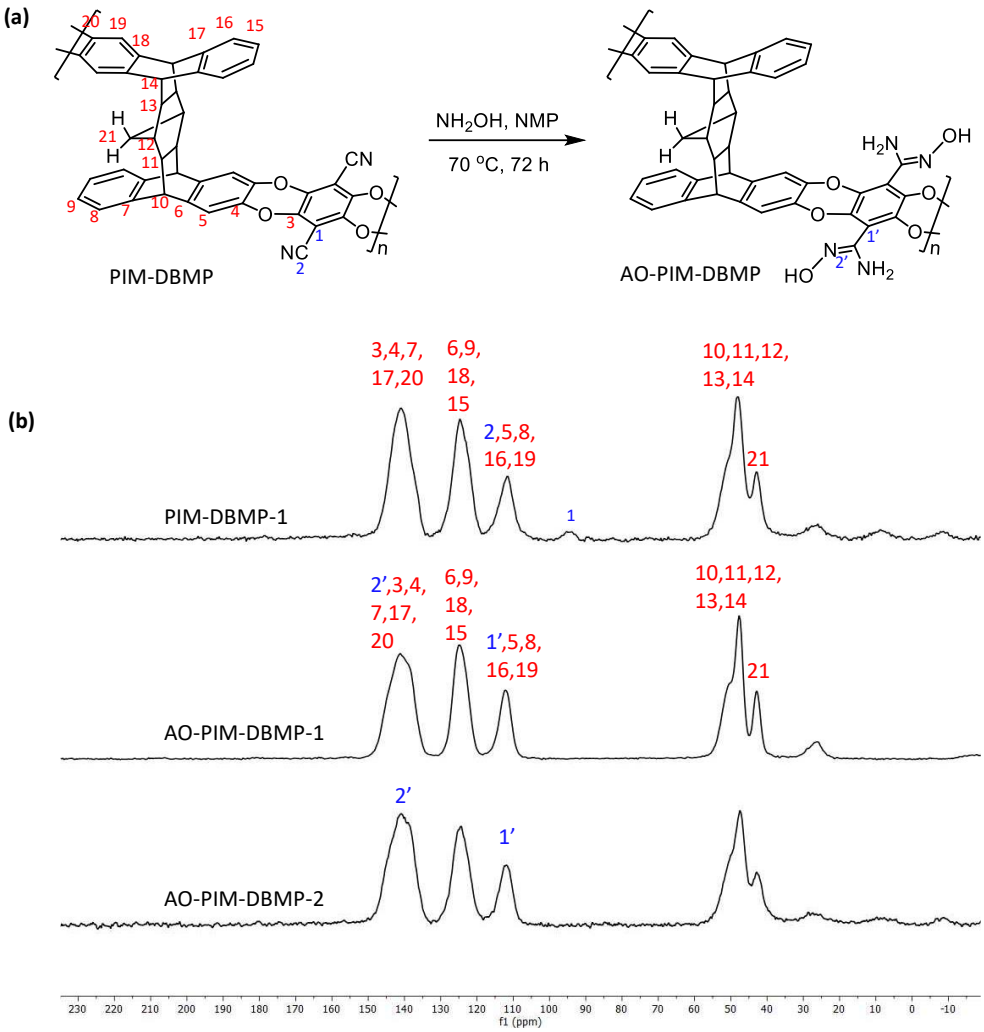

Figure 4.10 (a) Post-synthesis modification of PIM-DBMP to afford AO-PIM-DBMP. (b) Solid state ^{13}C NMR of PIM-DBMP-1 and AO-PIMs-DBMP.

The amidoxime modification of PIM-DBMP (AO-PIM-DBMP) was carried out according to the procedure reported by Patel *et al*.[190] PIM-DBMP was reacted with hydroxylamine in NMP at 70 ˚C (**Figure 4.10a**). After completion of the reaction, the colour of the polymers was observed to be notably changed from fluorescent yellow to off-white. The complete conversion of nitrile to amidoxime moiety was confirmed by solid state ^{13}C NMR and FTIR spectroscopy. After modification, the signal of the aromatic carbons connected to the nitriles (marked as 1) shifted from 94 ppm in PIM-DBMP to 111 ppm in AO-PIM-DBMP (**Figure 4.10b**). Mason *et al*. also observed a similar chemical shift change of this carbon in the amine

modified PIM-1.[158] The chemical shift of nitriles (marked as 2) shifted towards a downfield position (marked as 2') after being transformed to amidoximes, which overlaps with the peak of the aromatic carbon (**Figure 4.10b**). The successful formation of amidoxime groups was further confirmed by the FTIR spectra shown in **Figure 4.11a**. The characteristic stretching band of nitriles at 2239 cm^{-1} completely disappears in the AO-PIM-DBMP-1 spectrum along with the appearance of three new broad bands at 3476 cm^{-1}, 3358 cm^{-1} and 3356 cm^{-1} corresponding to the stretching vibrations of NH_2 and OH. The bands at 1647 and 935 cm^{-1} are assigned to the stretching vibrations of C=N and N-O bonds in amidoxime groups. These findings confirmed the full conversion of nitriles to amidoximes. TGA analysis of AO-PIM-DBMP-1 shows a weight loss of 6.5 % in the range of 200-325 ˚C, which is similar to AO-PIM-1[190] (**Figure 4.11b**). This is attributed to the thermal decomposition of the amidoxime group which leads to a loss of hydroxylamine. This weight loss is comparable with the theoretical weight loss value (4.7%) of the hydroxylamine in the completely converted AO-PIM-DBMP-1.

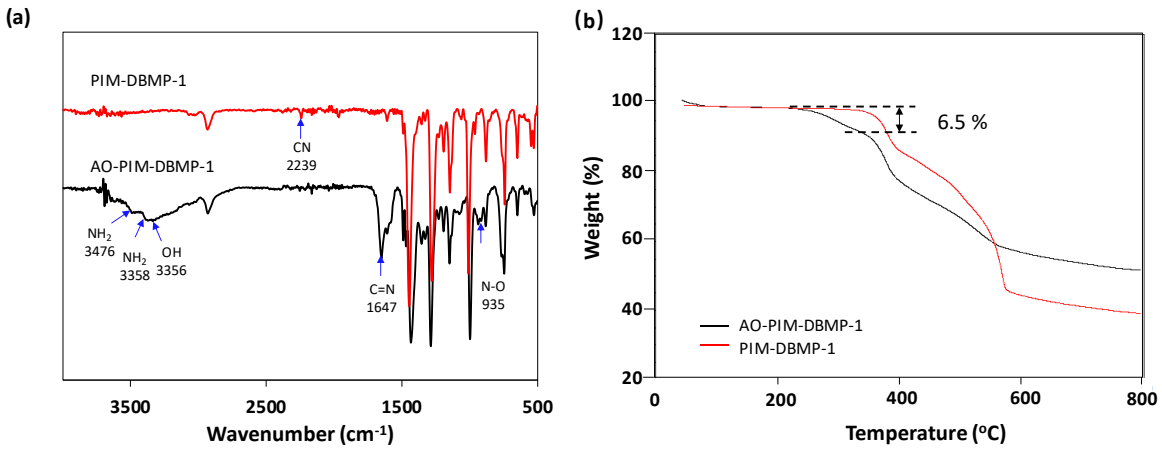

Figure 4.11 (a) FTIR spectra and (b) TGA spectra of PIM-DBMP-1 and AO-PIM-DBMP-1.

4.2.3 Microstructure analysis and Gas transport property

AO-PIMs-DBMP show good solubility in polar aprotic solvent NMP. Hence, free-standing films of AO-PIMs-DBMP were prepared by casting from NMP solutions. The film of AO-PIM-DBMP-1 based on the 'trans-like' DBMP monomers exhibited good mechanical property (**Figure 4.12a**), while the film of AO-PIM-DBMP-2 based on the 'cis-like' DBMP monomer broke during casting. The internal network of hydrogen bonding in AO-PIMs-DBMP enhanced the inter-chain interactions and thus improved the mechanical property of films. For AO-PIM-

DBMP-2, the major components are cyclic oligomers as discussed above, which cannot provide enough polymer chain entanglement, even with the introduction of the hydrogen-bonding network.

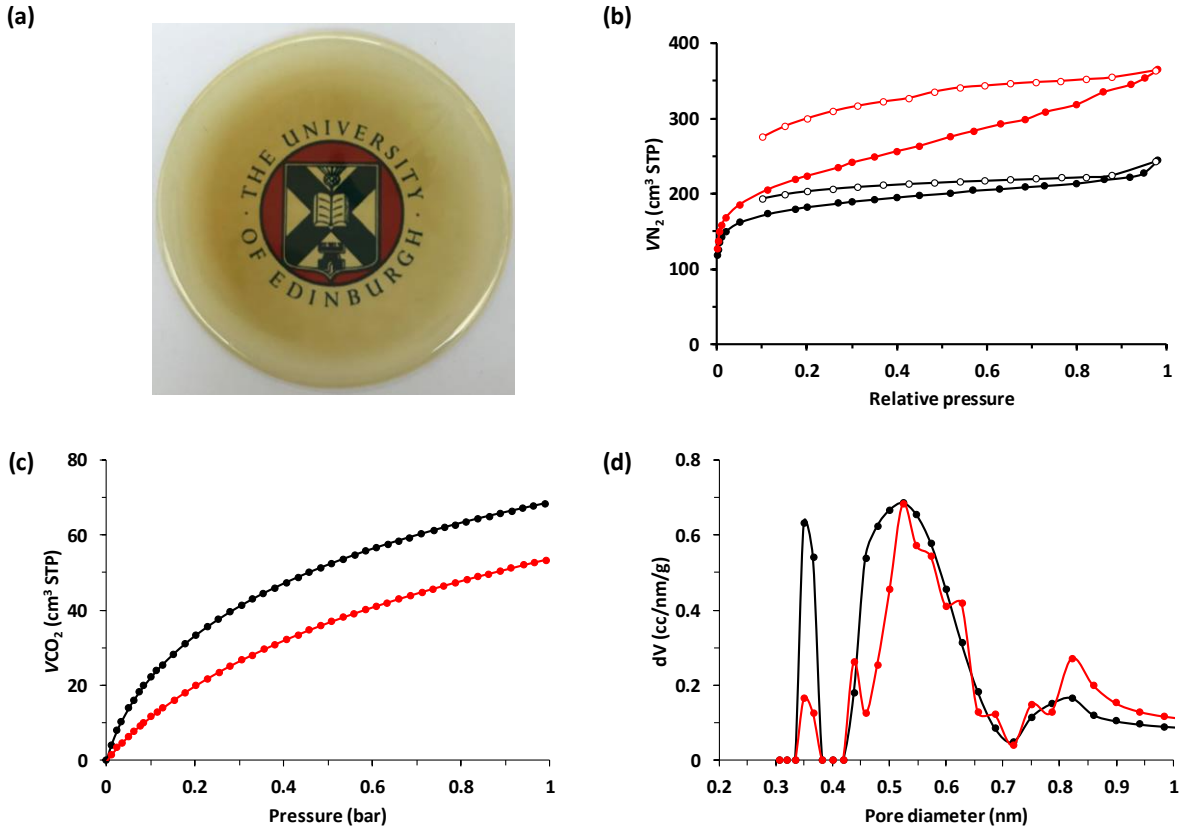

Figure 4.12 (a) Solvent cast free-standing film of AO-PIM-DBMP-1; (b) Nitrogen adsorption (solid circle) and desorption (open circle) isotherms at 77 K for powdered samples; (c) Carbon dioxide adsorption isotherms at 273 K for powdered samples; (d) Pore size distribution (PSD) calculated from CO_2 adsorption data using non-local density functional theory (NLDFT) model based on carbon slit-pore geometry; AO-PIM-DBMP-1 (●), PIM-DBMP-1 (●).

The microstructure of AO-PIM-DBMP-1 was investigated by physisorption and pore-size distribution (PSD) analyses using polymer powder. AO-PIM-DBMP-1 shows a typical type I nitrogen adsorption isotherm, indicating a microporous structure (**Figure 4.12b**). The N_2 uptake of AO-PIM-DBMP-1 is lower than that of PIM-DBMP-1 over the whole measured pressure range (**Figure 4.12b**), thereby, AO-PIM-DBMP-1 possesses a lower BET surface area of 645 m^2/g than PIM-DBMP of 790 m^2/g (82% surface area maintained, **Table 4.5**). AO-PIM-DBMP-1 also undergoes a reduction in total pore volume from 0.73 mL/g to 0.38 mL/g (**Table**

4.5). The reduced BET surface area and total free volume reflect a tightened microstructure as a result of the extensive hydrogen bonding formed between amidoxime groups. Upon N_2 desorption, a low hysteresis was observed for AO-PIM-DBMP-1 relative to the pronounced hysteresis for the parent PIM-DBMP-1 (**Figure 4.12b**). The hysteresis of desorption in PIMs was interpreted as a consequence of the swelling/trapping effect of non-network materials.[196, 197] The abundant inter- and intra-chain hydrogen bonding in AO-PIM-DBMP-1 can suppress the sorption-induced polymer swelling, leading to a low hysteresis. The low hysteresis of AO-PIM-DBMP-1 also reflects it may have better plasticization resistance than PIM-DBMP-1, which is beneficial to the practical separations under aggressive mixed-gas conditions.

Table 4.5 Physical and gas adsorption properties of PIMs

Polymer	SA_{BET} [a] (m^2/g)	V_{total} [b] (ml/g)	CO_2 uptake [c] (mmol/g)	Solubility
PIM-DBMP-1	790	0.73	2.38	Quinoline
AO-PIM-DBMP-1	645	0.38	3.05	NMP
PIM-1[3]	768	0.70	_	$CHCl_3$, CH_2Cl_2
AO-PIM-1[3]	482	0.27	_	DMSO, DMF, NMP

[a] BET surface area (SA_{BET}) calculated from N_2 adsorption isotherm obtained at 77 K. [b] CO_2 uptakes at 1 bar/273 K. [c] Total free volume (V_{Total}) estimated from N_2 adsorption at P/P_o = 0.98.

In contrast to the lower N_2 adsorption, AO-PIM-DBMP-1 displays higher CO_2 adsorption than PIM-DBMP-1 (**Figure 4.12c**). AO-PIM-DBMP-1 has a CO_2 capability of 3.05 mmol/g at 273 k at 1 bar, with 28% enhancement as compared to PIM-DBMP-1 of 2.38 mmol/g (**Table 4.5**). The enhanced CO_2 uptake was also observed for AO-PIM-1, which reflects the higher concentration of ultramicropores as compared to the parent PIMs. As demonstrated in the PSDs (**Figure 4.12d**), the amount of ultramicropores (< 0.7 nm) of AO-PIM-DBMP-1 shows a significant increase accompanied with a moderate decrease in the micropores (> 0.7 nm).

Unfortunately, as noted previously, a robust membrane of PIM-DBMP-1 for gas permeation measurements cannot be achieved, thereby the influence of amidoxime groups on gas separations cannot be evaluated directly by comparing their gas permeation values. According to the comparison of their microstructure, gas selectivity of AO-PIM-DBMP-1

should be higher than PIM-DBMP-1 coupled with a decreased gas permeability. For instance, the increase in CO_2 uptake coupled with a reduction in N_2 uptake suggests that AO-PIM-DBMP-1 exhibits higher selectivity for CO_2/N_2 gas pair. In addition, AO-PIM-DBMP-1 with reinforced structure shows less structural expansion and deformation than PIM-DBMP-1 when exposed to adsorbates as evidenced by the lower hysteresis in N_2 desorption isotherm of AO-PIM-DBMP-1. The gas selectivity of AO-PIM-DBMP-1 is anticipated to be more stable in practical mixed-gas system, where the gas selectivity of PIM-DBMP-1 may have a drop due to the swelling of polymer matrix leading to increased permeabilities of larger gases.

In comparison with the AO-PIM-1 reported by Swaidan *et al.*,[43] AO-PIM-DBMP-1 displays both higher BET surface area and total free volume (**Table 4.5**). It is consistent with the results obtained previously for TTSBI-DBMP copolymers that the inclusion of DBMP improves the free volume. In addition, AO-DBMP-1 has higher backbone stiffness than AO-PIM-1, which can further improve size-sieving property. Single gas permeabilities were measured using freshly methanol-treated AO-PIM-DBMP-1. The gas permebilities and selectivities for AO-PIM-DBMP-1 and those reported for AO-PIM-1 are summarized in **Table 4.6**. The gas permeability order for AO-PIM-DBMP-1 was: $H_2 > CO_2 > CH_4 \approx N_2$. In the case of AO-PIM-1, the most permeable gas is CO_2 (**Table 4.6**), following the typical order of polybenzodioxine PIMs because of their high CO_2 solubility. However, the H_2 permeability is higher than CO_2 for AO-PIM-DBMP-1, demonstrating an improved size sieving which favours the transport of smaller gases. The improved size-sieving ability of AO-PIM-DBMP-1 may be a consequence of the synergic between high backbone rigidity and hydrogen-bonding networks.

Table 4.6 Single gas permeabilities (P_X, Barrer) and ideal selectivities ($\alpha_{X/Y}$) for AO-PIM-DBMP-1 and reported AO-PIM-1.

Polymer	P_{N_2}	P_{O_2}	P_{CO_2}	P_{CH_4}	P_{H_2}	α_{CO_2/CH_4}	α_{CO_2/N_2}	α_{O_2/N_2}	α_{H_2/CO_2}	α_{H_2/CH_4}	α_{H_2/N_2}
AO-PIM-DBMP-1[a]	106	691	3524	106	4526	33	35	6.5	1.3	42.7	42.5
AO-PIM-DBMP-1 (70)	84	561	2914	93	3807	31	35	6.7	1.3	41	45
AO-PIM-1[b]	33	147	1153	34	912	34	33	4.5	0.8	26.8	27.6

[a] T = 25 °C, 1 bar, 24 methanol soak and air-dried for 24 h.

[b] T = 35 °C, 2 bar, 24 methanol soak and dried under vacuum at 120 °C for 24 h.[43]
The number in the parentheses is physical aging days.

It should be noted that the reported gas permeability data of AO-PIM-1 (80-100 μm) was measured using a membrane dried under vacuum at 120 ˚C for 24 h.[43] In our method, the film of AO-PIM-DBMP-1 (≈ 90 μm) was dried at ambient temperature after methanol treatment before gas permeability test. It is well known that the permeability properties of membranes vary when utilising different treatments. The membranes experience accelerated physical aging at elevated temperatures leading to increases in gas selectivity accompanied with reductions in gas permeability. Although it is less relevant to compare the gas permeability data of AO-PIM-DBMP-1 and the reported data of AO-PIM-1, it provides some important information via comparing their gas selectivity.

As expected, the gas selectivities of AO-PIM-DBMP-1 are higher than those of AO-PIM-1 due to the enhanced size-sieving property (**Table 4.6**). The significantly enhanced diffusivity selectivities (**Table 4.7**) of AO-PIM-DBMP-1 improved gas selectivities by about 60% for O_2/N_2, H_2/CH_4, H_2/N_2 and H_2/CO_2, as compared to AO-PIM-1. The exceptional gas selectivity combined with high permeability placed AO-PIM-DBMP-1 data above the 2015 upper bounds for H_2/CH_4, H_2/N_2 and O_2/N_2, where those for AO-PIM-1 are located near the 2008 upper bounds (**Figure 4.13**). In particular, AO-PIM-DBMP-1 shows outstanding separation performance for H_2 including gas pairs with H_2 permeability of 4526 Barrer and H_2/CH_4 selectivity of 42.7 (one of the best among PIMs to date).

Table 4.7 Diffusivity coefficients (D_X, 10^{-12} m^2 /s) and diffusivity selectivities (D_X/D_Y) for AO-PIM-DBMP-1 and reported AO-PIM-1

Polymer	D_{N_2}	D_{O_2}	D_{CO_2}	D_{CH_4}	D_{H_2}	D_{CO_2}/D_{CH_4}	D_{CO_2}/D_{N_2}	D_{O_2}/D_{N_2}	D_{H_2}/D_{CO_2}	D_{H_2}/D_{CH_4}	D_{H_2}/D_{N_2}
AO-PIM-DBMP-1[a]	19.5	126	35.4	4.1	5232	8.6	1.8	6.5	148	1276	269
AO-PIM-DBMP-1 (70)	15.0	95.4	26.6	3.8	4840	7.0	1.8	6.4	182	1274	322
AO-PIM-1[b]	9.9	40.6	24.6	2.6	-	9.5	2.5	4.1	-	-	-

[a] T = 25 °C, 1 bar, 24 methanol soak and air-dried for 24 h.
[b] T = 35 °C, 2 bar, 24 methanol soak and dried under vacuum at 120 °C for 24 h.[43]
The number in the parentheses is physical aging days.

Table 4.8 Solubility coefficients (S_X, cm^3_{STP} cm^{-3} bar^{-1}) and solubility selectivities (S_X/S_Y) for AO-PIM-DBMP-1 and reported AO-PIM-1

Polymer	S_{N_2}	S_{O_2}	S_{CO_2}	S_{CH_4}	S_{H_2}	S_{CO_2}/S_{CH_4}	S_{CO_2}/S_{N_2}	S_{O_2}/S_{N_2}	S_{H_2}/S_{CO_2}	S_{H_2}/S_{CH_4}	S_{H_2}/S_{N_2}
AO-PIM-DBMP-1[a]	4.1	4.1	74.7	19.4	0.7	3.8	18.2	1.0	0.01	0.04	0.16
AO-PIM-DBMP-1 (70)	4.2	4.4	82.3	18.3	0.6	4.5	19.6	1.1	0.01	0.05	0.14
AO-PIM-1[b]	3.3	3.6	46.8	13.0	-	3.6	14.2	1.1	-	-	-

[a] T = 25 °C, 1 bar, 24 methanol soak and air-dried for 24 h.

[b] T = 35 °C, 2 bar, 24 methanol soak and dried under vacuum at 120 °C for 24 h.[43]

The number in the parentheses is physical aging days.

For CO_2/N_2 and CO_2/CH_4, AO-PIM-DBMP-1 possessed similar gas selectivities to AO-PIM-1, while with a better overall gas separation performance (P_{CO_2} = 3524 Barrer, α_{CO_2/N_2} = 35, α_{CO_2/CH_4} = 33). Therefore, its gas permeability points lie on the latest 2019 upper bounds for these two gas pairs (**Figure 4.13**), whereas AO-PIM-1 locates on the 2018 upper bounds. The great size-sieving property of AO-PIM-DBMP-1 with high gas permeability makes it a potential material for applications in challenging tasks, such as, oxygen and nitrogen enrichment (O_2/N_2), efficient hydrogen recovery in ammonia production (H_2/N_2), petrochemistry (H_2/CH_4) and precombustion carbon capture (H_2/CO_2).

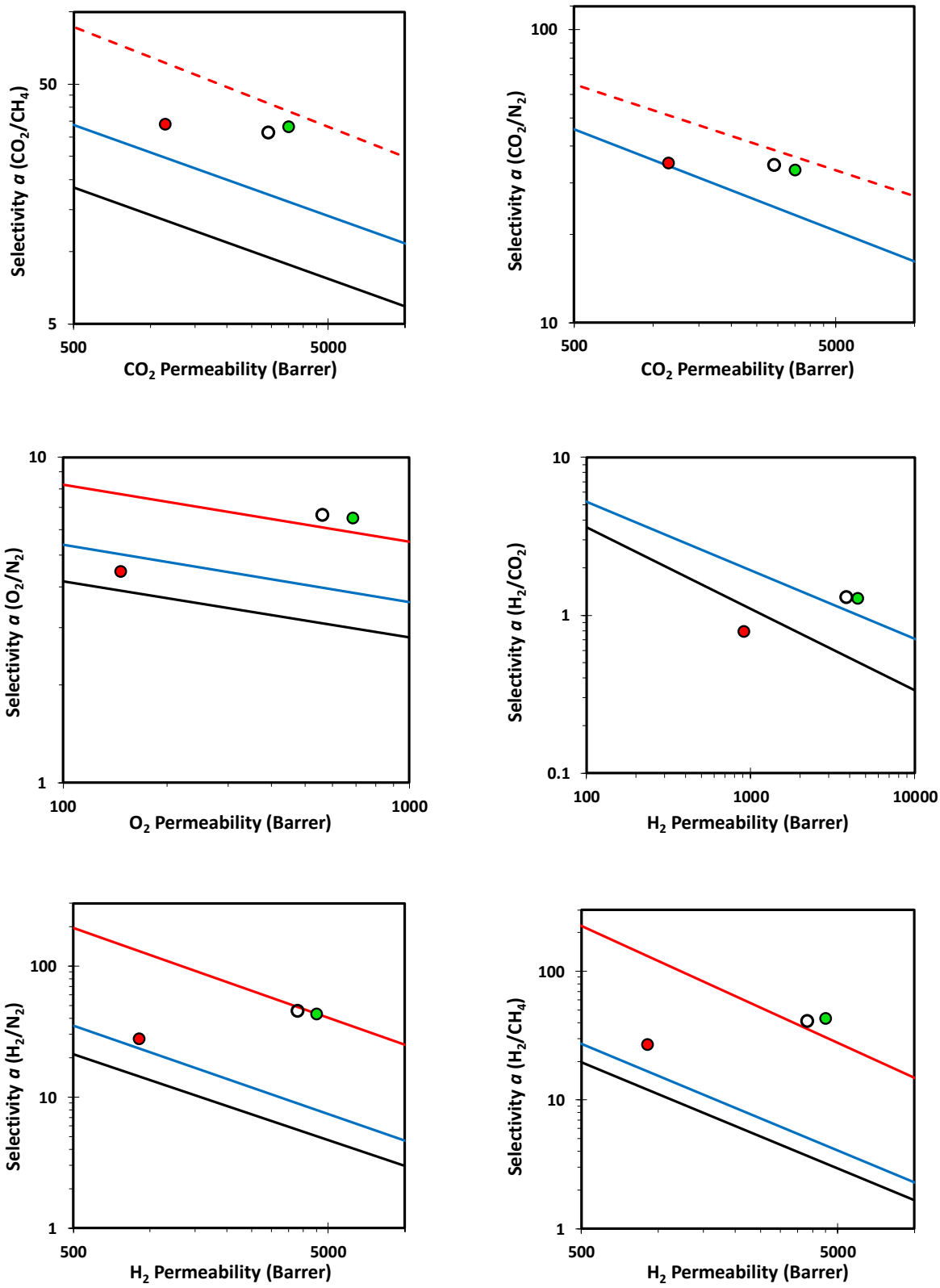

Figure 4.13 Robeson plots for the CO_2/CH_4, CO_2/N_2, O_2/N_2, H_2/CO_2, H_2/CH_4 and H_2/N_2 gas pairs showing the positions of AO-PIM-DBMP-1 film (fresh ●, 70 days aged ○) and AO-PIM-1 film[43] (●). The black

and blue lines represent the 1991 and 2008 upper bounds, and the red solid lines are the proposed 2015 upper bound for O_2/N_2, H_2/CH_4 and H_2/N_2. The dashed lines are the revised upper bounds for CO_2/CH_4 and CO_2/N_2 based on the benzotriptycene PIMs.

Physical aging studies was carried out for AO-PIM-DBMP-1. Surprisingly, AO-PIM-DBMP-1 showed good physical aging resistance losing only about 20%-10% of gas permeability over 70 days. This good anti-aging ability of AO-PIM-DBMP-1 may be a result of the synergy between the both high intrachain and interchain rigidity. It is worth noting that the largest gas CH_4 was the least influenced over aging with only 12% decrease in permeability, whereas N_2 lost the most permeability of 21%. It reflects that the physical aging mainly causes a collapse of pores with similar or smaller than N_2 diameter. Therefore, the selectivities of CO_2/CH_4 and H_2/CH_4 showed a little decrease at 70 days due to the significantly decreased permeabilities of smaller gases compared to CH_4. The gas selectivities of other gas pairs underwent an increase following the tradeoff relation, so they are still located near the latest upper bounds after aging (**Figure 4.13**). The permeability of AO-PIM-DBMP-1 over an extending period will continue to be tracked to investigate the stability of its permeation properties.

As demonstrated, DBMP is an excellent building block for microporous materials which can simultaneously improve the rigidity and ultramicropores of polymers and thus leads to both high gas permeability and selectivity. In addition, the both high intrachain and interchain rigidity provides AO-PIM-DBMP-1 with extraordinary gas selectivity and good stability.

Chapter 5 Conclusions

This thesis describes a series of new polymers of intrinsic microporosity (PIMs) for gas separation which were designed in two aspects to tune the pore contents, pore size distributions and chemical property: (1) the introduction of fluorine-containing groups; (2) the introduction of the new building unit dibenzomethanopentacene (DBMP).

In the second chapter, CF_3 substituted benzotriptycene-based PIMs (PIM-TFM-BTrip containing one CF_3 group on each repeating unit and PIM-DTFM-BTrip containing two CF_3 on each repeating unit) were achieved. Their gas transport results demonstrated that the bulky CF_3 group is an efficient interchain spacer, making PIM-DTFM-BTrip the most permeable polymer among all benzotriptycene-based PIMs. Importantly, CF_3 groups improved the solubility selectivities of CO_2/CH_4 and N_2/CH_4 for PIM-TFM-BTrip, arising from the low sorption of CH_4 as compared to PIM-BTrip (with no substituent). As a result, PIM-TFM-BTrip displayed both higher permeabilities and selectivities for CO_2/CH_4 and N_2/CH_4 than PIM-BTrip. In addition, the outstanding performance of the 2D benzotriptycene-based PIMs redefined the new 2019 upper bounds for CO_2/CH_4 and CO_2/N_2.

Following the abovementioned work, fluorinated benzomethanoanthracene based polymers with an improved fluorine density were prepared. These polymers can be achieved by fewer steps than the previous fluorinated benzotriptycene PIMs. The analysis of polymer microstructure and membrane gas adsorption illustrate the CH_4-phobic property of PIM-OCF with comparison to the nonfluorinated PIM-OCP. The perfluoroalkyl chain substituent was also observed to reduce the CH_4 sorption and thus improve the solubility selectivities of CO_2/CH_4 and He/CH_4 for PIM-C8F17. However, the reduced size selectivity of PIM-C8F17 and the extremely low surface area of PIM-C8F17-TB made them behave worse than the previously reported PIMs. These results demonstrated that the introduction of fluorines to PIMs reduced the adsorption of hydrocarbon molecules and thus created an effective way to tune the solubility selectivity. This result encouraged us to explore the plasticization resistant ability of these fluorinated PIMs under mixed gas conditions.

In the last chapter, DBMP was utilized to construct a new 2D PIM. Unfortunately, the PIM-DBMP homopolymer cannot be cast into a freestanding film. However, a series of DBMP copolymers with 10%, 25%, 50% and 75% proportions were synthesized. Analysis of their gas transport properties demonstrate that DBMP is an excellent building block for microporous materials which can simultaneously improve the rigidity and ultramicroporosities of polymers leading to both high gas permeability and selectivity. In addition, the amidoxime modification of PIM-DBMP (AO-PIM-DBMP) promoted the membrane forming ability of the polymer and afforded a robust film successfully. The resulting AO-PIM-DBMP exhibits an extraordinary gas separation performance which locates on the latest upper bounds for CO_2/CH_4, CO_2/N_2, O_2/N_2 and H_2/CO_2.

At last, physical aging studies for these new PIMs based on benzotriptycene and DBMP suggest the larger pores prefer to collapse over time (same as most PIM) leading to improved size selectivity properties. As a result, the aged PIMs showed better separation performances after aging for O_2/N_2 and H_2/N_2 pairs due to the significantly improved selectivity as compared to the fresh membranes.

Chapter 6 Future work

The gas permeability will be measured for PIM-OCP and PIM-OCF films. These two polymers possess high surface areas of 928 and 1062 m^2/g which are similar to the benzotriptycene-based PIMs (848 – 1034 m^2/g). Therefore, they are supposed to be as permeable as benzotriptycene-PIMs with high selectivity due to their high polymer chain rigidity. As demonstrated by molecular simulation, PIM-OCF and PIM-OCP have similar chain packing, so they may have similar diffusivity selectivity. The membrane gas sorption results demonstrate a lower CH_4 sorption of PIM-OCF, resulting in an improved CO_2/CH_4 selectivity as compared with PIM-OCP. Therefore, PIM-OCF is supposed to provide better gas selectivities for light gases over CH_4 (i.e., CO_2/CH_4, H_2/CH_4, He/CH_4 and N_2/CH_4) than PIM-OCP, due to its better solubility selectivities for light gases over CH_4.

Physical aging behaviour of these fluorinated polymers will be investigated in the future. Reported work demonstrated that glassy perfluoropolymers gave a more stable separation performance than other high-free-volume polymers.[180] The gas separation performances for these fluorinated polymers are attractive, especially for PIM-C8F17. The flexible perfluoroalkyl chain substituent may aggregate via relaxation over aging due to the low surface energy of fluorinated chains. Thus it may produce a phase separation on molecular scale between the fluorinated part and hydrocarbon part in the polymers which may improve its permeability stability over time.

The performance of these polymers under mixed-gas conditions will also be the subject of further studies. In comparison to the pure gas models, measurements under mixed-gas feeds can provide more relevant information about the potential of a new material in real separation systems. Generally, the gas selectivity of polymeric membranes decreases in the mixed-gas conditions, particularly gas mixtures containing highly condensable gases (e.g. CO_2/CH_4 and CO_2/N_2). This is because the highly condensable gases will cause polymer swelling and lead to increased adsorption sites for the other gas molecules. The fluorinated polymers synthesised in this thesis will be subjected to the mixed-gas permeability measurement. The low hydrocarbon sorption of the fluorinated polymers is anticipated to improve the plasticization resistance. Furthermore, the improved interchain interactions also contribute to an improved plasticization resistance. Reported data for AO-PIM-1 showed a

decrease in gas selectivity for the CO_2/CH_4 mixed-gas feed, but the decrease is less than PIM-1 due to the reinforced structure which limited the expansion of the polymer matrix.[43] In contrast, a thermally rearranged (TR) microporous polymers[198] and a post-synthesis modified PIM-1 (TZ-PIM-1)[40] exhibit a higher gas selectivity in the CO_2/N_2 and CO_2/CH_4 mixtures than the selectivity measured for single gases. This is due to their rigidified structures resisting plasticisation-induced swelling and thus retaining the sieving properties. The extraordinary rigidity of AO-PIM-DBMP-1, as the result of the synergy of the improved intrachain and interchain interactions as compared with previously reported polymers, was anticipated to have good plasticisation resistance and maintain its good separation performance for gas mixtures.

Chapter 7 Experimental

7.1 Techniques

Commercially available reagents were used without further purification unless stated otherwise. Anhydrous dichloromethane (DCM) and tetrahydrofuran (THF) were obtained from a Solvent Purification System (SPS facility). Dry dimethylformamide (DMF) was from Sigma Aldrich. All air/moisture sensitive reactions were carried out under a nitrogen atmosphere using oven-dried apparatus. Analytical thin layer chromatography (TLC) was carried out with aluminium-back plates coated with Merck Kieselgel 60 GF_{254}. Column chromatography was performed over silica gel 60 Å (40-63 µm) chromatography grade (Fisher Scientific).

Gas permeation

The detailed procedure can be found everywhere.[155] Single gas permeation measurements were carried out at 25 °C and a feed pressure of 1 bar in a fixed volume pressure increase apparatus (GKSS, Germany) using the time-lag mode. The instrument is equipped with PC controlled pneumatic valves to allow response times less than 0.5 s. The gases were tested in the following order: He, H_2, N_2, O_2, CH_4, and CO_2. Before each experiment the membrane sample was evacuated to a low pressure (10−2 mbar) to remove any dissolved species. Circular samples with an effective membrane area of 2.14 cm^2 were used. The thickness of the films was determined using a digital micrometer (Mitutoyo, Model IP65). Prior test, the films were soaked in methanol for 24 h and then dried at ambient temperature. Permeability (*P*) is reported in Barrer (1 Barrer = 10^{-10} cm^3 (STP) cm cm^{-2} s^{-1} cm Hg^{-1}), and the diffusivity coefficient (*D*) is calculated from the permeation time lag, Θ (s) using the following equation:

$$D = \frac{L^2}{6\Theta}$$

where *L* is the film thickness. The gas solubility coefficient (*S*) is calculated indirectly as the ratio of permeability over the diffusivity coefficient according to the solution-diffusion model.

$$s = \frac{p}{\mathrm{D}}$$

Melting Points (Mp)

Melting points were recorded using a Stuart Digital Melting Point Apparatus with a maximum of 300 °C, and are uncorrected.

Thermo-Gravimetric Analysis (TGA)

Thermo-gravimetric analysis (TGA) was carried out using a Thermal Analysis SDTQ600 system with a sample heating rate of 10 °C min^{-1} up to 800 °C under nitrogen atmosphere.

Infrared Spectroscopy (IR)

Infrared transmission spectra were recorded using powder or liquid in the range 4000-500 cm^{-1} using a Shimadzu IR Affinity-1S FTIR spectrophotometer.

Nuclear Magnetic Resonance (NMR)

^{1}H spectra were recorded in a suitable deuterated solvent using Avance Bruker AVA400 (400 MHz), AVA500 (500 MHz), PRO500 (500 MHz) or AVA 600 instruments, with ^{13}C NMR recorded at 100 MHz, 125MHz or 126 MHz respectively. Solid state ^{13}C NMR spectra were recorded using a Bruker Ultrashield ™ 300 WB spectrometer operating at 76 MHz.

Mass Spectrometry (MS)

Low-resolution mass spectrometry (LRMS) were determined using a Fisons VG Platform II quadrupole instrument using electron impact ionization (EI) unless otherwise stated. High-resolution mass spectrometry (HRMS) were obtained in electron impact ionization (EI) mode unless otherwise stated, on a Waters Q-TOF micromass spectrometer.

Gel Permeation Chromatography (GPC)

Gel permeation chromatography (GPC) was performed with chloroform solutions (~1 mg mL^{-1}) using a GPC MAX 1000 system equipped with two Viscotek CLM3012 LT 5000L columns and a RI(VE3580) detector, operating at a flow rate of 1 mL min^{-1}. Calibration was achieved using Viscotek polystyrene standards (*Mw* 1000-1000 000 g mol^{-1}).

Breunauer-Emmett-Teller (BET) surface areas

Low-temperature (77 K) N_2 and CO_2 (273 K) adsorption/desorption isotherms were obtained using a Quantachrome Quadrasorb automated surface area analyser. Accurately weighed powdered samples (~100 mg) were degassed at 120 °C for 12 h under high vacuum prior to analysis.

7.2 Monomer Synthesis

General procedure for microwave assisted Diels-Alder reactions (G.P 1)

In a microwave vessel, the corresponding diene and dienophile were dissolved in DMF and heated in the microwave reactor at 250 °C for 2 h at a pressure of 7 bar. After cooling, the resulting solution was poured into water, filtered off and washed with water repeatedly. The crude product was purified appropriately.

General procedure for pressure assisted Diels-Alder reactions (G.P 2)

In a 100 mL high-pressure reactor, the required diene and dienophile was dissolved in xylene and heated at 260 °C for 96 h. After cooling, the mixture was extracted with dichloromethane (DCM). The solvent was removed under vacuum to afford the crude product which was purified appropriately.

General procedure for the synthesis of biscatechol monomers (G.P 3)

The required biscatechol monomers were synthesised according to the general procedure reported by Ghanem *et al*.[199] The tetramethoxy precursor was dissolved in anhydrous DCM and cooled to 0 °C under a nitrogen atmosphere. Boron tribromide (3.0 eq.) was added dropwise and left at 0 °C for 30 minutes, then allowed to warm to room temperature for 2.5 h. The reaction mixture was poured into water and allowed DCM to evaporate under nitrogen environment. Finally, the product was extracted with ethyl acetate and precipitated from n-hexane.

2,3,6,7-Tetramethoxy-9,10-dimethylanthracene (1)

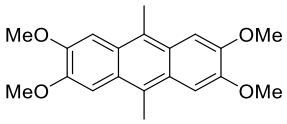

The compound 2,3,6,7-tetramethoxy-9,10-dimethylanthracene (**1**) was synthesised according to the procedure reported by Ghanem *et al*.[199] A solution of veratrole (20 mL, 157.0 mmol), acetaldehyde (8.8 mL, 157.mmol) and CH_3CN (8.2 mL, 157 mmol) was cooled to 0 °C. To this, *c*H_2SO_4 (75 mL) was added drop wise and maintained at 0 °C for 2 h. The resulting solution was poured onto ice, neutralised with aqueous sodium hydroxide solution (2 M) and filtered off. Washed precipitate with water, methanol and acetone to yield **1** (9.9 g, 30.3 mmol, 38 %) as an off-white solid. Mp: Above 300 °C; ν_{max} (cm^{-1}): 2995, 2982, 2967, 2957, 2922, 1497, 1468, 1447, 1439, 1381, 1371, 1250, 1209, 1202, 1190, 1163, 1146, 1084, 1030, 959, 893, 822, 750; ^{1}H NMR (500 MHz, $CDCl_3$): δ_H (ppm) 7.40 (s, 4H), 4.08 (s, 12H), 2.94 (s, 6H); ^{13}C NMR (126 MHz, $CDCl_3$): δ_C(ppm) 148.9, 126.0, 124.0, 102.8, 55.8, 14.9; LRMS (EI, m/z): Calculated: 326.15 found: 326.1 [M^+].

6-Trifluoromethyl-1,4-dihydro-1,4-epoxynaphthalene (2)

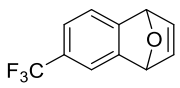

The compound 6-trifluoromethyl-1,4-dihydro-1,4-epoxynaphthalene (**2**) was synthesised according to the procedure reported by Bailly *et al*.[200] 4-Chlorofluorobenzene (10.0 g, 55.4 mmol) was dissolved in anhydrous THF (80 mL) and cooled to -78 °C. *n*-BuLi (29.0 mL, 72.0 mmol) was added dropwise and left to stir at -78 °C for 1 h. The reaction solution was transferred dropwise into furan (40.0 mL, 552 mmol) and left at room temperature for 2 h. After solvent removal, the crude product was filtered through a pad of basic alumina using diethyl ether as eluent. The resulting oil was distilled under vacuum to yield pure **2** as a colourless oil (5.7 g, 26.8 mmol, 48%). ν_{max} (cm^{-1}): 3019, 2359, 2324, 1427, 1354, 1323, 1275, 1198, 1167, 1140, 1049, 995, 897, 872, 853, 839, 750, 700, 654, 637, 544; ^{1}H NMR (500 MHz, $CDCl_3$): δ (ppm) 7.46 (s, 1H), 7.32 (d, *J* = 7.4 Hz, 1H), 7.30 (d, *J* = 7.4 Hz, 1H), 7.07-7.03 (m, 2H),

5.76-5.57 (m, 2H); ^{13}C NMR (151 MHz, $CDCl_3$): δ (ppm) 153.4, 150.5, 143.3, 142.8, 127.6 (q, *J* = 33 Hz), 127.0, 125.3, 123.4, 123.2 (q, *J* = 4 Hz), 121.6, 120.1, 117.1 (q, *J* = 4 Hz), 82.3; LRMS (EI, m/z): [M^+] calcd.: 212.04, found: 212.0.

5,7-Bis(trifluoromethyl)-1,4-dihydro-1,4-epoxynaphthalene (3)

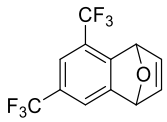

The compound 5,7-bis(trifluoromethyl)-1,4-dihydro-1,4-epoxynaphthalene (**3**) was obtained according to the procedure reported by Bailly *et al*.[200] 2,4-Bis(trifluoromethyl)chlorobenzene (10.0 g, 40.2 mmol) was dissolved into anhydrous THF (80 mL) and cooled to -78 °C. To this, a solution of *n*-BuLi was added dropwise and left to stir at -78 °C for 1 h. The resulting solution was transferred into anhydrous degassed furan (88.0 mL, 1207 mmol) and kept at room temperature for 24 h. Solvent was removed under vacuum and the resulting oil was filtered through a pad of basic alumina using diethyl ether as eluent. The desired product **3** was obtained by distillation under vacuum as colourless oil (4.5 g, 16.1 mmol, 40%). ν_{max}(cm^{-1}): 3036, 1389, 1325, 1287, 1256, 1192, 1175, 1142, 1069, 899, 872, 843, 820, 752, 704, 667, 635, 625; ^{1}H NMR (400 MHz, $CDCl_3$): δ_H (ppm) 7.61 (s, 1H), 7.49 (s, 1H), 7.11 (dd, *J* = 5.5, 1.9 Hz, 1H), 7.06 (dd, *J* = 5.5, 1.9 Hz, 1H), 6.08-6.01 (m, 1H), 5.87-5.81 (m, 1H); ^{13}C NMR (126 MHz, $CDCl_3$): δ_C (ppm) 152.5, 144.0, 142.3, 128.8 (q, *J* = 33 Hz), 126.8, 126.6, 124.6, 124.4, 124.0 (q, *J* = 35 Hz), 122.5, 122.3, 119.5 (dt, *J* = 8, 4 Hz), 81.9, 81.6 (q, *J* = 2 Hz); HRMS (EI, m/z): [M^+] calcd.: 280.0317, found: 280.0317.

2,3,6,7-Tetramethoxy-9,10-(4'-trifluoromethyl-2',7'-dihydro-2',7'-epoxynaphthalene)-9,10dimethylanthracene (4)

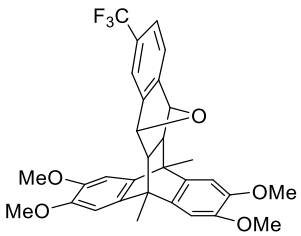

G.P.1 was followed using 2,3,6,7-tetramethoxy-9,10-dimethylanthracene (**1**) (2.2 g, 6.8 mmol) and 6-trifluoromethyl-1,4-dihydro-1,4-epoxynaphthalene (**2**) (1.0mL, 6.8 mmol) in DMF (15 mL). The obtained crude product was purified by column chromatography DCM/ethyl acetate (20:1, v/v) to yield adduct **4** (1.9 g, 3.5 mmol, 52%) as light brown crystalline solid. Mp: 138-140 °C; ν_{max} (cm^{-1}): 2938, 1506, 1485, 1462, 1437, 1404, 1319, 1292, 1279, 1196, 1148, 1113, 1045, 1020, 951, 885, 843, 818, 783, 746, 677, 669, 660, 606, 579; ^{1}H NMR (500 MHz, $CDCl_3$): δ_H (ppm) 7.38 (s, 1H), 7.34 (d, *J* = 7.7 Hz, 1H), 7.22 (d, *J* = 7.6 Hz, 1H), 6.88 (s, 1H), 6.87 (s, 1H), 6.84 (s, 2H), 5.05 (d, *J* = 1.9 Hz, 2H), 3.89 (s, 3H), 3.89 (s, 3H), 3.84 (s, 6H), 2.08 (s, 6H), 2.04-2.00 (m, 2H); ^{13}C NMR (151 MHz, $CDCl_3$): δ_C (ppm) 150.8, 148.0, 147.1, 146.7, 146.7, 140.2, 140.1, 136.6, 136.6, 128.9 (q, *J* = 32 Hz), 127.6, 125.4, 124.1 (t, *J* = 4 Hz), 123.3, 121.1, 118.9, 115.8 (q, *J* = 4 Hz), 106.7, 106.7, 106.2, 106.1, 79.6, 79.6, 56.6, 56.5, 56.0, 55.8, 43.1, 17.3, 17.2; HRMS (EI, m/z): [M^+] calcd.: 538.1962 found: 538.1969.

2,3,6,7-Tetramethoxy-9,10-(3',5'-bis(trifluoromethyl)-2',7'-dihydro-2',7'-epoxynaphthalene)-9,10-dimethylanthracene (5)

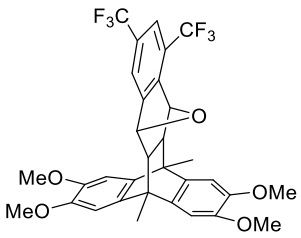

G.P.1 was followed using 2,3,6,7-tetramethoxy-9,10-dimethylanthracene **(1)** (1.5 g, 4.6 mmol) and 5,7-bis(trifluoromethyl)-1,4-dihydro-1,4-epoxynaphthalene **(3)** (0.8 mL, 4.6 mmol) in DMF (15 mL). The crude product was purified by trituration with MeOH to afford **5** (1.6 g, 2.7 mmol, 58%) as light brown powder. Mp 166-168 °C; ν_{max} (cm^{-1}): 2965, 2938, 2830, 1506, 1487, 1464, 1404, 1385, 1327, 1277, 1254, 1242, 1194, 1159, 1121, 1074, 1045, 1020, 949, 895, 870, 835, 820, 783, 752, 687, 673, 633, 608, 571; ^{1}H NMR (400 MHz, $CDCl_3$): δ_H (ppm) 7.56 (s, 2H), 6.90 (s, 1H), 6.88 (s, 1H) 6.85 (s, 1H), 6.84 (s, 1H), 5.31 (s, 1H), 5.14 (s, 1H), 3.90 (s, 3H), 3.90 (s, 3H), 3.84 (s, 3H), 3.83 (s, 3H), 2.09 (s, 3H), 2.08 (s, 3H), 2.03 (s, 2H); ^{13}C NMR (126 MHz, $CDCl_3$): δ_C (ppm) 149.9, 147.3, 147.3, 146.9, 146.8, 139.9, 136.4, 136.3, 130.1, 122.4, 120.7, 119.0, 106.9, 106.8, 106.3, 106.2, 79.4, 79.2, 56.6, 56.6, 56.5, 56.5, 55.7, 55.0, 43.1, 43.1, 17.2, 16.9; HRMS (EI, m/z): [M^+] calcd.: 606.1835, found: 606.1855.

2,3,6,7-Tetramethyl-9,10-dimethyl-13-trifluoromethylbenzotriptycene (6)

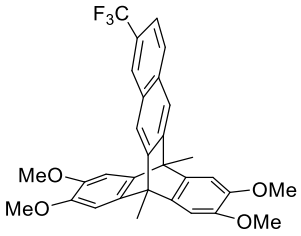

2,3,6,7-Tetramethoxy-9,10-(4'-trifluoromethyl-2',7'-dihydro-2',7'-epoxynaphthalene)-9,10dimethylanthracene (**4**) (6.2 g, 11.6 mmol) was dissolved into methanesulfonic acid (180 mL) and stirred at room temperature for 24 h. The reaction mixture was poured into ice/water, neutralised with sodium hydroxide aqueous (2 M), extracted with DCM and dried over $MgSO_4$. The crude product was purified by column chromatography DCM/ethyl acetate (40:1 v/v) to afford compound **6** (5.6 g, 10.8 mmol, 93%) as a white solid. Mp: 289-291 °C; ν_{max} (cm^{-1}): 2951, 1604,1585, 1516, 1489, 1443, 1408, 1384, 1327, 1281, 1258, 1223, 1184, 1146, 1111, 1065, 1038, 934, 903, 887, 872, 837, 814, 795, 752, 698, 679, 667, 640, 617, 598, 559; ^{1}H NMR (500 MHz, $CDCl_3$): δ_H (ppm) 8.01 (s, 1H), 7.80 (d, *J* = 8.6 Hz, 1H), 7.72 (s, 1H), 7.70 (s, 1H), 7.54 (dd, *J* = 8.6, 1.8 Hz, 1H,), 6.99 (s, 4H), 3.86 (s, 6H), 3.86 (s, 6H), 2.51 (s, 3H), 2.51 (s, m, 3H); ^{13}C NMR (126 MHz, $CDCl_3$): δ_C (ppm) 148.6, 147.7, 146.5, 146.5, 140.5, 140.4, 132.9, 130.4, 128.5, 127.9, 127.6 (q, *J* = 32 Hz), 125.7, 125.2 (q, *J* = 4 Hz), 123.6, 121.5 (q, *J* = 3 Hz), 119.0, 118.2, 106.2, 106.2, 56.5, 47.8, 47.7, 14.3; HRMS (EI, m/z): [M^+] calcd.: 520.1856, found: 520.1881.

2,3,6,7-Tetramethyoxy-9,10-dimethyl-12,14-bis(trifluoromethyl)benzotriptycene (7)

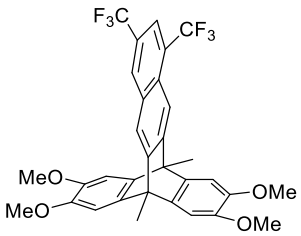

2,3,6,7-Tetramethoxy-9,10-(3',5'-bis(trifluoromethyl)-2',7'-dihydro-2',7'-epoxynaphthalene)-9,10-dimethylanthracene (**5**) (5.2 g, 8.5 mmol) was dissolved into

methanesulfonic acid (80 mL) and reacted at room temperature for 24 h. The reaction mixture was poured into ice/water bath, neutralised with sodium hydroxide aqueous (2 M), extracted with DCM and dried over $MgSO_4$. The crude product was purified by column chromatography (DCM) to yield **7** (4.7g, 7.9 mmol, 93 %) as a white solid. Mp 138-140 °C; ν_{max} (cm^{-1}): 2970, 2940, 2830, 1607, 1582, 1487, 1449, 1439, 1406, 1385, 1344, 1275, 1209, 1186, 1152, 1115, 1088, 1042, 1016, 959, 899, 887, 870, 762, 752, 733, 667, 613; ^{1}H NMR (601 MHz, $CDCl_3$): δ_H (ppm) 8.20 (s, 1H), 8.04 (s, 1H), 7.92 (s, 1H), 7.80 (s, 1H), 7.01 (s, 2H), 6.99(s, 2H), 3.87 (s, 6H), 3.86 (s, 6H), 2.54 (s, 3H), 2.52 (s, 3H); ^{13}C NMR (126 MHz, $CDCl_3$): δ_C (ppm) 150.6, 148.6, 146.7, 146.7, 140.1, 140.0, 131.5, 129.7 (q, *J* = 4 Hz), 128.7 (q, *J* = 33 Hz), 126.4 (q, *J* =33 Hz), 125.4, 125.0, 123.2, 122.8, 120.4 (dt, *J* = 8, 4 Hz), 119.7, 114.8, 106.3, 106.2, 56.6, 56.5, 48.2, 47.7, 14.1, 14.1; HRMS (EI, m/z): [M^+] calcd.: 588.1730, found: 588.1746.

2,3,6,7-Tetrahydroxy-9,10-dimethyl-13-trifluoromethylbenzotriptycene (8)

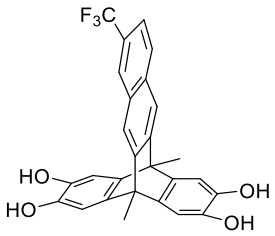

G.P.3 was followed using 2,3,6,7-tetramethyl-9,10-dimethyl-15-trifluoromethyl-benzotriptycene (3.1 g, 6.0 mmol) and boron tribromide (1.1 mL, 12.0 mmol) in anhydrous DCM (50 mL) and cooled to 0 °C to afford **8** (1.8 g, 3.9 mmol, 65 %) as a white powder. ν_{max} (cm^{-1}): 3352, 2970, 1612, 1487, 1443, 1379, 1329, 1298, 1263, 1186, 1155, 1117, 1065, 986, 934, 907, 843, 812, 762, 619, 598; ^{1}H NMR (601 MHz, MeOD): δ_H (ppm) 8.04 (s, 1H), 7.84 (d, *J* = 9.0 Hz, 1H), 7.69 (s, 1H), 7.65 (s, 1H), 7.51(dd, *J* = 8.6, 1.9 Hz, 1H), 6.84 (s, 4H), 2.31 (s, 6H); ^{13}C NMR (151 MHz, MeOD): δ_C (ppm) 151.1, 150.1, 142.9, 142.8, 141.1, 141.0, 134.3, 131.6, 129.7, 127.9, 127.0, 126.0 (q, *J* = 4 Hz), 121.7 (q, *J* = 4 Hz), 119.2, 118.4, 110.1, 110.1, 48.1, 48.0, 14.5, 14.5; HRMS (EI, m/z): [M^+] calcd.: 464.1229, found: 464.1229.

2,3,6,7-Tetrahydroxy-9,10-dimethyl-12,14-bis(trifluoromethyl)benzotriptycene (9)

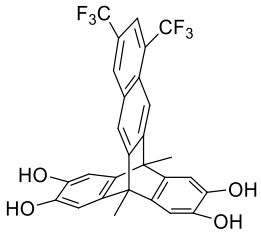

G.P.3 was followed using 2,3,6,7-tetramethyoxy-9,10-dimethyl-12,14-bis(trifluoromethyl)benzotriptycene (**7**) (3.0 g, 5.1 mmol) and boron tribromide (1.5 mL, 15.3 mmol) in anhydrous DCM (50 mL) to afford **9** (2.5 g, 4.7 mmol, 92 %) as a white powder. ν_{max} (cm^{-1}): 3429, 2974, 1614, 1489, 1445, 1383, 1342, 1298, 1277, 1207, 1188, 1157, 1117, 1088, 1015, 988, 957, 924, 903, 889, 880, 841, 775, 762, 669, 617; ^{1}H NMR (400 MHz, $(CD_3)_2CO$): δ_H (ppm) 8.53 (s, 1H), 8.08 (s, 1H), 8.01-7.98 (m, 2H), 7.63 (*br*, s, 3H), 6.96 (s, 2H), 6.95 (s, 2H), 2.39 (s, 6H); ^{13}C NMR (126 MHz, $(CD_3)_2CO$): δ_C (ppm) 153.0, 150.7, 142.7, 140.2, 140.0, 132.5, 131.3 (q, J = 5 Hz), 129.1, 127.4, 127.2, 126.8-125.8 (m), 124.2, 123.9, 120.6, 114.3, 110.3, 110.2, 48.2, 47.8, 14.3, 14.2; HRMS (EI, m/z): [M^+] calcd.: 532.1104, found: 532.1128.

2,3-Octafluorocyclopenta-5-norbornene (10a)

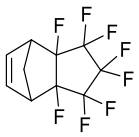

The compound 2,3-octafluorocyclopenta-5-norbornene (**10a**) was synthesized according to the procedure reported by Seehof *et al*.[169] Octafluorocyclopentene (17.7 g, 83.5 mmol), cyclopentadiene (4.5 g, 67.8 mmol) and hydroquinone (0.1 g) were added into 100 mL autoclave. The mixture was heated at 150 °C for 72 h. The resulted oil was purified by column chromatography (petroleum ether 40-60 °C) to afford **10a** as colorless oil (3.3 g, 11.9 mmol, 30%, mixture of endo/exo-isomers); ν_{max} (cm^{-1}): 3003, 1331, 1290, 1180, 1165, 1082, 1026, 945, 889, 781, 744, 578; ^{1}H NMR (400 MHz,$CDCl_3$): δ_H (ppm): 6.13 (s, 2H), 3.24 (m, 2H), 2.45 (dd, *J* = 9.8, 1.9 Hz, 1H), 2.19 (dd, *J* = 10.0, 1.7 Hz, 1H); 6.48 (s, 2H), 3.39 (d, *J* = 1.6 Hz, 2H), 1.91-1.78 (m, 1H), 1.78-1.67 (m, 1H); ^{13}C NMR (126 MHz, $CDCl_3$) δ_C (ppm): 136.7, 135.2, 116.1-115.3 (m, CF), 114.3-113.0 (m, CF), 112.1-110.7 (m, CF), 99.3 (dt, *J* = 31.9, 15.6 Hz, CF), 97.5

(dt, *J* = 31.2, 15.4 Hz, CF), 48.9, 48.5-48.1, 45.1-44.8, 41.4-41.2; HRMS (EI, m/z): [M^+] calcd.: 278.0336, found: 278.0321.

(10b)

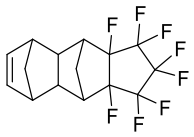

A side product of the Diels-Alder reaction for **10a** was obtained in a 19% yield. ν_{max} (cm^{-1}): ^1H NMR (400 MHz,$CDCl_3$): δ_H (ppm): 6.11 (t, *J* = 2.0 Hz, 1H), 3.06 – 3.00 (m, 1H), 2.81 – 2.75 (m, 1H), 2.76 – 2.72 (m, 1H), 1.46 – 1.41 (m, 1H), 1.37 – 1.31 (m, 1H), 0.97 – 0.89 (m, 1H); ^{13}C NMR (126 MHz, $CDCl_3$) δ_C (ppm): 136.78, 116.48-115.98, 114.71-113.69, 112.61-111.68, 96.79-96.31, 95.01-94.48, 53.87, 46.76, 41.38-41.25, 38.10-38.02, 26.63-26.42. HRMS (EI, m/z): [M^+] calcd.: 344.0809, found: 344.0807.

2,3-Cyclopenta-5-norbornene (11)

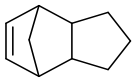

The compound 2,3-cyclopenta-5-norbornene (**11**) was synthesized according to the method reported by Hong *et al*.[170] Under nitrogen environment, dicyclopentadiene (11.7 g, 88.8 mmol), cyclopentene (42.4 g, 622.6 mmol) and butylated hydroxytoluene (1.0 g) were added into 100 mL autoclave. The autoclave was sealed and heated at 200 °C for 15 h. The obtained oil was purified via distillation under reduced pressure to afford the product **11** as a colourless oil (9.3 g, 69.3 mmol, 39%, 68 °C at 20 torr). ν_{max} (cm^{-1}): 2945, 1445, 1348, 1323, 1252, 1144, 1013, 899, 787, 731, 694; ^1H NMR (400 MHz, $CDCl_3$) δ_H (ppm): 6.11 (t, *J* = 2.0 Hz, 2H), 2.77-2.70 (m, 2H), 2.65-2.54 (m, 2H), 1.67-1.52 (m, 4H), 1.49-1.40 (m, 2H), 1.06-0.92 (m, 2H); ^{13}C NMR (126 MHz, $CDCl_3$): δ_C (ppm): 136.4, 53.5, 47.4, 46.1, 30.4, 28.9; HRMS (EI, m/z): [M^+] calcd.: 134.0190, found: 134.1081.

2,3,6,7-Tetramethoxy-9,10-(4',7'-methano-1',1',2',2',3',3',3a,7a-octafluoro-1'*H*-perhydroindenyl)-9,10-dimethylanthracene (12)

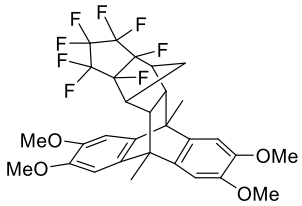

G.P.1 was followed using 2,3-octafluorocyclopenta-5-norbornene (**10**) (2.0 g, 7.2 mmol) and 2,3,6,7-tetramethoxyl-9,10-dimethylanthracene (**1**) (1.8 g, 5.5 mmol) in DMF (15 mL). The crude product was purified by column chromatography (DCM) to afford **12** (1.5 g, 2.5 mmol, 45%) as an off-white solid. Mp: 207-208 °C; ν_{max} (cm^{-1}): 2943, 1620, 1487, 1462, 1348, 1292, 1271, 1161, 1045, 1024, 924, 891, 866, 787, 573, 542; ^{1}H NMR (500 MHz, $CDCl_3$): δ_H (ppm) 6.88 (s, 2H), 6.80 (s, 2H), 3.88 (s, 12H), 2.69 (s, 2H), 2.38 (s, 2H), 1.97 (s, 6H), 0.75 (d, *J* = 14.1 Hz, 1H), 0.16-0.11 (m, 1H); ^{13}C NMR: (126 MHz, $CDCl_3$) δ_C (ppm) 147.5, 146.9, 139.8, 137.0, 116.3-115.7 (m, CF), 114.3-113.5 (m, CF), 112.2-111.6 (m, CF), 106.8, 105.6, 96.2-95.7 (m, CF), 94.4-93.9 (m, CF), 56.4, 46.1-45.8, 42.8, 40.9-40.6, 26.4-26.2, 16.7; HRMS (EI, m/z): [M^+] calcd.: 604.1854, found: 604.1828.

2,3,6,7-Tetramethoxy-9,10-(4',7'-methano-1'*H*-perhydroindenyl)-9,10-dimethylanthracene (13a)

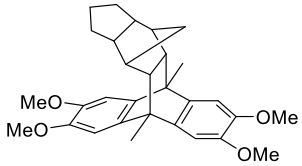

G.P.1 was followed using 2,3-cyclopenta-5-norbornene (**11**) (0.3 g, 2.0 mmol) and 2,3,6,7-tetramethoxy-9,10-dimethylanthracene (**1**) (0.5 g, 1.5 mmol) in DMF (3 mL). The crude product was purified by column chromatography DCM/ethyl acetate (50/1, v/v) to afford the product **13a** as an off-white solid (0.15 g, 3.3 mmol, 22%, mixture of isomers). Mp: 98-99 °C; ν_{max} (cm^{-1}):2936, 1613, 1579, 1483, 1458, 1402, 1281, 1242, 1196, 1148, 1047, 1022, 864, 642; ^{1}H NMR (500 MHz, $CDCl_3$): δ_H (ppm): 6.85 (s, 2H), 6.77 (s, 2H), 3.92-3.81 (m, 12H), 1.92 (s, 6H), 1.79 (m, 2H), 1.73 (dt, *J* = 13.3, 7.0 Hz, 2H), 1.65-1.55 (m, 5H), 1.15-1.06 (m, 1H), 0.81-0.74 (m, 2H), 0.48 (d, *J* = 11.1 Hz, 1H), -0.58 (d, *J* = 11.1 Hz, 1H); 6.84 (s, 2H), 6.75 (s, 2H), 3.87 (s, 6H), 3.86 (s, 6H), 2.29-2.24 (m, 2H), 1.99-1.95 (m, 2H), 1.87 (s, 6H), 1.81 (s, 2H), 1.51-1.40 (m,

3H), 1.40-1.29 (m, 3H), 0.58 (d, *J* = 10.3 Hz, 1H), -0.20 (d, *J* = 10.3 Hz, 1H); ^{13}C NMR (126 MHz, $CDCl_3$): δ_C (ppm): 146.9, 146.8, 146.3, 146.2, 141.0, 140.9, 138.3, 137.7, 106.7, 106.7, 105.5, 105.5, 56.8, 56.4, 56.4, 56.4, 49.8, 49.7, 47.3, 43.6, 43.4, 42.5, 42.0, 38.5, 31.4, 29.3, 27.7, 26.9, 26.2, 17.2, 16.9; HRMS (EI, m/z): [M^+] calcd.: 460.2608, found: 460.2600.

2,3,6,7-Tetrahydroxy-9,10-(4',7'-methano-1',1',2',2',3',3',3a,7a-octafluoro-1'*H*-perhydroindenyl)-9,10-dimethylanthracene (14)

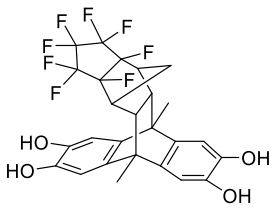

G.P.3 was followed using 2,3,6,7-tetramethoxy-9,10-(4',7'-methano-1',1',2',2',3',3',3a,7a-octafluoro-1'*H*-perhydroindenyl)-9,10-dimethylanthracene (**12**) (2.2 g, 3.6 mmol) and boron tribromide (1.0 mL, 10.8 mmol) in anhydrous DCM (50 mL) to afford **14** (1.7 g, 3.1 mmol, 83%) as a white powder. ν_{max} (cm^{-1}): 3229 (*br*), 2967, 1620, 1450, 1346, 1306, 1184, 1163, 1136, 1028, 924, 893, 876, 802, 544; ^{1}H NMR (400 MHz, DMSO-d_6): δ_H (ppm): 8.67 (s, 2H), 8.58 (s, 2H), 6.67 (s, 2H), 6.62 (s, 2H), 2.93 (s, 2H), 2.08 (s, 2H), 1.75 (s, 6H), 0.60 (d, *J* = 14.1 Hz, 1H), 0.18-0.12 (m, 1H); ^{13}C NMR (126 MHz, DMSO-d_6): δ_C (ppm) 142.7, 142.1, 138.3, 135.2, 115.7-115.3 (m, CF), 113.8-113.2 (m, CF), 111.9-111.2 (m, CF), 110.4, 108.9, 96.2-95.8 (m, CF), 94.4-93.9 (m, CF), 45.5-45.5, 41.9, 41.5, 25.8, 16.2; HRMS (EI, m/z): [M^+] calcd.: 548.1228, found: 548.1203.

2,3,6,7-Tetrahydroxy-9,10-(4',7'-methano-1'*H*-perhydroindenyl)-9,10-dimethylanthracene (15)

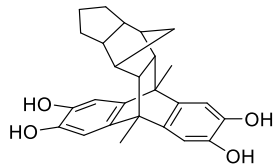

G.P.3 was followed using 2,3,6,7-tetramethoxy-9,10-(4',7'-methano-1'*H*-perhydroindenyl)-9,10-dimethylanthracene (**13a**) (1.0 g, 2.2 mmol) and boron tribromide (0.62 mL, 6.6 mmol) in anhydrous DCM (20 mL) to afford **15** (0.7 g, 1.7 mmol, 79%, mixture of isomers) as a white

powder. ν_{max} (cm^{-1}): 3399 (*br*), 2938, 1616, 1508, 1485, 1445, 1377, 1298, 1188, 1132, 989, 874, 822, 800, 642; ^{1}H NMR (500 MHz, DMSO-d_6): δ_H (ppm) 8.40 (s, 2H), 8.38 (s, 2H), 6.60 (s, 2H), 6.51 (s, 2H), 2.22-2.20 (m, 2H), 1.89-1.86 (m, 2H), 1.63 (s, 8H), 1.48-1.42 (m, 2H), 1.35-1.19 (m, 4H), 0.51 (d, *J* = 9.7 Hz, 1H), -0.16 (d, *J* = 9.8 Hz, 1H); 8.42 (s, 2H), 8.37 (s, 2H), 6.59 (s, 2H), 6.53 (s, 2H), 1.69 (s, 3H), 1.67 (s, 6H), 1.61-1.55 (m, 2H), 1.58-1.49 (m, 1H), 1.44-1.35 (m, 3H), 1.11-1.01 (m, 1H), 0.74 (m, 2H), 0.42 (d, *J* = 10.5 Hz, 1H), -0.55 (d, *J* = 10.6 Hz, 1H); ^{13}C NMR (126 MHz, DMSO-d_6) δ_C (ppm): 142.1, 142.0, 141.4, 141.4, 139.3, 139.1, 136.5, 136.0, 110.1, 110.0, 108.7, 56.4, 49.4, 49.1, 46.6, 42.1, 42.0, 41.9, 41.4, 38.1, 30.9, 30.9, 28.9, 27.2, 26.6, 25.9, 22.1, 16.9, 16.6, 14.0; HRMS (EI, m/z): [M^+] calcd.: 404.1982, found: 404.1962.

2-Heptadecafluorooctanyl-5-norbornene (16)

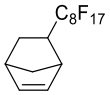

1H,1H,2H-Heptadecafluorodec-1-ene (16.8 g, 37.6 mmol) and dicyclopentadiene (2.0 g, 18.6 mmol) were added into a microwave vessel. The reaction mixture was heated in the microwave reactor at 200 °C, 1 bar for 2 h. The resulting oil was distilled under reduced pressure to afford **16** (14.6 g, 28.6 mmol, 76%, 78 °C at 1.6 torr, mixture of endo/exo-isomers) as colourless liquid. ν_{max} (cm^{-1}): 2970, 1368, 1198, 1144, 1115, 704, 650, 557; ^{1}H NMR (601 MHz, $CDCl_3$): δ_H (ppm) 6.20-6.17 (m, 2H), 3.17 (s, 1H), 2.93 (s, 1H), 2.85-2.73 (m, 1H), 2.00-1.96 (m, 1H), 1.49-1.46 (m, 1H), 1.30-1.28 (m, 1H), 1.27-1.24 (m, 1H) (major isomer, 67 %); 5.96 (m, 2H), 3.15 (s, 1H), 2.98 (s, 1H), 2.10-2.01 (m, 1H), 1.84-1.80 (m, 1H), 1.53-1.51 (m, 1H), 1.42-1.34 (m, 2H) (minor isomer, 33 %); ^{13}C NMR (126 MHz, $CDCl_3$) δ_C (ppm) 138.4, 137.4, 136.5, 131.9, 121.8-120.5 (m, CF), 119.8-118.2 (m, CF), 117.7-116.8 (m, CF), 116.4-115.9 (m, CF), 113.9-112.6 (m, CF), 111.9-111.2 (m, CF), 109.5-108.1 (m, CF), 106.9-106.0 (m, CF), 49.8, 46.6, 43.8, 42.6, 42.2, 41.4, 41.2-41.0, 40.4 (t, *J* = 19.5 Hz), 27.8, 27.0; HRMS (EI, m/z): [M^+] calcd.: 512.0427, found: 512.0436.

2,3,6,7-Tetramethoxy-9,10-(2'-Heptadecafluorooctacanylbenzomethano)-9,10-dimethylanthracene (17)

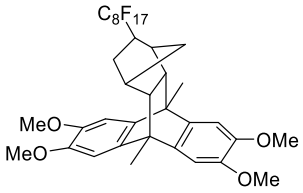

G.P.2 was followed using 2-heptadecafluorooctanyl-5-norbornene (**16**) (7.9 g, 15.3 mmol) and 2,3,6,7-tetramethoxy-9, 10-dimethylanthracene (**1**) (5.0 g, 15.3 mmol) were dissolved in xylene (5.0 mL). Purified by column chromatography (DCM) to afford **17** (5.3 g, 6.3 mmol, 41%, mixture of isomers) as light brown solid. Mp: 97-98 °C; ν_{max} (cm^{-1}): 2963, 1580, 1487, 1460, 1283, 1196, 1146, 1043, 866, 642 ; ^{1}H NMR (400 MHz, $CDCl_3$): δ_H (ppm) 6.88 (m, 2H), 6.81 (m, 2H), 3.90-3.88 (m, 12H), 2.52-2.46 (m, 1H), 2.22-2.17 (m, 1H), 1.97-1.94 (m, 6H), 1.79-1.76 (m, 1H), 1.70-1.61 (m, 2H), 1.45-1.28 (m, 1.5H), 0.92-0.85 (m, 0.5H), 0.68 (d, *J* = 11.2 Hz, 0.8H), 0.47 (d, *J* = 10.9 Hz, 0.2H), -0.13 (d, *J* = 11.1 Hz, 0.8H), -0.27 (d, *J* = 11.2 Hz, 0.2H); ^{13}C NMR (126 MHz, $CDCl_3$): δ_C (ppm) 147.4, 147.3, 147.2, 147.2, 146.7, 146.6, 146.6, 140.5, 140.4, 140.2, 140.2, 137.8, 137.6, 137.0, 118.8-118.2 (m, CF), 116.4-115.9 (m, CF), 113.9-108.4 (m, CF), 107.0, 106.9, 106.9, 106.7, 105.9, 105.7, 105.5, 57.9, 56.5-56.4, 55.6, 49.5, 45.0 (t, *J* = 20.6 Hz), 43.7-43.5, 40.0, 38.5, 38.1, 37.0, 35.1, 32.9, 32.1, 31.5, 17.3, 17.0, 16.9, 16.7; HRMS (EI, m/z): [M^+] calcd.: 838.1945, found: 838.1989.

2,3,6,7-Tetrahydroxy-9,10-(2'-heptadecafluorooctacanylbenzomethano)-9,10-dimethylanthracene (18)

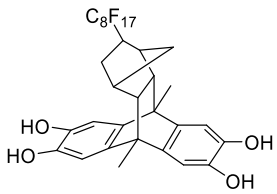

G.P.3 was followed using 2,3,6,7-tetramethoxy-9,10-(2'-heptadecafluorooctacanylbenzomethano)-9,10-dimethylanthracene (**17**) (3.1 g, 3.7 mmol) and boron tribromide (1.1 mL, 11.6 mmol) in anhydrous DCM (50 mL) to afford **18** (2.5 g, 3.2 mmol, 86 %) as a white powder. ν_{max} (cm^{-1}): 3308 (*br*), 2970, 2907, 1614, 1449, 1292, 1198,

1144, 988, 874; ^{1}H NMR (500 MHz, Acetone-d_6): δ_H (ppm) 6.76 (s, 1H), 6.75 (s, 1H), 6.72 (s, 1H), 6.72 (s, 1H), 2.47 (s, 1H), 2.25-2.08 (m, 2H), 1.80 (s, 3H), 1.80 (s, 3H), 1.71 (d, *J* = 8.6 Hz, 1H), 1.66 (d, *J* = 8.6 Hz, 1H), 1.61-1.56 (m, 1H), 1.49-1.44 (m, 1H), 0.62 (d, *J* = 10.8 Hz, 1H), -0.13 (d, *J* = 10.7 Hz, 1H); ^{13}C NMR (126 MHz, Acetone-d_6): δ_C (ppm) 143.3, 143.3, 142.7, 142.6, 140.6, 140.5, 137.3, 137.2, 122.2-116.6 (m, CF), 110.9, 110.7, 109.5, 109.2, 58.4, 56.3, 45.5, 43.4, 43.3, 39.3, 37.7, 33.4, 32.7, 17.5, 17.1; HRMS (EI, m/z): [M^+] calcd.: 782.1319, found: 782.1279.

9,10-(2'-Heptadecafluorooctacanylbenzomethano)anthracene (19)

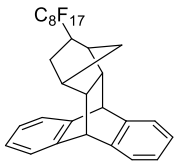

2-Heptadecafluorooctanyl-5-norbornene (**16**) (25.3 g, 15 mL, 49.3 mmol) and anthracene (8.8 g, 49.3 mmol) were added in a microwave vessel and heated in the microwave reactor at 250 °C for 4 h with a pressure of 10 bar. Purified by column chromatography (DCM) and the obtained solid was washed with hexane to afford the product **19** (21.0 g, 30.4 mmol, 62%, mixture of isotherms) as a white solid. Mp: 111-112 °C ; ν_{max} (cm^{-1}): 2945, 1460, 1369, 1196, 1148, 989, 745, 660, 557; ^{1}H NMR (500 MHz, $CDCl_3$): δ_H (ppm) 7.26-7.23 (m, 2H), 7.22-7.15 (m, 2H), 7.15-7.08 (m, 2H), 7.11-7.05 (m, 2H), 4.29 (d, *J* = 2.7 Hz, 1H),4.27 (d, *J* = 3.0 Hz, 1H), 2.46 (m, 1H), 2.10 (m, 1H), 2.05-1.94 (m, 2H), 1.93-1.82 (m, 1H), 1.65-1.55 (m, 1H), 1.46-1.36 (m, 1H), 0.69 (d, *J* = 11.3 Hz, 1H), -0.34 (d, *J* = 11.4 Hz, 1H); 7.26-7.23 (m, 2H), 7.22-7.15 (m, 2H), 7.15-7.08 (m, 2H), 7.11-7.05 (m, 2H), 4.26 (d, J = 3.0 Hz, 1H), 4.22 (d, *J* = 2.9 Hz, 1H), 2.40-2.37 (m, 1H), 2.37-2.29 (m, 1H), 2.13 (m, 1H), 2.04-1.95 (m, 2H), 1.75-1.69 (m, 1H), 1.31-1.24 (m, 1H).0.48 (d, *J* = 11.0 Hz, 1H),-0.17 (d, *J* = 11.4 Hz, 1H); ^{13}C NMR (126 MHz, $CDCl_3$): δ_C (ppm) 144.6, 144.4, 144.4, 142.6, 142.4, 141.9, 141.8, 126.7, 126.4, 126.4, 126.3, 126.2, 126.0, 125.9, 125.9, 125.8, 125.8, 125.6, 124.6, 124.5, 124.5, 124.4, 124.4, 124.0, 123.7, 123.5, 123.4, 123.4, 123.1-108.4 (m, CF), 50.32, 48.8-48.2, 46.6, 45.1 (t, *J* = 20.6 Hz), 43.1 (t, *J* = 20.1 Hz), 42.4, 42.1, 40.46, 40.2, 39.1, 34.8, 33.0, 31.8, 31.1, 29.2, 26.1, 22.8, 15.4, 14.3; HRMS (EI, m/z): [M^+] calcd.: 690.1210, found: 690.1177.

9,10-(2'-Heptadecafluorooctacanylbenzomethano)-2,(6)7-dinitroanthracene (20)

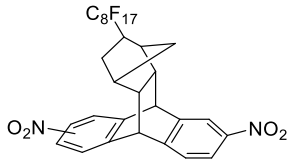

The nitration was conducted using a reported procedure.[201] 9,10-(2'-Heptadecafluorooctacanylbenzomethano)anthracene (**19**) (31.2 g, 45.2 mmol) and potassium nitrate (10.5 g, 104.1 mmol) were dissolved in the mixture of acetonitrile/DCM (700 mL, 4/1, v/v). Trifluoroacetic anhydride (66.5 g, 316.7 mmol) was added dropwise and heated at 50 °C for 24 h. The reaction mixture was extracted with DCM, washed thoroughly with saturated sodium hydrogen carbonate solution and water, and dried over $MgSO_4$. The solvent was removed under vacuum to give a yellow oil which was purified by column chromatography hexane/DCM (3/2, v/v) to afford pure dinitro product **20** (29.3 g, 37.6 mmol, 83%) as a white powder. Mp: 99-101 °C; ν_{max} (cm^{-1}): 2947, 1548, 1335, 1196, 1146, 989,745, 658, 557; ^{1}H NMR (500 MHz, $CDCl_3$): δ_H (ppm) 8.24-7.96 (m, 4H), 7.49-7.36 (m, 4H), 4.69-4.46 (m, 2H), 2.68-2.31 (m, 1.7H), 2.24 (m, 1H), 2.18-1.95 (m, 2.3H), 1.88-1.74 (m, 0.3H), 1.73-1.62 (m, 0.7H), 1.52-1.43 (m, 0.7H), 1.35-1.24 (m, 0.3H), 0.82 (d, *J* = 11.9 Hz, 0.7H), 0.62 (d, *J* = 11.5 Hz, 0.3H), -0.13 (d, *J* = 11.5 Hz, 0.3H), -0.29 (d, *J* = 11.8 Hz, 0.7H); ^{13}C NMR (126 MHz, $CDCl_3$): δ_C (ppm) 150.1, 149.6, 149.1, 148.8, 148.6, 148.3, 148.3, 147.8, 147.8, 147.1, 147.0, 147.0, 146.6, 144.6, 144.6, 144.1, 144.1, 143.2, 142.9, 142.7, 142.5, 142.5, 142.0, 141.9, 129.7-105.9 (m, CF), 49.7-46.8, 46.2, 45.2-44.9, 43.0-41.9, 40.4, 40.2-40.1, 39.2-39.0, 35.1, 32.9, 32.2, 31.7; HRMS (EI, m/z): [M+] calcd.:780.0911, found: 780.0880.

9,10-(2'-Heptadecafluorooctacanylbenzomethano)-2,(6)7-diaminoanthracene (21)

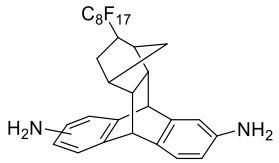

9,10-(2'-Heptadecafluorooctacanylbenzomethano)-2,(6)7-dinitroanthracene (**20**) (9.0 g, 11.5 mmol) was dissolved in a refluxing mixture of concentrated hydrochloric acid (50 mL) and ethanol (50 mL). Tin powder (4.6 g, 38.5 mmol) was added in small portions and refluxed for

24 h. After cooling, the reaction mixture was neutralised with sodium hydroxide (1 M), extracted with DCM and dried over $MgSO_4$. The solvent was removed under vacuum to afford **21** (7.7 g, 10.7 mmol, 94%, mixture of isomers) as a white powder. Mp: 85-86 °C; ν_{max} (cm^{-1}): 3460, 3347, 2924, 1624, 1481, 1362, 1202, 1142, 804, 719, 556; ^1H NMR (500 MHz, $CDCl_3$): δ_H (ppm) 7.06-6.96 (m, 1H), 6.94-6.88 (m, 2H), 6.67-6.62 (m, 2H), 6.60 (m, 2H), 6.49-6.28 (m, 2H), 4.19-3.92 (m, 2H), 3.53 (bs, 4H, NH_2), 2.51-2.32 (m, 1.7H), 2.21-1.80 (m, 3.3H), 1.79-1.53 (m, 1H), 1.45-1.24 (m, 1H), 0.74 (d, *J* = 11.1 Hz, 0.7H), 0.53 (d, *J* = 10.8 Hz, 0.3H), 0.11 (d, *J* = 11.0 Hz, 0.3H), -0.07 (d, *J* = 11.1 Hz, 0.7H).; ^{13}C NMR (126 MHz, $CDCl_3$): δ_C (ppm) 146.5, 146.3, 145.6, 145.5, 145.0, 144.7, 144.5, 144.3, 144.1, 143.6, 143.6, 142.7, 142.7, 135.9, 134.9, 133.5, 132.9, 131.9, 128.4, 125.7, 124.9-123.6 (m,CF), 118.4-108.7 (m,CF), 51.1, 50.9, 50.3, 50.3, 49.5, 49.5, 48.9-47.5, 46.8, 46.5, 46.4, 45.4-44.8, 42.9, 42.0, 40.5-40.1, 39.1, 34.9, 34.4, 33.0, 31.9, 30.5, 21.3; HRMS (EI, m/z): [M+] calcd.: 720.1428, found: 720.1416.

2-(3,4-Dimethoxybenzoyl)benzoic acid (22)

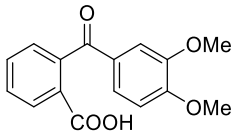

The compound 2-(3,4-dimethoxybenzoyl)benzoic acid (**22**) was synthesised according to the procedure reported by J. Veerman *et al*.[174] Veratrol (12.8 mL, 100.0 mmol) was added to a suspension of $AlCl_3$ (13.3 g, 100.0 mmol) in DCM (200 mL) at 0 °C. After this, phthalic anhydride (14.8 g, 100.0 mmol) was added in small portions. The reaction was allowed to warm to room temperature and stirring for 1 h, and then refluxed overnight. Upon cooling the reaction mixture was poured into ice/water. The precipitate was filtered off and washed with DCM to afford the product **22** (8.2 g, 28.6 mmol, 29%) as a white solid. Mp: 239-240 °C; ν_{max} (cm^{-1}): 3127 (*br*), 1713, 1628, 1574, 1508, 1449, 1418, 1391, 1296, 1233, 1132, 1074, 1020, 984, 883, 843, 752, 710, 648; ^1H NMR (400 MHz, Acetone-d_6): δ_H (ppm) 8.13-8.01 (m, 1H, Ar *H*), 7.73 (dt, *J* = 7.5, 1.4 Hz, 1H), 7.65 (dt, *J* = 7.6, 1.4 Hz, 1H), 7.47 (d, *J* = 2.0 Hz, 1H), 7.44-7.37 (m, 1H), 7.08 (dd, *J* = 8.4, 2.0 Hz, 1H), 6.96 (d, *J* = 8.4 Hz, 1H), 3.87 (s, 3H), 3.85 (s, 3H); ^{13}C NMR (126 MHz, Acetone-d_6): δ_C (ppm) 194.7, 166.3, 153.7, 149.4, 142.6, 132.2, 130.6, 130.0, 129.7, 129.2, 127.7, 124.6, 110.8, 110.4, 55.3, 55.2; HRMS (EI, m/z): [M^+] calcd.:286.0836, found:286.0835.

2,3-Dimethoxy-9,10-anthraquinone (23)

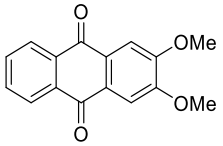

2-(3,4-Dimethoxybenzoyl)benzoic acid (**22**) (45.0 g, 157.0 mmol) was added into methanesulfonic acid (400 mL) and reacted at 70 °C for 24 h. After cooling, the solution was poured into ice/water and neutralized with sodium hydroxide solution (2 M). The precipitate was collected by filtration and washed with acetone to afford the product **23** (32.0 g, 119.0 mmol, 76%) a as yellow solid. Mp: 243-244 °C; ν_{max} (cm^{-1}): 2995, 1657, 1572, 1512, 1452, 1373, 1327, 1308, 1223, 1103, 1082, 1001, 962, 885, 775, 710, 613; ^{1}H NMR (400 MHz, $CDCl_3$): δ_H (ppm) 8.28 (dd, *J* = 5.8, 3.3 Hz, 2H), 7.76 (dd, *J* = 5.8, 3.3 Hz, 2H), 7.73 (s, 2H), 4.07 (s, 12H); ^{13}C NMR (126 MHz, $CDCl_3$): δ_C (ppm) 182.5, 153.9, 133.7, 133.6, 128.5, 127.0, 108.4, 56.6; LC-MS (m/z): $[M+H]^+$ calcd.: 269.1, found: 269.1.

2,3-Dimethoxyanthracene (24)

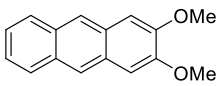

The compound 2,3-dimethoxyanthracene (**24**) was prepared according to the procedure reported by Pozzo *et al.*[202] 2,3-Dimethoxy-9,10-anthraquinone (**23**) (8.0 g, 29.8 mmol) was dispersed into isopropanol (600 mL). Sodium borohydride (12.0 g, 298.0 mmol) was added in small portions and then refluxed under nitrogen for 48 h. After cooling, the reaction mixture was poured into ice/water, quenched with hydrochloric acid (35%), and extracted with DCM. The organic layer was washed with sodium hydroxide solution (1 M), water and dried over $MgSO_4$. The solvent was removed under vacuum. The resulted solid was reduced with sodium borohydride (12.0 g, 298.0 mmol) again. After the same work up, the crude product was purified by recrystallization from ethyl acetate to afford **24** (5.4 g, 22.6 mmol, 76%) as white crystal. Mp: 210-211 °C; ν_{max} (cm^{-1}): 2974, 1630, 1564, 1489, 1466, 1449, 1431, 1283, 1261, 1211, 1152, 1011, 885, 748, 581; ^{1}H NMR (400 MHz, $CDCl_3$): δ_H (ppm) 8.22 (s, 2H), 7.97-7.89 (m, 2H), 7.43-7.37 (m, 2H), 7.20 (s, 2H), 4.05 (s, 6H); ^{13}C NMR (126 MHz, $CDCl_3$): δ_C (ppm)

150.1, 130.9, 128.6, 127.7, 124.6, 124.0, 104.9, 55.9; LC-MS (m/z): $[M+H]^+$ calcd.: 239.1, found: 239.2.

2,3,9,10-Tetramethoxy-5,14,7,12-dibenzeno-5,5a,6,6a,7,12,12a,13,13a,14-decahydro-6,13-methanopentacene (Tetramethoxy-DBMP) (25a)

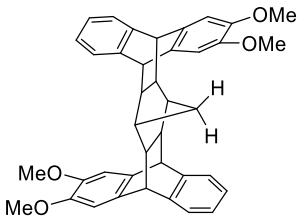

G.P.2 was followed using 2,3-dimethoxyanthracene (**24**) (3.0 g, 12.6 mmol) and norbornadiene (0.6 mL, 6.3 mmol) in xylene (5.0 mL). Purification by silica gel column chromatography to separate three isomers and afford **25a** (1.2 g, 2.1 mmol, 17%) as an off-white solid. Mp: 193-194 °C; ν_{max} (cm^{-1}): 2926, 1610, 1497, 1466, 1288, 1217, 1188, 1094, 1020, 984, 739, 642; ^1H NMR (601 MHz, $CDCl_3$): δ_H (ppm) 7.18 – 7.13 (m, 2H), 7.09 – 7.04 (m, 2H), 7.03 – 6.97 (m, 4H), 6.79 (s, 2H), 6.67 (s, 2H), 4.09 (s, 2H), 4.07 (s, 2H), 3.81 (s, 6H), 3.79 (s, 6H), 1.88 (s, 2H), 1.74 (s, 2H), 1.72 (s, 2H), -0.92 (d, J = 11.9 Hz, 1H), -1.00 (d, J = 11.9 Hz, 1H); ^{13}C NMR (101 MHz, CD_3Cl): δ_C (ppm) 147.1, 146.6, 145.3, 142.8, 137.4, 134.4, 125.9, 125.4, 123.8, 122.8, 108.9, 108.1, 56.3, 56.3, 51.5, 51.1, 48.2, 48.2, 43.3, 27.3; HRMS (EI, m/z): $[M^+]$ calcd.: 568.2608, found: 568.2581.

2,3,9,10-Tetrahydroxy-5,14,7,12-dibenzeno-5,5a,6,6a,7,12,12a,13,13a,14-decahydro-6,13-methanopentacene (DBMP-a)

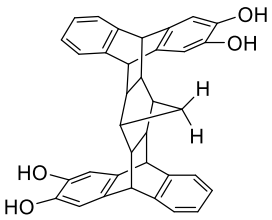

G.P.4 was followed using 2,3,9,10-tetramethoxy-5,14,7,12-dibenzeno-5,5a,6,6a,7,12,12a,13,13a,14-decahydro-6,13-methanopentacene (**25**) (1.5 g, 2.6 mmol) and boron tribromide (0.75 mL, 7.8 mmol) was dissolved in anhydrous DCM (25 mL) to afford **DBMP-a** (1.0 g, 2.0 mmol, 74 %) as a white solid. ν_{max} (cm^{-1}): 3343 (*br*), 1699, 1651, 1609, 1499, 1456, 1296, 1148, 1072, 874, 920, 741, 646, 588; ^{1}H NMR (500 MHz, DMSO-d_6): δ_H (ppm) 8.41 (s, 2H), 8.40 (s, 2H), 7.18 – 7.09 (m, 2H), 7.07 – 6.99 (m, 2H), 7.00 – 6.88 (m, 4H), 6.60 (s, 2H), 6.47 (s, 2H), 3.97 (s, 4H), 1.72 (s, 2H), 1.58 (s, 2H), 1.52 (s, 2H), -1.15 (d, J = 11.5 Hz, 1H), -1.24 (d, J = 11.2 Hz, 1H); ^{13}C NMR (101 MHz, DMSO-d_6): δ_C (ppm) 145.4, 143.2, 142.5, 141.9, 135.5, 132.6, 125.3, 124.8, 123.4, 122.6, 112.5, 111.5, 50.8, 50.3, 46.7, 46.6, 42.6; HRMS (EI, m/z): [M^+] calcd.:512.1982, found: 512.1978.

7.3 Polymer synthesis

General procedure for the synthesis of polybenzodioxin polymers (G.P.P.1)

The polybenzodioxin polymers were synthesized according to the method reported by Ian *et al*.[141] The required biscatechol (1.00 eq.) and tetrafluoroterephthalonitrile (1.00 eq.) were dissolved in anhydrous DMF. After dissolved absolutely, K_2CO_3 (8.00 eq.) was added and heated at 65 °C for 72 h. After this time, polymer solution was poured into water, acidified with conc. HCl. The precipitate was collected by filtration and washed repeatedly with water, acetone and methanol, and dried in the vacuum oven. Polymers were dissolved in required solvents and reprecipitated by adding acetone/methanol (2/1, v/v), then filtered off to remove oligomers. The obtained polymers were refluxed in methanol for 24 h and dried under vacuum at 100 °C for 24 h.

PIM-TFM-BTrip

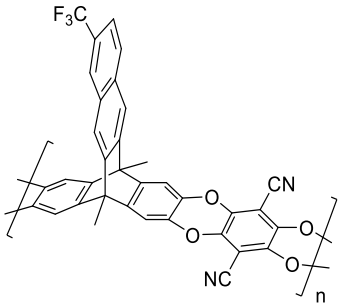

Following the general procedure (**G.P.P.1**), 2,3,6,7-tetrahydroxy-9,10-dimethyl-15-trifluoromethylbenzotriptycene (**8**) (1.80 g, 3.87 mmol) and 2,4,5,6-tetrafluoroterephthalonitrile (0.77 g, 3.87 mmol), K_2CO_3 (4.27 g, 30.93 mmol) and anhydrous DMF (40.0 mL) were combined to afford the desired polymer **PIM-TFM-BTrip** (1.97 g, 79%) as a yellow powder. ν_{max} (cm^{-1}): 2974, 2241, 1439, 1329, 1294, 1269, 1186, 1163, 1124, 1067, 1005, 885; ^{13}C NMR (101 MHz, solid state): δ_C (ppm) 145.4, 138.3, 132.8, 130.8, 127.8, 119.8, 109.7, 94.8, 48.0, 12.9; BET surface area = 848 m^2/g; total pore volume = 0.66 mL/g at P/P_o = 0.98 from N_2 adsorption at 77 K; TGA analysis (nitrogen): 520 °C (onset temperature of decomposition).

PIM-DTFM-BTrip

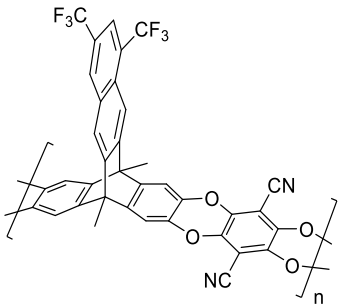

Following the general procedure (**G.P.P.1**), 2,3,6,7-tetrahydroxy-9,10-dimethyl-12,14-bis(trifluoromethyl)benzotriptycene (**9**) (2.16 g, 4.05 mmol), 2,4,5,6-tetrafluoroterephthalonitrile (0.81 g, 4.05 mmol), K_2CO_3 (4.48 g, 32.40 mmol) and anhydrous DMF (57.0 mL) were combined to afford **PIM-DTFM-BTrip** (2.42 g, 84%) as a yellow powder.

ν_{max} (cm^{-1}): 2980, 2241, 1439, 1298, 1271, 1206, 1188, 1161, 1128, 1088, 1007, 905, 885, 671; ^{13}C NMR (101 MHz, solid state): δ_C (ppm) 145.4, 138.3, 132.0, 128.3, 122.1, 120.4, 114.6, 109.8, 94.8, 48.1, 12.5; BET surface area = 964 m^2/g; total pore volume = 1.02 mL/g at P/P_o = 0.98 from N_2 adsorption at 77 K; TGA analysis (nitrogen): 534 °C (onset temperature of decomposition).

PIM-OCF

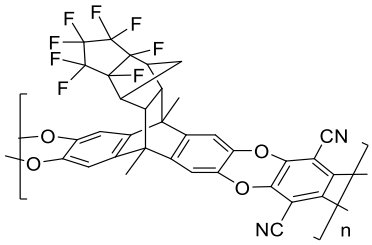

Following the general procedure (**G.P.P.1**), 2,3,6,7-tetrahydroxyl-9,10-(4',7'-methano-1',1',2',2',3',3',3a,7a-octafluoro-1'H-perhydroindenyl)-9,10-dimethylanthracene (**14**) (2.18 g, 3.97 mmol), 2,4,5,6-tetrafluoroterephthalonitrile (0.7937 g, 3.97 mmol), K_2CO_3 (4.39 g, 31.77 mmol) and anhydrous DMF (34.0 mL) were combined to afford **PIM-OCF** (2.09 g, 79%) as a yellow powder. ν_{max} (cm^{-1}):2974, 2243, 1605, 1441, 1310, 1269, 1188, 1161, 1007, 891; ^1H NMR (500 MHz, THF-d_8): δ_H (ppm) 7.15 (*bs*,2H), 7.11 (*bs*, 2H), 2.98 (*bs*, 2H), 2.48 (*bs*, 2H), 1.99 (*bs*, 6H), 0.87 (*bs*, 1H), 0.37 (*bs*, 1H); ^{13}C NMR (75 MHz, solid state): δ_C (ppm) 142.8, 138.3, 109.7, 94.3, 45.1, 42.5, 40.6, 25.1, 13.6; BET surface area = 929 m^2/g; total pore volume = 0.74 mL/g at P/P_o = 0.98 from N_2 adsorption at 77 K; TGA analysis (nitrogen): 300 °C (onset temperature of decomposition).

PIM-OCP

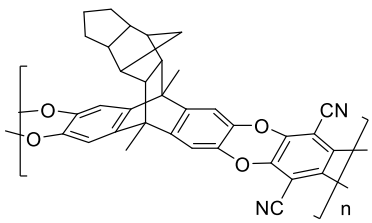

Following the general procedure (**G.P.P.1**), 2,3,6,7-tetrahydroxyl-9,10-(4',7'-methano-1'H-perhydroindenyl)-9,10-dimethylanthracene (**15**) (0.69 g, 1.71 mmol), 2,4,5,6-

tetrafluoroterephthalonitrile (0.34 g, 1.17 mmol), K_2CO_3 (1.89 g, 13.68 mmol) and anhydrous DMF (13.0 mL) were combined to afford the polymer **PIM-OCP** (2.09 g, 79%) as a yellow powder; ν_{max} (cm^{-1}):2943, 2239, 1605, 1441, 1269, 1005, 955, 881, 752; ^{13}C NMR (75 MHz, solid state) δ_C (ppm): 141.5, 137.3, 108.8, 93.8, 55.7, 49.3, 46.9, 42.8, 30.2, 25.7, 14.5; BET surface area = 1062 m^2/g; total pore volume = 0.82 mL/g at P/P_o = 0.98 from N_2 adsorption at 77 K; TGA analysis (nitrogen): 309 °C (onset temperature of decomposition).

PIM-C8F17

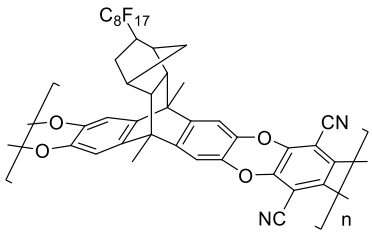

Following the general procedure (**G.P.P.1**), 2,3,6,7-tetrahydroxyl-9,10-(2'-heptadecafluorooctacanylbenzomethano)-9,10-dimethylanthracene (**18**) (2.39 g, 3.06 mmol), tetrafluoroterephthalonitrile (0.61 g, 3.06 mmol), K_2CO_3 (3.38 g, 24.48 mmol) and anhydrous DMF (35.0 mL) were combined to afford **PIM-C8F17** as yellow powder (2.57 g, 93%). ν_{max} (cm^{-1}): 2970, 2908, 2241, 1441, 1275, 1206, 1148, 1007, 883; BET surface area = 569 m^2/g; total pore volume = 0.62 mL/g at P/P_o = 0.98 from N_2 adsorption at 77 K; TGA analysis (nitrogen): 319 °C (onset temperature of decomposition).

PIM-C8F17-TB

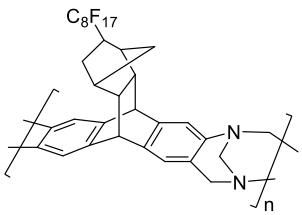

Tröger's Base (TB) polymers were synthesised according to the method reported by Carta *et al*.[1] 9,10-(2'-Heptadecafluorooctacanylbenzomethano)-2,(6)7-diaminoanthracene (**21**) (2.50

g, 3.47 mmol) was dissolved in dimethoxymethane (DMM, 1.54 mL, 1.32 g, 17.35 mmol) and cooled to 0 °C. Trifluoroacetic acid (TFA, 6.1 mL, 9.03 g, 79.18 mmol) was added slowly and then stirred at room temperature until a desired viscous solution formed. The reaction was quenched with aqueous ammonium solution and filtered off to collect the precipitate. The precipitate was washed thoroughly with water, acetone and methanol. The resulting powder was dried in the oven, dissolved in HFIP and reprecipitated from methanol. The reprecipitation was repeated twice. Polymer was dissolved in HFIP and added dropwise into hexane. Resulting polymer was filtered off, refluxed in methanol for 24 h and oven dried at 100 °C for 24 h to afford **PIM-C8F17-TB** (2.49 g, 95%) as off-white powder. ν_{max} (cm^{-1}): 2938, 1470, 1422, 1358, 1120, 1148, 937, 719, 654; BET surface area = 25 m^2/g total pore volume = 0.22 mL/g at P/P_o = 0.98 from N_2 adsorption at 77 K; TGA analysis (nitrogen): 327 °C (onset temperature of decomposition).

PIM-DBMP-1

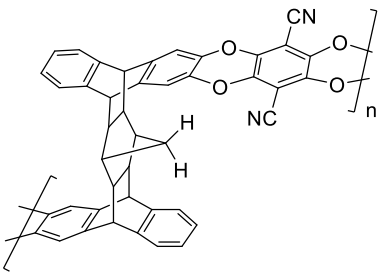

Following the general procedure (**G.P.P.1**), DBMP-a (**26**) (1.13 g, 2.20 mmol), tetrafluoroterephthalonitrile (0.44 g, 2.20 mmol), K_2CO_3 (2.43 g, 17.59 mmol) and anhydrous DMF (19 mL) were combined to afford the polymer **PIM-DBMP-1** as a yellow powder (1.29 g, 93%). ν_{max} (cm^{-1}): 2930, 2238, 1607, 1443, 1277, 1190, 1144, 1007, 878, 739, 646; ^{13}C NMR (75 MHz, solid state) δ (ppm) 141.9, 125.6, 112.5, 96.2, 49.0, 43.8, 26.9.; BET surface area = 789 m^2/g; total pore volume = 0.57 mL/g at P/P_o = 0.98 from N_2 adsorption at 77 K; TGA analysis (nitrogen): 361 °C (onset temperature of decomposition).

PIM-DBMP-2

Following the general procedure, DBMP-b and DBMP-c (isotherms of **26**) (2.37 g, 4.63 mmol), tetrafluoroterephthalonitrile (0.93 g, 4.63 mmol), K_2CO_3 (5.12 g, 37.04 mmol) and anhydrous DMF (51 mL) were combined to afford the polymer **PIM-DBMP-2** as a yellow powder (2.79 g, 95%). BET surface area = 875 m^2/g; total pore volume = 0.64 mL/g at P/P_o = 0.98 from N_2 adsorption at 77 K;

PIM-DBMP-*co*-TTSBI copolymers

PIM-DBMP-*co*-TTSBI (90:10)

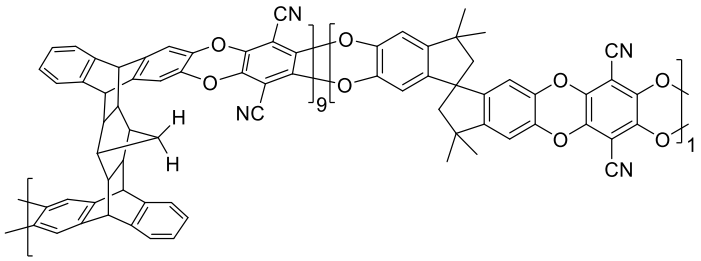

Following the general procedure (**G.P.P.1**), DBMP (2.12 g, 4.14 mmol), 5,5′,6,6′-tetrahydroxy-3,3,3′,3′-tetramethylspirobisindane (TTSBI) (0.16 g, 0.46 mmol), tetrafluoroterephthalonitrile (TTFPN) (0.92 g, 4.6 mmol), K_2CO_3 (2.54 g, 18.4 mmol) and anhydrous DMF (35.0 mL) were combined to afford **PIM-DBMP-*co*-TTSBI (90:10)** as a yellow powder (2.38 g, 82 %). ν_{max} (cm^{-1}): 2934, 2241, 1607, 1445, 1279, 1144, 1007, 878, 739, 648; BET surface area = 728 m^2/g; total pore volume = 0.54 mL/g at P/P_o = 0.98 from N_2 adsorption at 77 K; TGA analysis (nitrogen): 358 °C (onset temperature of decomposition).

PIM-DBMP-*co*-TTSBI (75:25)

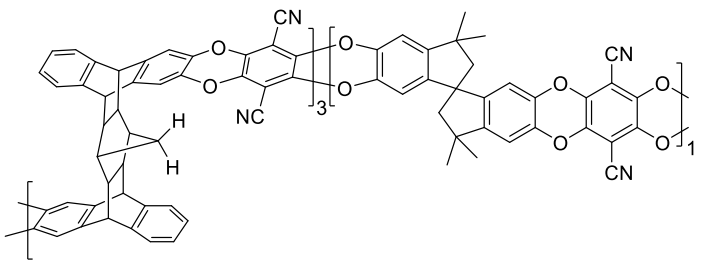

Following the general procedure, DBMP (1.00 g, 1.96 mmol), 5,5',6,6'-tetrahydroxy-3,3,3',3'-tetramethylspirobisindane (TTSBI) (0.22 g, 0.65 mmol), tetrafluoroterephthalonitrile (TTFPN) (0.52 g, 2.61 mmol), K_2CO_3 (1.44 g, 10.44 mmol) and anhydrous DMF (12.0 mL) were combined to afford **PIM-DBMP-*co*-TTSBI (75:25)** as yellow powder (1.21 g, 77%). ν_{max} (cm^{-1}): 2934, 2241, 1607, 1445, 1279, 1144, 1007, 878, 739, 648; BET surface area = 728 m^2/g; total pore volume = 0.54 mL/g at P/P_o = 0.98 from N_2 adsorption at 77 K; TGA analysis (nitrogen): 358 °C (onset temperature of decomposition).

PIM-DBMP-*co*-TTSBI (50:50)

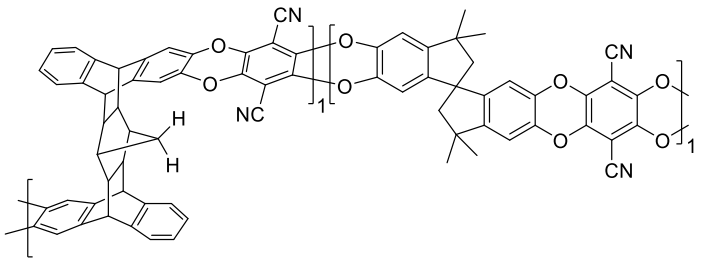

Following the general procedure, DBMP (0.84 g, 1.65 mmol), 5,5',6,6'-tetrahydroxy-3,3,3',3'-tetramethylspirobisindane (TTSBI) (0.56 g, 1.65 mmol), tetrafluoroterephthalonitrile (TTFPN) (0.66 g, 3.30 mmol), K_2CO_3 (1.82 g, 13.19 mmol) and anhydrous DMF (15.0 mL) were combined to afford **PIM-DBMP-*co*-TTSBI (50:50)** as yellow powder (1.23 g, 80%). ν_{max} (cm^{-1}):2932, 2241, 1608, 1443, 1277, 1211, 1144, 1007, 878, 741, 648; ^1H NMR (500 MHz, $CDCl_3$) δ_H (ppm) 7.19-6.97 (m, 8H), 6.90-6.62 (m, 6H), 6.40 (s, 2H), 4.09 (s, 4H), 2.34 (s, 2H), 2.17 (s, 2H), 1.92 (s, 2H), 1.72 (s, 4H) 1.49-1.09 (m, 6H), -0.79 (s, 1H), -0.96 (s, 1H); ^{13}C NMR (126 MHz, $CDCl_3$): δ_C (ppm) 149.94, 147.09, 143.70, 142.41, 141.25, 139.35, 137.58, 137.07, 126.29, 124.35, 123.29, 112.61, 110.58, 109.19, 94.27, 59.03, 57.27, 50.46, 47.67, 43.74, 43.16, 31.49, 30.04; BET surface area = 830 m^2/g; total pore volume = 0.67 mL/g at P/P_o = 0.98 from N_2 adsorption at 77 K; TGA analysis (nitrogen): 355 °C (onset temperature of decomposition).

PIM-DBMP-*co*-TTSBI (25:75)

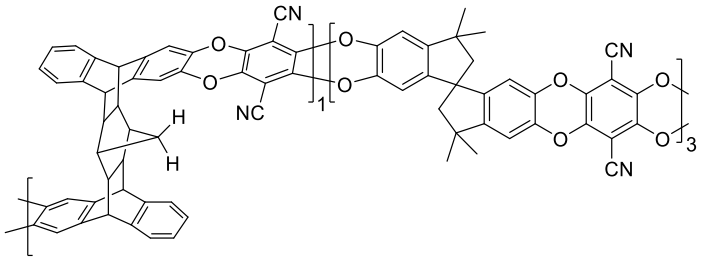

Following the general procedure, DBMP (0.51 g, 1.00 mmol), 5,5',6,6'-tetrahydroxy-3,3,3',3'-tetramethylspirobisindane (TTSBI) (1.02 g, 3 mmol), tetrafluoroterephthalonitrile (TTFPN) (0.80 g, 4.00 mmol), K_2CO_3 (4.42 g, 32.00 mmol) and anhydrous DMF (15.0 mL) were combined to afford **PIM-DBMP-*co*-TTSBI (25:75)** as yellow powder (1.62 g, 76%). ν_{max} (cm^{-1}): 2955, 2241, 1485, 1445, 1310, 1265, 1211, 1146, 1107, 1009, 876, 754, 741; ^1H NMR (400 MHz, $CDCl_3$) δ_H (ppm) 7.21-6.95 (m, 8H), 6.89-6.66 (m, 10H), 6.41 (s, 6H), 4.10 (s, 4H), 2.33 (s, 6H), 2.17 (s, 6H), 1.92 (s, 2H), 1.72 (s, 4H), 1.46-1.08 (m, 36H), -0.79 (s, 1H), -0.96 (s, 1H); ^{13}C NMR (126 MHz, $CDCl_3$) δ_C (ppm) 149.82, 147.07, 143.69, 142.39, 141.25, 139.61, 139.45, 139.31, 137.54, 137.04, 126.06, 124.29, 123.32, 112.42, 110.66, 109.46, 94.22, 58.96, 57.27, 50.59, 47.65, 43.71, 43.16, 31.47, 30.04; BET surface area = 759 m^2/g; total pore volume = 0.62 mL/g at P/P_o = 0.98 from N_2 adsorption at 77 K; TGA analysis (nitrogen): 353 °C (onset temperature of decomposition).

PIM-DBMP-*co*-TTSBI (10:90)

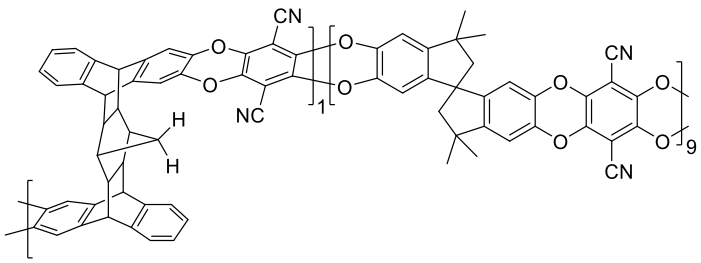

Following the general procedure, DBMP (0.20 g, 0.39 mmol), 5,5',6,6'-tetrahydroxy-3,3,3',3'-tetramethylspirobisindane (TTSBI) (1.20 g, 3.51 mmol), tetrafluoroterephthalonitrile (TTFPN) (0.78 g, 3.90 mmol), K_2CO_3 (4.31 g, 31.21 mmol) and anhydrous DMF (15.0 mL) were

combined to afford **PIM-DBMP-*co*-TTSBI (10:90)** as yellow powder (1.54 g, 78%). ν_{max} (cm^{-1}): 2955, 2238, 1607, 1447, 1310, 1287, 1263, 1211, 1107, 1009, 876, 754; ^{1}H NMR (400 MHz, $CDCl_3$): δ_H (ppm) 7.17-6.99 (m, 8H), 6.81 (s, 22H), 6.42 (s, 18H), 4.10 (s, 4H), 2.40-2.26 (m, 18H), 2.16 (m, 18H), 1.93 (s, 2H), 1.72 (s, 4H), 1.49-1.05 (m, 108H), -0.78 (s, 1H), -0.95 (s, 1H); ^{13}C NMR (126 MHz, $CDCl_3$): δ_C (ppm) 149.83, 147.05, 143.69, 142.39, 141.25, 139.61, 139.46, 139.34, 137.54, 137.04, 126.06, 124.29, 123.32, 112.44, 110.66, 109.52, 94.25, 58.96, 57.29, 50.67, 47.79, 43.72, 43.16, 31.49, 30.07; BET surface area = 801 m^2/g; total pore volume = 0.66 mL/g at P/P_o = 0.98 from N_2 adsorption at 77 K; TGA analysis (nitrogen): 389 °C (onset temperature of decomposition).

AO-PIM-DBMP (NMP)

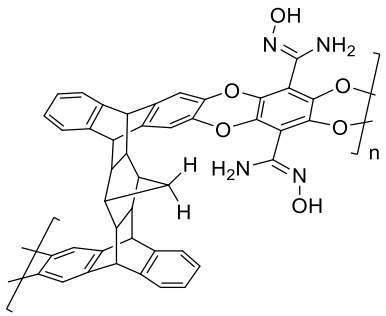

PIM-DBMP (0.5 g) was dispersed into NMP (50 mL) and heated to 65 °C. Hydroxylamine (5 mL) was added slowly and reacted at 65 °C for 72 h. After cooling, the reaction mixture was poured into ethanol, filtered off and refluxed in ethanol for 12 h. At last, the product was collected by filtration and dried under vacuum oven at 100 °C. Amidoxime PIM-DBMP was obtained as an off white powder in a 93% yield. ν_{max} (cm^{-1}): 3615, 3476, 3556, 2932, 1647, 1433, 1285, 1148, 995, 935, 743; ^{13}C NMR (75 MHz, solid state) δ_C (ppm) 141.6, 125.1, 112.5, 48.1, 43.5, 27.1.; BET surface area = 645 m^2/g; total pore volume = 0.38 mL/g at P/P_o = 0.98 from N_2 adsorption at 77 K; TGA analysis (nitrogen): 267 °C (onset temperature of decomposition).

Bibliography

1. M. Carta, R. Malpass-Evans, M. Croad, Y. Rogan, J. C. Jansen, P. Bernardo, F. Bazzarelli and N. B. McKeown, *Science*, 2013, **339**, 303-307.
2. S. Wang, X. Li, H. Wu, Z. Tian, Q. Xin, G. He, D. Peng, S. Chen, Y. Yin, Z. Jiang and M. D. Guiver, *Energy & Environmental Science*, 2016, **9**, 1863-1890.
3. S. Alexander Stern, *Journal of Membrane Science*, 1994, **94**, 1-65.
4. R. W. Baker, *Industrial & Engineering Chemistry Research*, 2002, **41**, 1393-1411.
5. E. D. P. Bernardo and G. Golemme, *Industrial & Engineering Chemistry Research*, 2009, **48**, 4638-4663.
6. P. M. Budd and N. B. McKeown, *Polymer Chemistry*, 2010, **1**, 63-68.
7. D. Reinares-Fisac, L. M. Aguirre-Diaz, M. Iglesias, N. Snejko, E. Gutierrez-Puebla, M. A. Monge and F. Gandara, *Journal of the American Chemical Society*, 2016, **138**, 9089-9092.
8. H. J. Mackintosh, P. M. Budd and N. B. McKeown, *Journal of Materials Chemistry*, 2008, **18**, 573-578.
9. N. B. McKeown, B. Gahnem, K. J. Msayib, P. M. Budd, C. E. Tattershall, K. Mahmood, S. Tan, D. Book, H. W. Langmi and A. Walton, *Angewandte Chemie International Edition*, 2006, **45**, 1804-1807.
10. A. Zecchina, S. Bordiga, J. G. Vitillo, G. Ricchiardi, C. Lamberti, G. Spoto, M. Bjørgen and K. P. Lillerud, *Journal of the American Chemical Society*, 2005, **127**, 6361-6366.
11. X. Zhao, B. Xiao, A. J. Fletcher, K. M. Thomas, D. Bradshaw and M. J. Rosseinsky, *Science*, 2004, **306**, 1012-1015.
12. J. Rouquerol, D. Avnir, C. Fairbridge, D. Everett, J. Haynes, N. Pernicone, J. Ramsay, K. Sing and K. Unger, *Pure and Applied Chemistry*, 1994, **66**, 1739-1758.
13. D. A. J. Rouquerol, C. W. Fairbridge, D. H. Everett, J. M. Haynes, N. Pernicone, J. D. F. Ramsay, K. S. W. Sing and K. K. Unger, *Pure Applied Chemistry*, 1994, **66**, 1739-1758.
14. P. Klobes, Meyer, K., and Munro, R. G., *NIST Recommended Practice Guide*, NIST, 2006.
15. S. Brunauer, P. H. Emmett and E. Teller, *Journal of the American Chemical Society*, 1938, **60**, 309-319.
16. I. Langmuir, *Journal of the American Chemical Society*, 1916, **38**, 2221-2295.
17. K. S. Sing, *Pure and Applied Chemistry*, 1985, **57**, 603-619.
18. D. R. Paul and Y. P. Yampol'skii, *Polymeric gas separation membranes*, CRC press, 1993.
19. R. W. Baker, *Membrane Technology and Applications*, John Wiley & Sons Ltd, 2004, 96-103.
20. D. S. Sholl and R. P. Lively, *Nature*, 2016, **532**, 435-437.
21. W. J. Koros and R. P. Lively, *AIChE Journal*, 2012, **58**, 2624-2633.
22. R. Baker and I. Blume, *Chemtech*, 1986, **16**, 232-238.
23. B. Freeman, Y. Yampolskii and I. Pinnau, *Materials science of membranes for gas and vapor separation*, John Wiley & Sons, 2006.
24. L. M. Robeson, *Journal of Membrane Science*, 1991, **62**, 165-185.
25. B. D. Freeman, *Macromolecules*, 1999, **32**, 375-380.
26. L. M. Robeson, *Journal of Membrane Science*, 2008, **320**, 390-400.
27. R. Swaidan, B. Ghanem and I. Pinnau, *ACS Macro Letters*, 2015, **4**, 947-951.
28. Z.-X. Low, P. M. Budd, N. B. McKeown and D. A. Patterson, *Chemical Reviews*, 2018, **118**, 5871-5911.

29. R. Swaidan, B. Ghanem, E. Litwiller and I. Pinnau, *Macromolecules*, 2015, **48**, 6553-6561.
30. L. M. Robeson, W. F. Burgoyne, M. Langsam, A. C. Savoca and C. F. Tien, *Polymer*, 1994, **35**, 4970-4978.
31. Y. Huang and D. R. Paul, *Polymer*, 2004, **45**, 8377-8393.
32. X. Ma and I. Pinnau, *Macromolecules*, 2018, **51**, 1069-1076.
33. Y. Huang and D. R. Paul, *Industrial & Engineering Chemistry Research*, 2007, **46**, 2342-2347.
34. X. Ma, R. Swaidan, Y. Belmabkhout, Y. Zhu, E. Litwiller, M. Jouiad, I. Pinnau and Y. Han, *Macromolecules*, 2012, **45**, 3841-3849.
35. M. Wessling, S. Schoeman, T. van der Boomgaard and C. A. Smolders, *Gas Separation & Purification*, 1991, **5**, 222-228.
36. D. F. Sanders, Z. P. Smith, R. Guo, L. M. Robeson, J. E. McGrath, D. R. Paul and B. D. Freeman, *Polymer*, 2013, **54**, 4729-4761.
37. Y. Xiao, B. T. Low, S. S. Hosseini, T. S. Chung and D. R. Paul, *Progress in Polymer Science*, 2009, **34**, 561-580.
38. J. D. Wind, C. Staudt-Bickel, D. R. Paul and W. J. Koros, *Macromolecules*, 2003, **36**, 1882-1888.
39. B. Kraftschik and W. J. Koros, *Macromolecules*, 2013, **46**, 6908-6921.
40. N. Du, H. B. Park, G. P. Robertson, M. M. Dal-Cin, T. Visser, L. Scoles and M. D. Guiver, *Nature Materials*, 2011, **10**, 372-375.
41. Y. Xiao, T.-S. Chung, H. M. Guan and M. D. Guiver, *Journal of Membrane Science*, 2007, **302**, 254-264.
42. N. Du, M. M. Dal-Cin, G. P. Robertson and M. D. Guiver, *Macromolecules*, 2012, **45**, 5134-5139.
43. R. Swaidan, B. S. Ghanem, E. Litwiller and I. Pinnau, *Journal of Membrane Science*, 2014, **457**, 95-102.
44. R. Guo and J. E. McGrath, *Polymer Science: A Comprehensive Reference*, 2012, **5**, 377-430.
45. N. Jusoh, K. K. Lau and A. M. Shariff, *Advanced Materials Research*, 2014, **917**, 307-316.
46. F. V. Adams, E. N. Nxumalo, R. W. M. Krause, E. M. V. Hoek and B. B. Mamba, *Journal of Membrane Science*, 2012, **405**, 291-299.
47. T. M. Henis JS, *US Patent* 4230463, 1977.
48. C. L. Aitken, W. J. Koros and D. R. Paul, *Macromolecules*, 1992, **25**, 3424-3434.
49. C. L. Aitken, W. J. Koros and D. R. Paul, *Macromolecules*, 1992, **25**, 3651-3658.
50. J. S. McHattie, W. J. Koros and D. R. Paul, *Polymer*, 1992, **33**, 1701-1711.
51. J. S. McHattie, W. J. Koros and D. R. Paul, *Polymer*, 1991, **32**, 840-850.
52. T. Heinze and T. Liebert, *Macromolecular Symposia*, 2004, **208**, 167-238.
53. W. N. R. Jami'an, H. Hasbullah, F. Mohamed, N. Yusof, N. Ibrahim and R. R. Ali, *IOP Conference Series: Earth and Environmental Science*, 2016, **36**, 012008.
54. B. S. Minhas, T. Matsuura and S. Sourirajan, *Industrial & Engineering Chemistry Research*, 1987, **26**, 2344-2348.
55. A. C. Puleo, D. R. Paul and S. S. Kelley, *Journal of Membrane Science*, 1989, **47**, 301-332.
56. Y. W. J. Seo-Hyun Pak, Myung-Seop Shin, and Hyung Chul Koh, *Environmental Engineering Science*, 2016, **33**, 17-24.
57. M. J. K. D. Mahoney, *US Patent*, US4276173A, 1978.
58. X. He, *Membranes*, 2017, **7**, 27.
59. S. Saka, *Macromolecular Symposia*, 2004, **208**, 7-28.

60. C. A. Scholes, G. W. Stevens and S. E. Kentish, *Fuel*, 2012, **96**, 15-28.
61. J. Hennessy and A. LivingstonBaker, *Nature Materials*, 2017, **16**, 280-282.
62. H. Sanaeepur, B. Nasernejad and A. Kargari, *Greenhouse Gases: Science and Technology*, 2015, **5**, 291-304.
63. H. Sanaeepur, A. Kargari, B. Nasernejad, A. Ebadi Amooghin and M. Omidkhah, *Journal of the Taiwan Institute of Chemical Engineers*, 2016, **60**, 403-413.
64. X. F. Zhang, Y. Feng, Z. Wang, M. Jia and J. Yao, *Journal of Membrane Science*, 2018, **568**, 10-16.
65. M. Mubashir, Y. F. Yeong, K. K. Lau, T. L. Chew and J. Norwahyu, *Separation and Purification Technology*, 2018, **199**, 140-151.
66. H. Sanaeepur, A. Kargari and B. Nasernejad, *RSC Advances*, 2014, **4**, 63966-63976.
67. X. l. Fu, M. Zeng, J.-b. Zhou and C. Xu, *RSC Advances*, 2017, **7**, 41070-41076.
68. W.-g. Kim, J. S. Lee, D. G. Bucknall, W. J. Koros and S. Nair, *Journal of Membrane Science*, 2013, **441**, 129-136.
69. C. Liu, Wilson, Stephen T., Chiou, Jeffrey J., Lesch, David A., Kulprathipanja, Santi, *US Patent*, US20100326273, 2010.
70. G. Chowdhury, B. Kruczek, T. Matsuura, *Polyphenylene Oxide and Modified Polyphenylene Oxide Membranes : Gas, Vapor, and Liquid Separation*, Springer, 2001.
71. A. S. Hay, H. S. Blanchard, G. F. Endres and J. W. Eustance, *Journal of the American Chemical Society*, 1959, **81**, 6335-6336.
72. W. J. Koros, G. K. Fleming, S. M. Jordan, T. H. Kim and H. H. Hoehn, *Progress in Polymer Science*, 1988, **13**, 339-401.
73. M. Aguilar-Vega and D. R. Paul, *Journal of Polymer Science Part B: Polymer Physics*, 1993, **31**, 1577-1589.
74. W. J. Koros, B. J. Story, S. M. Jordan, K. O'Brien and G. R. Husk, *Polymer Engineering & Science*, 1987, **27**, 603-610.
75. B. J. Story and W. J. Koros, *Journal of Applied Polymer Science*, 1991, **42**, 2613-2626.
76. K. Ghosal and R. T. Chern, *Journal of Membrane Science*, 1992, **72**, 91-97.
77. R. T. Chern, F. R. Sheu, L. Jia, V. T. Stannett and H. B. Hopfenberg, *Journal of Membrane Science*, 1987, **35**, 103-115.
78. R. T. Chern, L. Jia, S. Shimoda and H. B. Hopfenberg, *Journal of Membrane Science*, 1990, **48**, 333-341.
79. B. J. Story and W. J. Koros, *Journal of Membrane Science*, 1992, **67**, 191-210.
80. S. Sridhar, B. Smitha, M. Ramakrishna and T. M. Aminabhavi, *Journal of Membrane Science*, 2006, **280**, 202-209.
81. R. W. Baker and B. T. Low, *Macromolecules*, 2014, **47**, 6999-7013.
82. K. V. Ohya H, Semenova SI, *Polyimide membranes - applications, fabrications, and properties*, Gordon and Breach, 1996.
83. A. Bos, I. G. M. Pünt, M. Wessling and H. Strathmann, *Separation and Purification Technology*, 1998, **14**, 27-39.
84. D. T. Clausi and W. J. Koros, *Journal of Membrane Science*, 2000, **167**, 79-89.
85. D. Q. Vu, W. J. Koros and S. J. Miller, *Journal of Membrane Science*, 2003, **211**, 311-334.
86. K. Tanaka, M. Okano, H. Toshino, H. Kita and K.-I. Okamoto, *Journal of Polymer Science Part B: Polymer Physics*, 1992, **30**, 907-914.
87. L. S. White, *Membrane Gas Separation*, John Wiley & Sons Ltd, 2010.
88. Y. Liu, R. Wang and T.-S. Chung, *Journal of Membrane Science*, 2001, **189**, 231-239.
89. P. S. Tin, T. S. Chung, Y. Liu, R. Wang, S. L. Liu and K. P. Pramoda, *Journal of Membrane Science*, 2003, **225**, 77-90.

90. H.-Y. Zhao, Y.-M. Cao, X.-L. Ding, M.-Q. Zhou, J.-H. Liu and Q. Yuan, *Journal of Membrane Science*, 2008, **320**, 179-184.
91. H. Eguchi, D. J. Kim and W. J. Koros, *Polymer*, 2015, **58**, 121-129.
92. C. Cao, T.-S. Chung, Y. Liu, R. Wang and K. P. Pramoda, *Journal of Membrane Science*, 2003, **216**, 257-268.
93. M. E. Dose, M. Chwatko, I. Hubacek, N. A. Lynd, D. R. Paul and B. D. Freeman, *Polymer*, 2019, **161**, 16-26.
94. L. Escorial, M. de la Viuda, S. Rodríguez, A. Tena, A. Marcos, L. Palacio, P. Prádanos, A. E. Lozano and A. Hernández, *European Polymer Journal*, 2018, **103**, 390-399.
95. E. Hiroshi, U. Hiroki, S. Makoto and Y. Kazuhiro, *JP Patent*, JP2016137484A, 2016.
96. J. S. Lee, W. Madden and W. J. Koros, *Journal of Membrane Science*, 2010, **350**, 232-241.
97. X. Duthie, S. Kentish, S. J. Pas, A. J. Hill, C. Powell, K. Nagai, G. Stevens and G. Qiao, *Journal of Polymer Science Part B: Polymer Physics*, 2008, **46**, 1879-1890.
98. Y. Zhang, I. H. Musselman, J. P. Ferraris and K. J. Balkus, *Journal of Membrane Science*, 2008, **313**, 170-181.
99. J. G. Drobny, *Technology of fluoropolymers*, CRC Press, 2001.
100. P. I. Merkel TC, Prabhakar R, Freeman BD, *Materials Science of Membranes for Gas and Vapor Separation*, John Wiley & Sons Ltd, 2006.
101. V. Arcella, A. Ghielmi and G. Tommasi, *Annals of the New York Academy of Sciences*, 2003, **984**, 226-244.
102. J. Scheirs, *Modern Fluoropolymers: High Performance Polymers for Diverse Applications*, Polymer Science & Technology General, 1997.
103. E. N. Squire, *US Patent*, US4935477A, 1990.
104. D. Hofmann, M. Entrialgo-Castano, A. Lerbret, M. Heuchel and Y. Yampolskii, *Macromolecules*, 2003, **36**, 8528-8538.
105. M. Rudel, J. Kruse, K. Rätzke, F. Faupel, Y. P. Yampolskii, V. P. Shantarovich and G. Dlubek, *Macromolecules*, 2008, **41**, 788-795.
106. T. Masuda, E. Isobe, T. Higashimura and K. Takada, *Journal of the American Chemical Society*, 1983, **105**, 7473-7474.
107. N. A. Platé, A. K. Bokarev, N. E. Kaliuzhnyi, E. G. Litvinova, V. S. Khotimskii, V. V. Volkov and Y. P. Yampol'skii, *Journal of Membrane Science*, 1991, **60**, 13-24.
108. V. V. Volkov, *Polymer Journal*, 1991, **23**, 457-466.
109. A. Morisato, H. C. Shen, S. S. Sankar, B. D. Freeman, I. Pinnau and C. G. Casillas, *Journal of Polymer Science Part B: Polymer Physics*, 1996, **34**, 2209-2222.
110. Y. Ichiraku, S. A. Stern and T. Nakagawa, *Journal of Membrane Science*, 1987, **34**, 5-18.
111. V. P. Shantarovich, I. B. Kevdina, Y. P. Yampolskii and A. Y. Alentiev, *Macromolecules*, 2000, **33**, 7453-7466.
112. K. Takada, H. Matsuya, T. Masuda and T. Higashimura, *Journal of Applied Polymer Science*, 1985, **30**, 1605-1616.
113. T. Masuda, Y. Iguchi, B.-Z. Tang and T. Higashimura, *Polymer*, 1988, **29**, 2041-2049.
114. Y. Hu, M. Shiotsuki, F. Sanda, B. D. Freeman and T. Masuda, *Macromolecules*, 2008, **41**, 8525-8532.
115. K. Nagai, A. Higuchi and T. Nakagawa, *Journal of Applied Polymer Science*, 1994, **54**, 1207-1217.
116. K. Nagai, T. Masuda, T. Nakagawa, B. D. Freeman and I. Pinnau, *Progress in Polymer Science*, 2001, **26**, 721-798.
117. X.-Y. Wang, F. T. Willmore, R. D. Raharjo, X. Wang, B. D. Freeman, A. J. Hill and I. C. Sanchez, *The Journal of Physical Chemistry B*, 2006, **110**, 16685-16693.

118. K. Nagai, A. Higuchi and T. Nakagawa, *Journal of Polymer Science Part B: Polymer Physics*, 1995, **33**, 289-298.
119. L. Starannikova, V. Khodzhaeva and Y. Yampolskii, *Journal of Membrane Science*, 2004, **244**, 183-191.
120. A. J. Hill, S. J. Pas, T. J. Bastow, M. I. Burgar, K. Nagai, L. G. Toy and B. D. Freeman, *Journal of Membrane Science*, 2004, **243**, 37-44.
121. J. Jia and G. L. Baker, *Journal of Polymer Science, Part B: Polymer Physics*, 1998, **36**, 959-968.
122. C. J. Ruud, J. Jia and G. L. Baker, *Macromolecules*, 2000, **33**, 8184-8191.
123. M. Kitchin, J. Teo, K. Konstas, C. H. Lau, C. J. Sumby, A. W. Thornton, C. J. Doonan and M. R. Hill, *Journal of Materials Chemistry A*, 2015, **3**, 15241-15247.
124. D. S. Bakhtin, L. A. Kulikov, S. A. Legkov, V. S. Khotimskiy, I. S. Levin, I. L. Borisov, A. L. Maksimov, V. V. Volkov, E. A. Karakhanov and A. V. Volkov, *Journal of Membrane Science*, 2018, **554**, 211-220.
125. X. Q. Cheng, K. Konstas, C. M. Doherty, C. D. Wood, X. Mulet, Z. Xie, D. Ng, M. R. Hill, L. Shao and C. H. Lau, *ACS Applied Materials & Interfaces*, 2017, **9**, 14401-14408.
126. X. Q. Cheng, K. Konstas, C. M. Doherty, C. D. Wood, X. Mulet, Z. Xie, D. Ng, M. R. Hill, C. H. Lau and L. Shao, *ChemSusChem*, 2017, **10**, 1887-1891.
127. C. H. Lau, K. Konstas, C. M. Doherty, S. Kanehashi, B. Ozcelik, S. E. Kentish, A. J. Hill and M. R. Hill, *Chemistry of Materials*, 2015, **27**, 4756-4762.
128. H. B. Park, C. H. Jung, Y. M. Lee, A. J. Hill, S. J. Pas, S. T. Mudie, E. Van Wagner, B. D. Freeman and D. J. Cookson, *Science*, 2007, **318**, 254-258.
129. G. Dong and Y. M. Lee, *Journal of Materials Chemistry A*, 2017, **5**, 13294-13319.
130. S. Kim and Y. M. Lee, *Progress in Polymer Science*, 2015, **43**, 1-32.
131. D. F. Sanders, Z. P. Smith, C. P. Ribeiro, R. Guo, J. E. McGrath, D. R. Paul and B. D. Freeman, *Journal of Membrane Science*, 2012, **409-410**, 232-241.
132. H. B. Park, S. H. Han, C. H. Jung, Y. M. Lee and A. J. Hill, *Journal of Membrane Science*, 2010, **359**, 11-24.
133. S. H. Han, N. Misdan, S. Kim, C. M. Doherty, A. J. Hill and Y. M. Lee, *Macromolecules*, 2010, **43**, 7657-7667.
134. Y. Wang, X. Ma, B. S. Ghanem, F. Alghunaimi, I. Pinnau and Y. Han, *Materials Today Nano*, 2018, **3**, 69-95.
135. N. B. McKeown and P. M. Budd, *Macromolecules*, 2010, **43**, 5163-5176.
136. P. M. Budd, B. S. Ghanem, S. Makhseed, N. B. McKeown, K. J. Msayib and C. E. Tattershall, *Chemcal Communications*, 2004, **2**, 230-231.
137. L. Gao, M. Alberto, P. Gorgojo, G. Szekely and P. M. Budd, *Journal of Membrane Science*, 2017, **529**, 207-214.
138. P. M. Budd, E. S. Elabas, B. S. Ghanem, S. Makhseed, N. B. McKeown, K. J. Msayib, C. E. Tattershall and D. Wang, *Advanced Materials*, 2004, **16**, 456-459.
139. S. V. Adymkanov, Y. P. Yampol'skii, A. M. Polyakov, P. M. Budd, K. J. Reynolds, N. B. McKeown and K. J. Msayib, *Polymer Science Series A*, 2008, **50**, 444-450.
140. Y. Rogan, L. Starannikova, V. Ryzhikh, Y. Yampolskii, P. Bernardo, F. Bazzarelli, J. C. Jansen and N. B. McKeown, *Polymer Chemistry*, 2013, **4**, 3813-3820.
141. I. Rose, C. G. Bezzu, M. Carta, B. Comesana-Gandara, E. Lasseuguette, M. C. Ferrari, P. Bernardo, G. Clarizia, A. Fuoco, J. C. Jansen, K. E. Hart, T. P. Liyana-Arachchi, C. M. Colina and N. B. McKeown, *Nature Materials*, 2017, **16**, 932.
142. M. J. Baran, M. N. Braten, S. Sahu, A. Baskin, S. M. Meckler, L. Li, L. Maserati, M. E. Carrington, Y.-M. Chiang, D. Prendergast and B. A. Helms, *Joule*, 2019, **3**, 2968-2985.
143. C. Li, A. L. Ward, S. E. Doris, T. A. Pascal, D. Prendergast and B. A. Helms, *Nano Letters*, 2015, **15**, 5724-5729.

144. P. Zuo, Y. Li, A. Wang, R. Tan, Y. Liu, X. Liang, F. Sheng, G. Tang, L. Ge, L. Wu, Q. Song, N. B. McKeown, Z. Yang and T. Xu, *Angewandte Chemie International Edition*, 2020, **59**, 2-12.
145. R. Tan, Wang, A., Malpass-Evans, R. et al., *Nature Materials*, 2020, **19**, 195-202.
146. N. B. McKeown and P. M. Budd, *Chemical Society Reviews*, 2006, **35**, 675-683.
147. P. Budd, N. McKeown, B. Ghanem, K. Msayib, D. Fritsch, L. Starannikova, N. Belov, O. Sanfirova, Y. Yampolskii and V. Shantarovich, *Journal of Membrane Science*, 2008, **325**, 851-860.
148. C. G. Bezzu, M. Carta, A. Tonkins, J. C. Jansen, P. Bernardo, F. Bazzarelli and N. B. McKeown, *Advanced Materials*, 2012, **24**, 5930-5933.
149. M. Carta, M. Croad, R. Malpass-Evans, J. C. Jansen, P. Bernardo, G. Clarizia, K. Friess, M. Lanc and N. B. McKeown, *Advanced Materials*, 2014, **26**, 3526-3531.
150. I. Rose, M. Carta, R. Malpass-Evans, M.-C. Ferrari, P. Bernardo, G. Clarizia, J. C. Jansen and N. B. McKeown, *ACS Macro Letters*, 2015, **4**, 912-915.
151. B. S. Ghanem, R. Swaidan, X. Ma, E. Litwiller and I. Pinnau, *Advanced Materials*, 2014, **26**, 6696-6700.
152. C. G. Bezzu, M. Carta, M.-C. Ferrari, J. C. Jansen, M. Monteleone, E. Esposito, A. Fuoco, K. Hart, T. P. Liyana-Arachchi, C. M. Colina and N. B. McKeown, *Journal of Materials Chemistry A*, 2018, **6**, 10507-10514.
153. B. Liang, X. He, J. Hou, L. Li and Z. Tang, *Advanced Materials*, 2018, **31**, 1806090.
154. E. Madrid, P. Cottis, Y. Rong, A. T. Rogers, J. M. Stone, R. Malpass-Evans, M. Carta, N. B. McKeown and F. Marken, *Journal of Materials Chemistry A*, 2015, **3**, 15849-15853.
155. B. Comesaña-Gándara, J. Chen, C. G. Bezzu, M. Carta, I. Rose, M.-C. Ferrari, E. Esposito, A. Fuoco, J. C. Jansen and N. B. McKeown, *Energy & Environmental Science*, 2019, **12**, 2733-2740.
156. G. B. S., S. Raja, L. Eric and P. Ingo, *Advanced Materials*, 2014, **26**, 3688-3692.
157. N. Du, G. P. Robertson, J. Song, I. Pinnau and M. D. Guiver, *Macromolecules*, 2009, **42**, 6038-6043.
158. C. R. Mason, L. Maynard-Atem, K. W. J. Heard, B. Satilmis, P. M. Budd, K. Friess, M. Lanč, P. Bernardo, G. Clarizia and J. C. Jansen, *Macromolecules*, 2014, **47**, 1021-1029.
159. R. A. Pasternak, G. L. Burns and J. Heller, *Macromolecules*, 1971, **4**, 470-475.
160. F. Bailly, F. Cottet and M. Schlosser, *Synthesis*, 2005, **5**, 791-797.
161. Y. Yampolskii, *Polymer Reviews*, 2017, **57**, 200-212.
162. J. Wu, J. Liu and T.-S. Chung, *Advanced Sustainable Systems*, 2018, **2**, 1800044.
163. C. R. Mason, L. Maynard-Atem, N. M. Al-Harbi, P. M. Budd, P. Bernardo, F. Bazzarelli, G. Clarizia and J. C. Jansen, *Macromolecules*, 2011, **44**, 6471-6479.
164. T. C. Merkel, H. Lin, X. Wei and R. Baker, *Journal of Membrane Science*, 2010, **359**, 126-139.
165. J. C. Foster, S. Varlas, L. D. Blackman, L. A. Arkinstall and R. K. O'Reilly, *Angewandte Chemie International Edition*, 2018, **57**, 10672-10676.
166. K. L. Makovetsky, E. S. Finkel'shtein, I. Y. Ostrovskaya, E. B. Portnykh, L. I. Gorbacheva, A. I. Golberg, N. V. Ushakov and Y. P. Yampolsky, *Journal of Molecular Catalysis*, 1992, **76**, 107-121.
167. S. Martínez-Arranz, A. C. Albéniz and P. Espinet, *Macromolecules*, 2010, **43**, 7482-7487.
168. T. Hong, S. Chatterjee, S. M. Mahurin, F. Fan, Z. Tian, D.-e. Jiang, B. K. Long, J. W. Mays, A. P. Sokolov and T. Saito, *Journal of Membrane Science*, 2017, **530**, 213-219.
169. E. Lasseuguette, M. Carta, S. Brandani and M.-C. Ferrari, *International Journal of Greenhouse Gas Control*, 2016, **50**, 93-99.

170. N. Seehof and W. Risse, *Die Makromolekulare Chemie, Rapid Communications*, 1991, **12**, 107-112.
171. M. Hong, G.-F. Yang, Y.-Y. Long, S. Yu and Y.-S. Li, *Journal of Polymer Science Part A: Polymer Chemistry*, 2013, **51**, 3144-3152.
172. M. Lanč, K. Pilnáček, C. R. Mason, P. M. Budd, Y. Rogan, R. Malpass-Evans, M. Carta, B. C. Gándara, N. B. McKeown, J. C. Jansen, O. Vopička and K. Friess, *Journal of Membrane Science*, 2019, **570-571**, 522-536.
173. S. M. Rafiq, R. Sivasakthikumaran and A. K. Mohanakrishnan, *Organic Letters*, 2014, **16**, 2720-2723.
174. J. Veerman, T. van den Bergh, K. M. Orrling, C. Jansen, P. Cos, L. Maes, E. Chatelain, J.-R. Ioset, E. E. Edink, H. Tenor, T. Seebeck, I. de Esch, R. Leurs and G. J. Sterk, *Bioorganic & Medicinal Chemistry*, 2016, **24**, 1573-1581.
175. R. Short, M. Carta, C. G. Bezzu, D. Fritsch, B. M. Kariuki and N. B. McKeown, *Chemical Communications*, 2011, **47**, 6822-6824.
176. M. Longo, M. P. De Santo, E. Esposito, A. Fuoco, M. Monteleone, L. Giorno, B. Comesaña-Gándara, J. Chen, C. G. Bezzu, M. Carta, I. Rose, N. B. McKeown and J. C. Jansen, *Industrial & Engineering Chemistry Research*, 2019, **59**, 5381-5391.
177. A. Fuoco, B. Comesaña-Gándara, M. Longo, E. Esposito, M. Monteleone, I. Rose, C. G. Bezzu, M. Carta, N. B. McKeown and J. C. Jansen, *ACS Applied Materials & Interfaces*, 2018, **10**, 36475-36482.
178. W. J. Koros and C. Zhang, *Nature Materials*, 2017, **16**, 289-297.
179. R. R. Tiwari, J. Jin, B. D. Freeman and D. R. Paul, *Journal of Membrane Science*, 2017, **537**, 362-371.
180. R. R. Tiwari, Z. P. Smith, H. Lin, B. D. Freeman and D. R. Paul, *Polymer*, 2014, **55**, 5788-5800.
181. S. Harms, K. Rätzke, F. Faupel, N. Chaukura, P. M. Budd, W. Egger and L. Ravelli, *The Journal of Adhesion*, 2012, **88**, 608-619.
182. D. Naiying, R. G. P., P. Ingo, T. Sylvie and G. M. D., *Macromolecular Rapid Communications*, 2009, **30**, 584-588.
183. Z. G. Wang, X. Liu, D. Wang and J. Jin, *Polymer Chemistry*, 2014, **5**, 2793-2800.
184. J. Zhang, J. Jin, R. Cooney, Q. Fu, G. G. Qiao, S. Thomas and T. C. Merkel, *Polymer Chemistry*, 2015, **6**, 5003-5008.
185. X. Ma and I. Pinnau, *Polymer Chemistry*, 2016, **7**, 1244-1248.
186. K. Yuan, C. Liu, S. Zhang, L. Jiang, C. Liu, G. Yu, J. Wang and X. Jian, *Journal of Membrane Science*, 2017, **541**, 403-412.
187. B. Shrimant, U. K. Kharul and P. P. Wadgaonkar, *Reactive and Functional Polymers*, 2018, **133**, 153-160.
188. L. Starannikova, N. Belov, V. Shantarovich, J. Zhang, J. Jin and Y. Yampolskii, *Journal of Membrane Science*, 2018, **548**, 593-597.
189. I. Hossain, S. Y. Nam, C. Rizzuto, G. Barbieri, E. Tocci and T.-H. Kim, *Journal of Membrane Science*, 2019, **574**, 270-281.
190. H. A. Patel and C. T. Yavuz, *Chemical Communications*, 2012, **48**, 9989-9991.
191. S. Yi, B. Ghanem, Y. Liu, I. Pinnau and W. J. Koros, *Science Advances*, 2019, **5**, eaaw5459.
192. B. Satilmis, T. Isık, M. M. Demir and T. Uyar, *Applied Surface Science*, 2019, **467-468**, 648-657.
193. P. Yanaranop, B. Santoso, R. Etzion and J. Jin, *Polymer*, 2016, **98**, 244-251.
194. N. Du, G. P. Robertson, M. M. Dal-Cin, L. Scoles and M. D. Guiver, *Polymer*, 2012, **53**, 4367-4372.
195. B. Satilmis, M. N. Alnajrani and P. M. Budd, *Macromolecules*, 2015, **48**, 5663-5669.

196. M. Hashem, C. Grazia Bezzu, B. M. Kariuki and N. B. McKeown, *Polymer Chemistry*, 2011, **2**, 2190-2192.
197. M. Carta, C. G. Bezzu, J. Vile, B. M. Kariuki and N. B. McKeown, *Polymer*, 2017, **126**, 324-329.
198. R. Swaidan, X. Ma, E. Litwiller and I. Pinnau, *Journal of Membrane Science*, 2013, **447**, 387-394.
199. B. S. Ghanem, M. Hashem, K. D. M. Harris, K. J. Msayib, M. Xu, P. M. Budd, N. Chaukura, D. Book, S. Tedds, A. Walton and N. B. McKeown, *Macromolecules*, 2010, **43**, 5287-5294.
200. F. Bailly, F. Cottet and M. Schlosser, *Synthesis*, 2005, **2005**, 791-797.
201. J. V. Crivello, *The Journal of Organic Chemistry*, 1981, **46**, 3056-3060.
202. J.-L. Pozzo, G. M. Clavier, M. Colomes and H. Bouas-Laurent, *Tetrahedron*, 1997, **53**, 6377-6390.